

Syracuse University

SURFACE

Dissertations - ALL

SURFACE

June 2017

Investigation of the multi-physics of laser-induced ignition of transportation fuels

Nathan Peters
Syracuse University

Follow this and additional works at: <https://surface.syr.edu/etd>



Part of the [Engineering Commons](#)

Recommended Citation

Peters, Nathan, "Investigation of the multi-physics of laser-induced ignition of transportation fuels" (2017). *Dissertations - ALL*. 689.
<https://surface.syr.edu/etd/689>

This Dissertation is brought to you for free and open access by the SURFACE at SURFACE. It has been accepted for inclusion in Dissertations - ALL by an authorized administrator of SURFACE. For more information, please contact surface@syr.edu.

ABSTRACT

Cleaner and more efficient combustion systems are expected to operate at conditions where successful spark ignition is difficult to achieve. Laser ignition is a proposed alternative ignition system capable of stable engine performance under these conditions. Fundamental studies are needed to fully characterize the complex, multi-physics nature of the laser ignition process. This thesis is a contribution in that direction, also characterizing the ignition and flame behavior of some engine-relevant fuels.

This work investigates experimentally the early stages of the laser ignition process, characterizing breakdown and laser-induced shock waves. It then explores self-sustained flame behavior from early flame emergence to complete propagation or quenching.

Regarding the early stages of laser ignition, the influence of focusing optics, thermodynamic conditions, and chemical structure of fuels on optical breakdown threshold is examined. These results are presented in a universal representation of the breakdown threshold, facilitating their comparison. The results agree with previous studies and new data sets are generated.

Thermomechanical differences between breakdown in non-reactive and reactive mixtures are quantified, isolating the effect of exothermicity on plasma and shock wave propagation. The thermodynamic conditions of the gas near the focal volume are investigated and quantified using two-color interferometry. This information is applied toward developing accurate initial conditions for simulations based on absorbed laser energy and early kernel geometry.

With respect to flame propagation, schlieren and interferometric imaging techniques are used

to examine early flame behavior, especially near flammability limits. This provides insight into the mechanisms controlling quenching of fuel-lean laser ignited flames as well as the time-scales involved. Four fuels (methane, biogas, iso-octane, and E85) are characterized, highlighting thermochemical effects which control their flame kernel development, the dynamics, and fate of initially sustained flames.

Laser ignition is further put into context by contrasting with the better established spark ignition process. The duration of energy deposition and heat transfer to the spark plug electrodes are found to be the main reasons for differences between laser and spark ignited flames.

By examining these different physical aspects of laser ignition, this thesis advances understanding of forced ignition, consolidating this by contrasting with spark-ignition behavior. The results are useful for the design of fuel-flexible and lean combustion technologies. The data set is also useful for CFD simulations and simplified modeling of the ignition process.

Investigation of the multi-physics of laser-induced ignition of transportation fuels

Nathan D. Peters

B.S., Iowa State University, 2012

M.S., Syracuse University, 2013

DISSERTATION

Submitted in partial fulfillment
of the requirements for the degree

Doctor of Philosophy in Mechanical and Aerospace Engineering

Syracuse University

June, 2017

Copyright 2017
Nathan D. Peters
All Rights Reserved

Appreciation

I owe a great debt of gratitude to my advisor, Dr. Ben Akih-Kumgeh. He has given me support in my academic pursuits, direction in my research, and advice in life that I will always carry with me. I am extremely lucky to have had his guidance and encouragement during my doctoral studies. He has had confidence in me as a researcher, even when mine has wavered, and for that I am truly grateful.

I wish to thank the members of my dissertation committee: Prof. Mark Glauser, Prof. Melissa Green, Prof. Matthew LaHaye, Prof. Jacques Lewalle, and Prof. Shalabh Maroo for generously offering their time and support in preparation and review of this document. Additionally, my thanks goes to Prof. Ezzat Khalifa, Prof. Alan Levy, and Prof. Mohd Yousuf Ali for their support during my time as a teaching assistant. Most of all, I would like to thank all of them for their continued interest in my progress and encouragement throughout my doctoral studies.

I would like to thank Syracuse University for the continued support of my studies and research. My appreciation goes to the College of Engineering and Computer Sciences for assistance through the Syracuse University Graduate Fellowship and the Department of Mechanical and Aerospace Engineering for the Master's Teaching Support appointment, both of which have been instrumental to my success in the program. Thank you to the Syracuse Center of Excellence for the wonderful lab space in which I have had the pleasure of working and for the conference travel support.

For the past five years, I have had the support of a great group of friends within the Thermodynamics and Combustion Lab. First of all, my thanks to Mazen Eldeeb. I will always be grateful for your friendship and support during our time at SU. Thank you to Deshawn Coombs for all of your help with CFD simulations and great conversations, both about research and beyond. Thank you to Shirin Jouzdani, Apeng Zhou, David Zheng, and Amir Montakhab for your friendship and encouragement. Also, my thanks to the great group of undergraduate students who have made my life easier and been incredibly helpful throughout the course of this work. Finally, thank you to my friends at SU for being so supportive and keeping me sane these past five years.

I am forever grateful for the love and support of my wonderful family. Thank you to my parents. Their unconditional love and continued encouragement is the reason for who I am today. I could not ask for a better support-system and am appreciative of all they have sacrificed to help me achieve my dreams. Thank you to my big sister, Erin, who has steadfastly believed in me and stood behind me throughout my life. Most of all, I want to thank my amazing wife, Jodi. Throughout the highs and lows of my doctoral studies, her love and support has been unwavering. As I progress as a researcher and come to understand the laws governing the world around me, one thing I will never understand is how I got to be so lucky as to have her in my life.

Finally, my thanks to God for the opportunities that have been provided to me and His guidance throughout my life.

Syracuse, New York

May, 2017

Contents

List of Figures	viii
-----------------	------

List of Tables	xv
----------------	----

Dissertation

1	Introduction and literature review	1
1.1	Background and motivation	1
1.2	Literature review	5
1.2.1	Previous research on spark ignition	5
1.2.2	Previous research on laser-induced breakdown	8
1.2.3	Previous research on laser ignition	13
1.2.4	Forced ignition modeling and simulations	18
1.3	Scope and objectives of this work	22
2	Experimental procedure and analysis	24
2.1	Experimental setup	24
2.2	Principles of the experimental visualization techniques	32
2.2.1	Schlieren imaging diagnostic	32
2.2.2	Interferometry diagnostic	33
2.3	Data processing	38
2.4	Outline of experiments	43
2.5	Laser ignition simulations	45

3	Laser-induced breakdown and shock wave dynamics	48
3.1	Laser-induced breakdown threshold	49
3.1.1	Effect of focal length on breakdown threshold	50
3.1.2	Effect of pressure on breakdown threshold	54
3.1.3	Effect of gas composition on breakdown threshold	55
3.1.4	Universal representation of breakdown threshold	58
3.2	Dynamics of laser-induced shock waves	61
3.2.1	Blast wave theory	62
3.2.2	Laser-induced shock waves in combustible mixtures	66
3.3	Internal dynamics of the plasma kernel	71
3.4	Comparison of experimental and simulation results	75
4	Fuel effects on laser-induced ignition	80
4.1	Minimum laser ignition energies	81
4.1.1	Iso-octane and ethanol blends	83
4.1.2	Methane and biogas	87
4.2	Flame kernel development	90
4.3	Propagation of self-sustained flame	94
5	Laser and spark ignition comparison	99
5.1	Plasma kernel	100
5.2	Ignition of iso-octane and ethanol blends	102
5.3	Ignition of methane and biogas	105
6	Conclusion and outlook	116
	Bibliography	120
	Vita	135

List of Figures

1.1	Similarities and differences between forced ignition (left) and auto ignition (right) processes.	2
1.2	Lewis and von Elbe experimental setup [1].	6
1.3	Lewis and von Elbe minimum ignition energies for various fuels as a function of fuel volume in air [1].	6
1.4	Main types of laser ignition mechanisms. Photochemical ignition where a specific laser wavelength is used to target chemical bonds; thermal laser ignition where a laser is used to locally heat a combustible mixture to a temperature where ignition occurs; and laser-induced breakdown ignition where a focused laser beam is used to create a plasma which initiates combustion.	9
1.5	Schlieren image of laser-induced plasma and shock wave 5 μ s after optical breakdown.	12
2.1	Outer view of constant volume combustion chamber, showing optical windows.	26
2.2	An overview of the experimental setup for laser ignition studies.	26
2.3	Experimental setup depicting the arrangement of laser power meters for measuring incident and absorbed laser pulse energies.	27
2.4	Spark plug ignition circuit.	28
2.5	Spark plug mounted in combustion chamber for spark ignition experiments. .	29
2.6	Schematic of the laser ignition experiment including the schlieren imaging system.	30
2.7	A schematic of the Mach-Zehnder interferometer used in this work.	31

2.8	Schlieren image of laser-induced shock wave (left) and binary image showing edges of the shock wave (right).	39
2.9	Quantifying the temporal evolution of the early flame kernels using the lower edge and the center of the energy reception focus.	39
2.10	Schlieren image of laser-ignited flame showing location of analysis of the flame front and plot of the gradient of pixel intensity.	40
2.11	Example of the temporal evolution of a laser-ignited flame for a methane/air mixture at 1 atm and 300 K.	40
2.12	Interferometric image of laser-induced plasma and shock wave 1.5 μ s after optical breakdown.	41
2.13	Pixel intensity plotted for a row of pixels from the interferometric image and the resulting discretized fringe locations.	42
2.14	Discretized and undisturbed fringe locations used to calculate localized phase shift for interferometric images.	42
3.1	Approximate timeline of laser ignition from the start of the laser pulse to the end of combustion.	49
3.2	Logistic regression for breakdown in air using a focal length of 25 cm. Red circles signify successful (1) and unsuccessful (0) breakdown events.	51
3.3	Variation of breakdown energy threshold with lens focal length. The gas is air at $T = 300$ K, $p = 1$ atm.	51
3.4	Variation of breakdown power density threshold with lens focal length, accounting for spherical aberrations due to the focusing lens. The gas is air at $T = 300$ K, $p = 1$ atm.	53
3.5	Variation of breakdown energy threshold with chamber pressure. The gas is air at $T = 300$ K and a focal length of 15 cm.	54

3.6	Variation of breakdown power density threshold with chamber pressure. The gas is air at $T = 300$ K with a lens of $f = 15$ cm. The larger uncertainty is associated with errors in the estimate of focal geometry.	55
3.7	Breakdown energy threshold for air and mixtures of methane/air and biogas/air at $\phi = 0.65$, $T = 300$ K, and $f = 15$ cm.	56
3.8	Breakdown power density threshold for air and mixtures of methane/air and biogas/air at $\phi = 0.65$, $T = 300$ K, and $f = 15$ cm.	57
3.9	Universal plot for laser-induced breakdown in air at $T = 300$ K showing results for focal length and pressure.	61
3.10	Schlieren images showing the evolution of a laser-induced shock wave in air.	62
3.11	Comparison of Taylor-Sedov and Jones blast wave theories with experimental data for 25.2 mJ of absorbed laser pulse energy in air at $T = 295$ K, $p = 1$ atm. Both blast wave theory calculations use a point blast energy of 22.4 mJ.	64
3.12	Experimental data (symbols) and Jones blast wave theory (lines) for three different absorbed laser pulse energies in air at $T = 295$ K, $p = 1$ atm.	68
3.13	Experimental data (symbols) and Jones blast wave theory (lines) for 3.79 mJ of absorbed laser pulse energy in air and methane at $T = 295$ K, $p = 1$ atm.	69
3.14	Phase shift at $5 \mu\text{s}$ after breakdown measured by one-color interferometer for air, methane, and biogas at $\phi = 0.6$	72
3.15	Line-averaged gas density measured with two-color interferometer at $1.5 \mu\text{s}$ after breakdown in air for an incident laser pulse energy of 12.3 mJ.	73
3.16	Line-averaged electron density measured with two-color interferometer at $1.5 \mu\text{s}$ after breakdown in air for an incident laser pulse energy of 12.3 mJ.	73
3.17	Spatial and temporal evolution of the gas density in the laser-induced plasma.	74
3.18	Comparison of experimental and simulated density gradient fields in laser-induced shock waves in air at $p = 1$ atm, $T = 300$ K and $E_{\text{absorbed}} = 25.2$ mJ.	75

3.19	Temporal evolution of the shock front in air initially at $p = 1$ atm, $T = 300$ K.	76
3.20	Comparison of the spatial and temporal evolution of the gas density in the laser-induced plasma obtained through experiment (solid black line) and simulation (red dashed line).	77
3.21	Evolution of velocity field, arising from a laser-induced shock wave in air initially at $p = 1$ atm, $T = 300$ K with $E_{absorbed} = 25.2$ mJ.	78
4.1	Example of successful and quenched flame kernels.	82
4.2	Laser ignition of iso-octane and E85, focal length of 15 cm, $p = 1$ atm, and $T = 300$ K.	83
4.3	Laser ignition of iso-octane and E85, focal length of 15 cm, $p = 1$ atm, and $T = 300$ K.	84
4.4	Constant pressure adiabatic flame temperature for various equivalence ratios of iso-octane/air and ethanol/air with initial conditions of $p = 1$ atm, $T = 300$ K.	85
4.5	Laminar burning velocity for various equivalence ratios of iso-octane/air and ethanol/air with initial conditions of $p = 1$ atm, $T = 300$ K.	86
4.6	Minimum ignition energies at various equivalence ratios of methane/air and biogas/air mixtures, focal length of 15 cm, $p = 1$ atm, and $T = 300$ K. These increase rapidly near the lean limit.	88
4.7	Minimum pulse energy for various equivalence ratios of methane/air and biogas/air. Dashed line represents approximate breakdown threshold for methane and biogas mixtures, for a focal length of 15 cm, $p = 1$ atm, and $T = 300$ K.	88
4.8	Constant pressure adiabatic flame temperature for various equivalence ratios of methane/air and biogas/air with initial conditions of $p = 1$ atm and $T = 300$ K. Values are obtained from chemical equilibrium calculations using the program GASEQ.	89

4.9	(Top) Comparison of flame kernel visualized by interferometry at 0.1 ms for stoichiometric methane, 75% CH ₄ /25% CO ₂ , and 50% CH ₄ /50% CO ₂ . (Bottom) Contour maps showing the magnitude of the fringe deflection, where magnitude of 2 corresponds to a displacement of 2 fringe widths.	92
4.10	Laser ignited flame kernel development for methane and biogas at $\phi = 0.9$, $p = 1$ atm, and $T = 300$ K. The incident laser energies for these ignition events were 17.7 mJ for methane and 17.5 mJ for biogas.	93
4.11	Front lobe radius, r_{FL} , compared to radius of toroidal section, r_{TS} . Symbols represent the average of five ignition events and are fitted with a trendline.	94
4.12	Evolution of laser ignited flames of methane and biogas at $\phi = 0.9$, $p = 1$ atm, and $T = 300$ K. The incident laser energies for these ignition events are 17.72 mJ for methane and 17.51 mJ for biogas.	95
4.13	Chamber dynamic pressure histories for single ignition events of methane and biogas mixtures at various equivalence ratios, $p = 1$ atm, and $T = 300$ K.	96
4.14	Chamber dynamic pressure histories for methane and biogas mixtures with the same mass fraction of methane, $p = 1$ atm, and $T = 300$ K. Biogas at $\phi = 0.85$ corresponds with methane at $\phi = 0.75$ and biogas at $\phi = 0.65$ corresponds with methane at $\phi = 0.6$	96
4.15	Constant pressure adiabatic flame temperature for various equivalence ratios of methane/air and biogas/air with initial conditions of $p = 1$ atm, $T = 300$ K. Red lines identify methane and biogas fuel/air mixtures with the same mass fraction of methane.	97
5.1	(Top) Interferometer fringe patterns for laser-induced breakdown and the initial and final stages of spark-discharge in air. (Bottom) Contour maps showing the magnitude of the fringe deflection, where magnitude of 1 corresponds to a displacement of 1 fringe width.	101

5.2	Schlieren images of laser and spark ignited flames of E85/air mixtures, $T = 300$ K, $p = 1$ atm.	103
5.3	Quantifying the temporal evolution of the early flame kernels using the lower edge and the spark center.	103
5.4	Comparison of iso-octane flame propagation for spark (blue) and laser (red) ignited flames at stoichiometric (solid lines) and lean (dashed lines) equivalence ratios, $T = 300$ K, $p = 1$ atm.	104
5.5	Comparison of E85 flame propagation for spark (blue) and laser (red) ignited flames at stoichiometric (solid lines) and lean (dashed lines) equivalence ratios, $T = 300$ K, $p = 1$ atm.	105
5.6	Evolution of the early flame kernels in laser-induced and spark-ignited methane flames under stoichiometric and lean conditions. At 4 ms, the lean flames clearly propagate slower than the stoichiometric flames for each method, with the spark-ignited flames clearly lagging the laser-induced flames.	107
5.7	Pressure profiles during ignition of stoichiometric and lean mixtures of methane by laser and spark-discharge. At the same equivalence ratio, similar pressure evolution is observed.	108
5.8	Quantitative differences in the evolution of the laser-induced and spark-ignited methane flame kernels. Differences are more pronounced for the lean mixtures.	109
5.9	Evolution of laser- and spark-ignited flames of 100% CH_4 and 50% $\text{CH}_4/50\%$ CO_2 , both at $\phi = 0.8$	110
5.10	Pressure profiles for ignition of 100% CH_4 , 75% $\text{CH}_4/25\%$ CO_2 , and 50% $\text{CH}_4/50\%$ CO_2 by laser and spark-discharge at $\phi = 0.8$. Spark ignition shows a small lag in pressure rise as more CO_2 is added to the fuel.	111

5.11 Quantitative differences in the evolution of the laser-induced and spark-ignited flame kernels for mixtures of 100% CH₄, 75% CH₄/25% CO₂, and 50% CH₄/50% CO₂ at $\phi = 0.8$. Long induction period is observed for spark ignited biogas mixtures. 112

List of Tables

3.1	Values for the ratio of specific heats, γ , and geometry parameter, B , for gases used in this study.	66
3.2	Point blast energies, in mJ, calculated using Jones blast wave theory compared to absorbed laser energy, $E_{absorbed}$, in mixtures at $p = 1$ atm, $T = 295$ K. . .	69

Investigation of the multi-physics of laser-
induced ignition of transportation fuels

Chapter 1

Introduction and literature review

1.1 Background and motivation

Combustion systems are an important part of transportation and power generation. Combustion systems require an ignition mechanism to initiate self-sustained combustion as in gas turbines, or for repetitive combustion mode operation as in internal combustion engines. There are two types of ignition, termed auto-ignition and forced ignition as illustrated in Figure 1.1. In auto-ignition, a fuel/air mixture is elevated to temperatures and pressures where combustion can start after a characteristic delay time as a result of chain reactions. In forced ignition, however, localized energy input from an external source is used to start the combustion of a small volume which then evolves into a self-sustained combustion wave. The energy delivery can be performed using a number of different methods and it occurs over a short duration. The most common method of energy delivery is the spark plug. When a high voltage is applied to a spark plug, an electrical potential between the high voltage center electrode and outer ground electrode causes the air between them to ionize, creating a plasma that can initiate combustion in fuel/air mixtures. This is an old technology with little room for further improvement. As combustion systems increasingly operate in regimes where spark ignition is difficult to achieve, other more robust ignition technologies must be

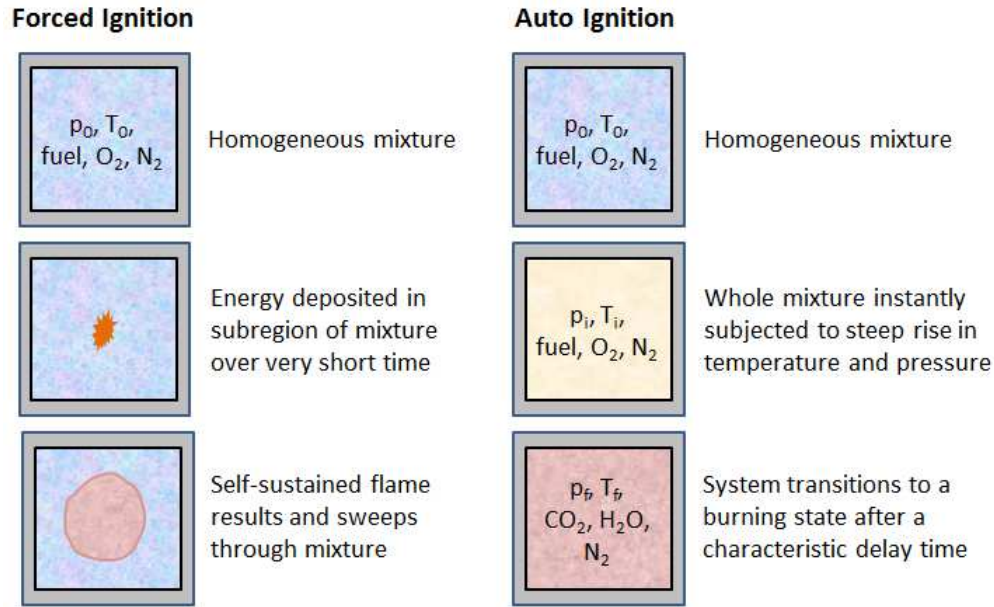


Figure 1.1: Similarities and differences between forced ignition (left) and auto ignition (right) processes.

considered. One of the promising alternatives is laser ignition.

Laser ignition consists in focusing a laser beam to a small volume such that it results in optical breakdown and plasma formation if the power density exceeds a certain threshold. The breakdown in air occurs at a power density of about 10^{11} W/cm² [2]. If breakdown occurs in a combustible gas, the gas is ignited and can result in the propagation of a self-sustained flame. This process differs in many ways from spark plug ignition. For example, the time scale is much shorter for laser ignition and the physics of the photon-driven laser-induced breakdown process is not the same as the dielectric breakdown that occurs in spark plugs between electrodes.

There are many benefits associated with using laser ignition compared to using spark plug ignition. One of the main benefits is the ability to ignite leaner mixtures with comparable energy input. This lowers combustion temperatures, which is conducive for lower NO_x emissions. Additionally, since the laser can be focused anywhere inside the combustion chamber, ignition is no longer confined to the combustion chamber walls; areas with the

greatest probability of ignition can be strategically targeted. Also, getting rid of electrodes has major advantages in engine applications and research. In engine applications, laser ignition occurs at locations that are away from any materials, so the system is not affected by wall temperature. On the contrary, in spark ignition engines, the electrodes are cold at start-up. They therefore act like heat sinks, thereby reducing the probability of ignition. The laser ignition system thus presents a "clean" ignition problem that can be studied without the added complexity of heat transfer to the surrounding electrodes. The resulting flame can also be more easily characterized and modeled.

A major drawback for laser ignition is the added cost and size of high-power lasers needed to generate the laser pulse. Since the development of laser technology and laser ignition approaches, flash-pumped solid state lasers have been used. They emit fundamental frequencies in the near infrared region and can be frequency doubled to visible and ultraviolet laser output. The lasing material is a solid state crystal such as neodymium-doped yttrium aluminum garnet (Nd:YAG) which receives energy from a flash lamp. After multiple reflections and population inversion, the laser beam is emitted by means of a Q-switch. Conventional flash pumped solid state lasers are quite large and thus the size might be too limiting for most laser ignition applications.

Considerable progress has been made in recent decades in laser technology that have reduced both the size and cost of potential lasers for ignition. Much of this stems from improvements to laser diodes and diode pumped solid state lasers. Laser diodes are used in many applications where size is a major constraint. This includes laser pointers, DVD players, bar code readers, and many other applications. It is now possible to create diode pumped solid state microlasers with an energy output of several millijoules; enough to cause laser-induced breakdown [3, 4]. This would replace the larger flash-pumped lasers which are still typically used for research. Furthermore, the military is developing laser defense weapons capable of being mounted on aircraft by the year 2020 [5]. This will require light weight, rugged laser systems which can

handle the intense vibrations that can be experienced mid-flight. Scaled down versions of this technology could possibly be used for future ignition systems.

In addition to characterizing ignition concepts, accurate physical models of the ignition process are needed for combustion analysis at the design stage. Computer-aided engineering is often applied to combustion analysis since it is less expensive than, and complementary to, experiments and full-scale tests. With proper representation of the physics and thermodynamics of the problem, computational fluid dynamics (CFD) simulations can help predict the performance of various engine or combustor designs. In view of limited resources, there is a trade off between model accuracy and computational cost during analysis. To reduce cost, simplified but sufficiently accurate physical models are needed. Resolving the short time-scales and small spatial-scales required for correctly capturing ignition events is a computationally expensive task. Simplified ignition models could be used to initialize engine simulations that do not fully resolve these small scales. However, to maintain accuracy, the ignition process must be fully understood and modeled correctly. This is where experiments that expand our knowledge of fundamental physical phenomena come into play. In order to have accurate low-dimensional models, we must have a solid understanding of the complex physics of the problem at hand. To arrive at an ignition model, we need to break up the problem into simpler sub-processes.

This thesis is focused on characterizing the multi-physics processes associated with laser ignition. The results are rationalized by invoking analogous processes in spark ignition. The data also sets the stage for ignition modeling.

1.2 Literature review

A review of progress in fundamental spark and laser ignition studies is presented. For laser ignition, the previous research encompasses laser-induced breakdown and laser ignition of conventional and non-conventional fuels. Spark ignition research is reviewed to put the laser ignition work into context. Ignition modeling for CFD applications is also reviewed. Persisting challenges are identified throughout the review and they form the basis of this work.

1.2.1 Previous research on spark ignition

Spark ignition is used to initiate burning processes in many combustion engines. Although the study of ignition by spark discharge has been ongoing for many decades, it does not receive as much attention as auto-ignition in the combustion research community. This is likely due to the perception that with a large enough energy deposition, ignition will be successful, and the details of this process can be overlooked. However, accurate ignition models require good understanding of the underlying physics of forced ignition, which can be quite different depending on the method used. Apart from ensuring successful ignition, care must also be taken to avoid a detonation or quenched flame at later times.

Early research in spark ignition was pioneered in the 1950's by Lewis and von Elbe [1]. They performed parametric studies of minimum ignition energy (MIE) for electrode-based sparks. The MIE is the lowest spark energy needed to realize successful initiation of combustion. It depends on the spark gap, electrode type, and thermodynamic conditions of the mixture. Figure 1.2 shows the setup of the Lewis and von Elbe experiment for the measurement of MIE. Figure 1.3 shows the result for a number of fuels as a function of fuel volume in air. As can be seen, MIE is lowest for stoichiometric mixtures but rapidly increases as we approach fuel lean conditions. Although often cited as the standard for minimum ignition

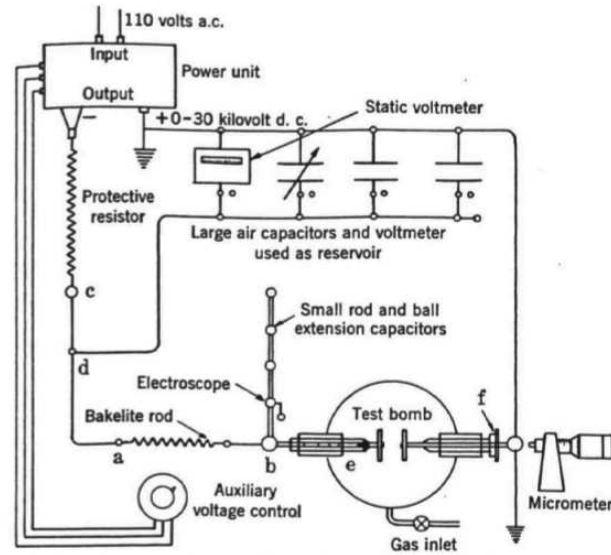


Figure 1.2: Lewis and von Elbe experimental setup [1].

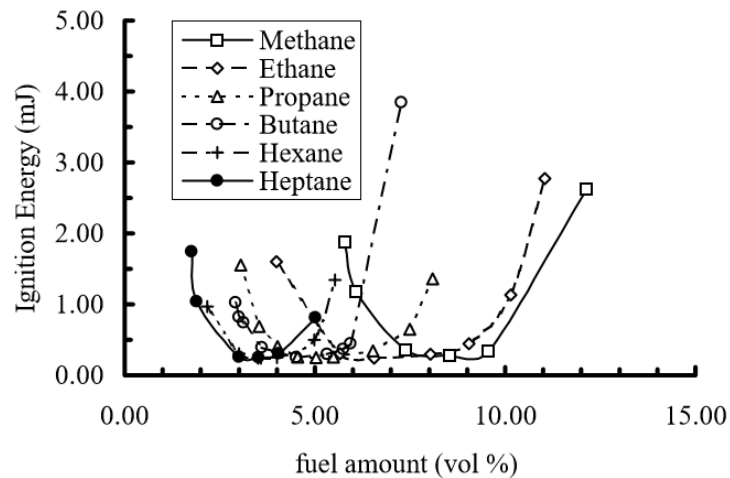


Figure 1.3: Lewis and von Elbe minimum ignition energies for various fuels as a function of fuel volume in air [1].

energy measurements, many researchers have called into question their measurements due to the inability to reproduce MIE as low as 0.25 mJ as reported in their work.

Many subsequent studies have used direct observational methods, such as schlieren, to characterize the flame development process. A phenomenological model for early flame kernel growth based on high-speed schlieren imaging has been developed by Lim et al. [6]. In their model, they show the initial rapid flame kernel growth is controlled by the breakdown process

and power input while the subsequent flame growth is diffusion controlled. Following this approach, Arpaci et al. [7] used a power law to identify the different regimes of flame kernel growth and subsequent transition to a self-sustained flame. The flame kernel size needed to ensure sustained propagation, termed the critical radius, was studied experimentally by Kelley et al. [8] and theoretically by Chen et al. [9]. More recently, research has concentrated on fundamental spark ignition studies in extreme environments, using advanced diagnostics. Sforzo et al. [10] studied the post-discharge evolution of spark igniter flame kernels in a uniform flow. They modeled the spark discharge as instantaneous thermal energy deposition, which agreed well with experimental results from high-speed schlieren imaging. They found that for a fixed deposition energy, the spark kernel evolution is essentially independent of initial size and composition of the kernel. Assanis et al. [11] used a rapid compression machine (RCM) to study the interaction of autoignition chemistry with simultaneous flame development initiated by a spark plug. Compression heating of the unburned mixture by the spark ignited flame was found to reduce autoignition delay times. Dilution effects on the lean flammability limit were also studied and found to correlate well with the theoretical adiabatic flame temperature. In-cylinder, quasi-4D measurements of early flame propagation have been performed by Peterson et al. [12]. They revealed a large dynamic range of local flame displacement speeds near the spark plug, a testament to the complex nature of flame kernel development during this early stage.

One important parameter that can vary significantly between different ignition systems is the timescale of energy deposition. In an important study by Maly & Vogel [13] on the three modes of spark ignition (breakdown, arc, and glow discharge), they found the breakdown process to have the largest affect on early flame behavior. It was determined that short duration energy transfer with high efficiency is best for producing a robust flame kernel. Although not stated in the paper, this makes a strong case for nanosecond-duration ignition methods such as laser ignition. Further insight into the complex spark ignition problem may come through fundamental comparative studies with other ignition technologies. This is

something that is strongly lacking in the literature.

1.2.2 Previous research on laser-induced breakdown

The following section addresses research on breakdown of gases caused by a focused laser beam. General research on the properties affecting the breakdown threshold are presented followed by characteristics of the breakdown process, including plasma production and the laser-induced shock wave dynamics.

Laser-induced breakdown

When a laser beam is tightly focused to a small volume of gas, optical breakdown can occur a number of ways. The possible processes are photochemical, thermal, and laser-induced breakdown as shown in Figure 1.4. Laser-induced breakdown can be resonant and non-resonant breakdown [14]. Non-resonant breakdown, whereby the strength of the electric field in the focal region causes breakdown, is preferable for most applications since it is not wavelength dependent and occurs over short time scales [15]. During non-resonant breakdown, plasma is formed in the focal volume by two competing mechanisms, multiphoton ionization and collisional cascade. Multiphoton ionization is the simultaneous absorption of a sufficient number of photons to cause ionization of a molecule [16]. Multiphoton ionization dominates at low pressures and short wavelength lasers (ultraviolet). This is because short wavelength photons have higher energies, so fewer photons need to be absorbed during the laser pulse to cause ionization. During collisional cascade (also called electron cascade), initial free electrons present in the gas absorb photons. If sufficient energy is gained, they can ionize neutral molecules upon impact [15]. This process then repeats, creating further ionizing the gas. Collisional cascade ionization dominates at longer wavelengths (visible, infrared) and higher pressures where electron collisions are more likely.

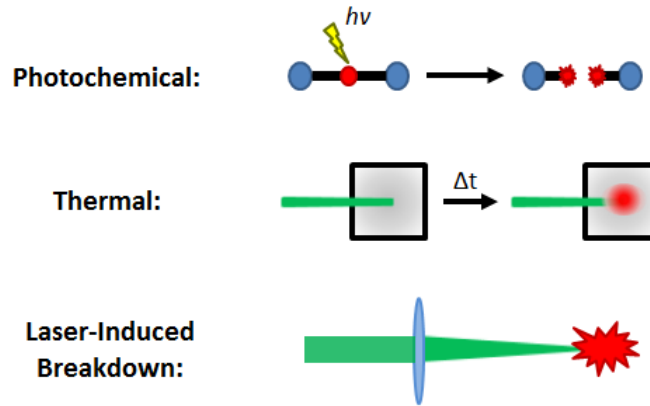


Figure 1.4: Main types of laser ignition mechanisms. Photochemical ignition where a specific laser wavelength is used to target chemical bonds; thermal laser ignition where a laser is used to locally heat a combustible mixture to a temperature where ignition occurs; and laser-induced breakdown ignition where a focused laser beam is used to create a plasma which initiates combustion.

It has been known for decades that focused laser beams can create plasma when pulsed at energies above a given gas-specific breakdown threshold. In the 1960s following the development of lasers, research focused on the parameters affecting this breakdown threshold. One of the earliest studies on the effect of focal length and pressure was by Mitsuk et al. [17]. This study focused on breakdown in xenon and krypton at low pressures of 0.06 - 0.75 atm. They found that the threshold field intensity depends strongly on focal distance for low pressures where plasma diffusion losses are present. Other types of losses, such as plasma recombination and elastic collision losses, were found to be insignificant under those conditions. A later study by Chan et al. [18] investigated the effects of focal length and pressure for an additional number of gases, showing a similar trend. Stricker & Parker [19] determined breakdown thresholds for oxygen and nitrogen for a laser wavelength of 1064 nm and pressures from 1 to 50 atm. This paper proposed a geometric interpretation of the focal volume that is commonly adopted today. A universal representation of the breakdown data was also proposed to facilitate comparison with microwave breakdown data [20]. Pressure and focal length dependence on breakdown threshold was also studied by Tambay & Thareja [21], including laser wavelength effects as well. More recently, Thiyagarajan & Scharer [22]

used a 193 nm laser to investigate breakdown thresholds of air for UV wavelengths where multiphoton ionization is the dominant ionization mechanism.

Of importance to combustion system applications is how the breakdown threshold varies in fuel/air mixtures of various compositions. Hickling and Smith [23] first studied combustible gases, focusing on mixtures of air and fuel such as, isooctane, cyclohexane, n-heptane, n-hexane, clear indolene, and No. 1 diesel fuel. They reported no significant differences between the breakdown energy of air and the energies of the fuels studied. These studies of combustible mixtures should be extended to lighter hydrocarbon fuels such as methane, for which a higher volume of fuel is present in the mixture. This higher fuel percentage may cause some differences. Additionally, methane-based fuels such as natural gas and biogas are likely to be the first fuels to be used with laser ignition systems in combustion systems. To date, literature on laser-induced breakdown in methane [2, 24, 25] only pertains to pure gases and not mixtures of methane and air.

Most studies on the effect of focal length on breakdown threshold have concentrated either on short focal lengths (< 15 cm) or long focal lengths (> 15 cm). Few have investigated the intersection of these regions, highlighting where the importance of diffusion losses begin. Additionally, a universal representation of both focal length and pressure dependence plotted together is missing; particularly at a wavelength of 532 nm. The universal representation of optical breakdown thresholds has currently only been applied to infrared and ultraviolet wavelengths. A noted deficiency in the literature is breakdown in combustible gases, particularly light hydrocarbons. This special focus on combustible gases is needed for application to laser ignition.

Laser-induced plasma

Once laser-induced breakdown occurs, a high temperature plasma is formed originating from the laser focal volume. Once the plasma recombines, the high temperature gas can persist

for several milliseconds. The breakdown process and evolution of the plasma kernel can be difficult to investigate experimentally. Two commonly used non-intrusive diagnostics for plasmas are interferometry and spectroscopy.

Interferometry is an optical diagnostic method capable of yielding quantified changes in refractive index. In essence, a simple interferometer consists in splitting a coherent beam of light along two different optical paths and then recombining them to cause an interference pattern. A change in refractive index in one of the beam paths changes the optical path length and can be visualized as a deflection in the interferometric fringe pattern. This technique is utilized in many plasma applications to measure electron and neutral species densities. It was first used for studying laser breakdown by Alcock and Ramsden [26] in 1966 where they used a two wavelength interferometer to measure average electron density of the plasma. Later on, Kimura et al. [27] also used a two wavelength interferometer to measure electron and neutral species densities for a spark gap in 5% SF₆/20% N₂/75% He and 1% Xe/99% H₂ mixtures. Further, Villagran-Muniz et al. [28] used a two wavelength interferometer to investigate laser-induced plasmas in atmospheric air in 2001, reporting a temporal evolution of electron density. Since then, most interferometric studies of laser-induced plasmas have used a single wavelength interferometer, determining electron densities and change in refractive index [29, 30, 31, 32, 33]. What is still missing is a detailed study of neutral species densities which will provide the most useful information for validating simulations of the flows resulting from laser-induced breakdown processes.

In the last two decades, the study of plasmas through emission spectra has become more prevalent with the emergence of laser-induced breakdown spectroscopy (LIBS). In 1998, Chen et al. [34] provided a detailed study of the spatial and temporal evolution of laser-induced plasmas with nanosecond resolution. More recently, this was also studied by Kawahara et al. [35]. Yalcin et al. [36] used emission spectra to study temperature and electron density evolution in laser-induced air plasmas. A similar technique was used by El-Rabii et al. [37]

to measure temperature and composition of plasmas produced by a UV laser for the first time. Although an effective method for providing some thermodynamic quantities of plasmas, key information useful for modeling laser plasmas, such as absolute gas density, cannot be provided by emission spectra.

Laser-induced shock waves

Another physical process associated with optical breakdown in gases is the formation of a shock wave as a result of rapid energy deposition. Some recent work has focused on characterizing the resulting shock wave dynamics. Navarro-Gonzalez et al. [38] investigated shock waves formed by $1.064\ \mu\text{m}$ laser pulse in 1 atm of air. The shock radius at a given time was found not to have a strong dependence on focal length. In a separate study by the same authors [39], the average shock velocity for a 300 mJ pulse was found to be $460 \pm 70\ \text{m/s}$ at $1\ \mu\text{s}$. The shock velocity for a 300 mJ pulse in air was also investigated by Lackner et al. [40]. They found a much higher velocity of 1,900 m/s at $1\ \mu\text{s}$ showing that there are still a lot of inconsistencies in shock velocity measurements among different research groups. They also investigated reactive systems such as methane/air ignition, showing that equivalence ratio had a negligible effect on the size of the resulting ellipsoidal flame kernel. Recently,

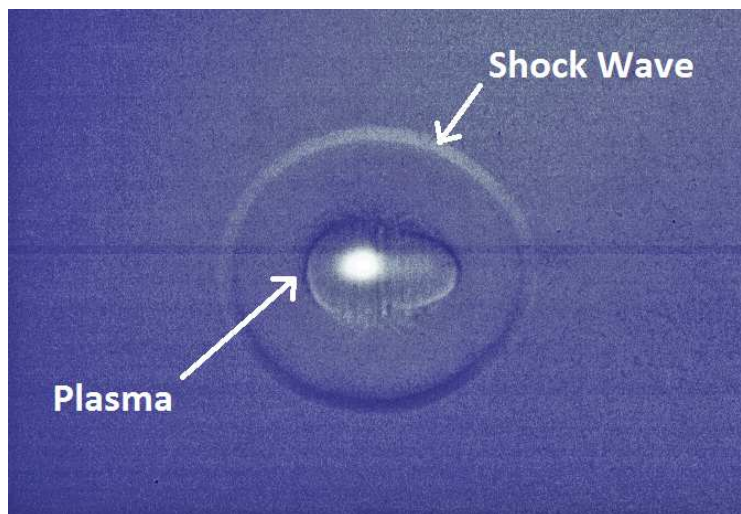


Figure 1.5: Schlieren image of laser-induced plasma and shock wave $5\ \mu\text{s}$ after optical breakdown.

Gebel et al. [41] compared experimental shock velocity results for breakdown in air to various blast wave theories. A blast wave theory characterizes the temporal evolution of a shock front from a point-like rapid deposition of energy. Given the energy, the theory predicts the time dependence of the shock front. Conversely, from the temporal evolution of the shock front, the energy used to generate the blast can be estimated. Gebel et al. found that the often referenced Taylor-Sedov blast theory [42] does not work for laser-induced shock waves since the Mach number quickly reduces to near unity. It was also found that more than 50% of the energy from the absorbed laser pulse can go to generating the shock wave.

Although laser-induced shock waves have been investigated in a number of non-reactive gases, few have studied shock waves in combustible mixtures. Moreover, none have used the blast wave theory to investigate point blast energy in combustible mixtures. This could determine the role of exothermicity of reactants in the focal volume on the shock wave dynamics. This is often mentioned in literature [43, 44, 45, 46], although no experimental studies have so far quantified this assertion.

1.2.3 Previous research on laser ignition

Laser ignition fundamentals

Laser ignition is the initiation of combustion by means of a focused laser as described previously. This was investigated in the 1970's but later abandoned due in large part to researchers believing it would never be economically feasible. There has been renewed interest in laser ignition over the last 20 years driven by advances in laser technology as well as the current trends in combustion systems [47]. There are a number of benefits associated with the use of laser ignition over conventional spark ignition systems. The location of the ignition spot inside the combustion chamber can be optimized to minimize misfires, taking advantage of recirculation zones and areas of high fuel concentration [48]. Additionally, it is possible to

extend lean flammability limits and realize combustion under conditions which favor lower combustion temperatures and, therefore, lower NO_x emissions [49, 50]. To reduce the size of combustion systems and improve thermodynamic efficiencies, the design trend is toward higher system pressures. This is a challenge for traditional spark plugs which require higher breakdown voltages at these conditions. On the contrary, studies have shown that the energy required for successful laser ignition decreases as the chamber pressure increases [51]. While the development of laser ignition systems is still in the early phase, research into miniaturized lasers is ongoing and it is anticipated that modular systems will be available in due course as previously mentioned [52, 53].

Early work in the area of laser ignition has been reviewed by Ronney [15], highlighting a fundamental description of how breakdown occurs as well as topics of technical importance, such as ignition energies. Bradley et al. [50] furthered the discussion of ignition fundamentals in their review including assessment of the effects of turbulence on flame propagation. Tauer et al. [54] summarized information on breakdown and ignition while also focusing on the application side by describing current technological capabilities. Another application-based review by Morsy [55] gives the current state of laser ignition in internal combustion engines.

In terms of the fuels investigated, fundamental research in laser ignition has mostly focused on methane fuel. Early work by Ma et al. [56] was performed in a single cylinder test engine fueled with methane. Results showed the feasibility of the concept as well as improvements in certain areas of performance, such as faster flame propagation. Soon after, Phuoc et al. [57] measured minimum ignition energies (MIE) of methane for a range of equivalence ratios from 0.66 to 1.95. Results showed ignition energies in the range of 3 to 4 mJ for stoichiometric and slightly rich mixtures. At the lean limit of the study energies were as high as 40 mJ. Apart from the MIE, the minimum pulse energy (MPE) is also important for laser ignition. This is the laser pulse energy, a fraction of which is eventually absorbed as MIE. The dependence of MPE on other parameters such as focal length and pressure was investigated by Kopecek et

al. [58]. Pressure dependence of methane ignition was also studied by Weinrotter et al. [51]. They observed that high temperatures can extend the lean limit of laser ignited methane mixtures. Methane was ignited in their combustion chamber at an MPE of just 0.15 mJ, close to the theoretical minimum ignition limit predicted by Lewis and von Elbe [1]. They note that these values can only be obtained by optimizing focusing optics and laser parameters. More recently, Srivastava et al. [59, 60, 61, 62] have carried out further studies on laser ignition of compressed natural gas (CNG). The structure and propagation of laser-ignited CNG flames were investigated along with effects of focal length on ignition energies. The performance of laser ignition in a single cylinder test engine has also been evaluated.

Another fuel of practical interest is iso-octane, an important component in gasoline. Most application based studies have focused around comparisons of ignition systems in gasoline test engines and have shown improved combustion stability for laser ignition systems over spark ignition [63, 64]. The results from many of these IC engine tests have been summarized in papers by Morsy [55] and Dearden and Shenton [65]. However, there have been very few fundamental studies of iso-octane laser ignition. One such study by Ternel et al. [66] determined MIEs of iso-octane for different focal lengths and wavelengths of laser light. In order to gain a proper understanding of how different fuels affect ignition dynamics, this work must be extended to include fuels that are increasingly considered for combustion systems.

Until now, laser ignition studies have mainly focused on a limited number of conventional fuels. Many of the first applications of laser ignition will likely employ non-conventional fuels, such as biofuels, and therefore fuel diversity must be addressed.

Laser ignition of non-conventional fuels

The number and chemical composition of potential fuels for various combustion systems are expected to vary more widely in the future on account of increased use of renewable and coal-derived fuels. These fuel differences necessitate examination of the impact of their

thermochemical properties on ignition dynamics. However, most laser ignition studies have focused on methane, as mentioned previously. Further, there are few comparative studies of fuel effects on laser ignition. In order to successfully implement laser ignition systems, these open questions need to be investigated.

One of the first practical uses of laser ignition may be in stationary power generation systems. For many stationary gas turbines and IC engines, natural gas is widely used as the fuel of choice. Biogas, derived from various biomass sources, is increasingly considered as a complement or substitute. The composition of biogas can vary widely depending on the percentage of the inert gas, e.g. nitrogen and carbon dioxide. If the variations in fuel compositions are high enough to affect combustion initiation, this may ultimately lead to adverse affects on engine performance and emissions. This point has been highlighted by Lieuwen et al. [67], suggesting that combustion properties of various fuel mixtures in a gas turbine combustor may behave in a highly nonlinear fashion.

Unlike natural gas that consists mostly of methane and other higher hydrocarbons, biogas contains a high percentage of carbon dioxide, whose varying compositions can lead to huge differences in flame temperatures. The typical composition is 15-40% carbon dioxide and 60-80% methane [68]. Depending on the source, diluent gases can comprise up to 51% of the fuel by molar volume [69]. This high carbon dioxide content can hinder flame kernel formation, lead to slower flame propagation, or even extinction of successfully ignited flames. Lean blowout and combustion instabilities of biogas-fueled gas turbines with high CO₂ dilution have been reported [70, 71]. Improved knowledge of the effects of CO₂ on forced ignition may suggest ways to overcome difficulties in the combustion of low caloric fuels such as biogas (e.g. flame kernel quenching).

To date, only a few studies have investigated laser ignition of methane and biogas. Forsich et al. [72] provided the first comparison of methane and biogas for fuel rich to fuel lean mixtures at pressures up to 3 MPa. The study focused on the formation of water near the spark

location and flame emissions, leaving out a detailed investigation into ignition energy. A key observation was that the presence of CO₂ contributed to lower burning velocities. Biet et al. [73] investigated ignition energies for methane and biogas for very lean conditions, concluding that the addition of CO₂ led to higher energy requirements. Results were compared with spark discharge ignition showing similar behavior at low pressures. For elevated pressures and near the lean flammability limit, ignition performance with the laser was superior to that of a spark discharge. Further experimental studies are needed to corroborate their findings, expand the range of investigated conditions, and include further visualization techniques that can offer more insight on the early phase of the ignition process. Additionally, improved understanding of the affects of CO₂ on early flame kernel growth and differences between the laser and spark ignition process need to be pursued as this can indicate the variable that must be taken into account in ignition modeling.

Ethanol is another fuel of practical interest which has not been extensively studied. Blends of gasoline fuels with ethanol, such as E10 (10% ethanol/90% gasoline) and E85 (85% ethanol/15% gasoline), are commonly used as automotive fuels. Fundamental research of the combustion properties of these blends has mainly focused on chemical kinetic modeling [74], burning velocities [75], and auto-ignition behavior [76]. Only a few studies on forced ignition have been carried out, comparing these fuels in optical IC engines and focusing on burning characteristics [77, 78]. It is observed that ethanol, as with other alcohols studied, shows faster flame propagation than iso-octane or gasoline. For laser ignition, ethanol has not garnered much attention. Kawahara et al. studied laser-ignited pure ethanol spray flames with varying degrees of water content [79] as well as premixed ethanol/air [80]. They found that some water content, up to 30%, improved combustion characteristics but with too much, greater than 30%, ignitability of the mixture deteriorated. Seo et al. [81] investigated the ignition energy of rich premixed and sprayed pure ethanol, both at $\phi = 1.59$. They found the breakdown threshold in premixed ethanol to be lower than premixed methane. Additionally, the breakdown threshold in ethanol sprays was much less than premixed ethanol. Laser

ignition behavior of ethanol under fuel lean conditions has not yet been fully addressed. Furthermore, laser ignition of iso-octane/ethanol blends has not yet been investigated. This fuel is more likely to be utilized in advanced combustion engines with laser ignition systems than pure ethanol fuel.

The ultimate goal of these laser ignition experiments is to develop a sufficient understanding of the controlling physics and thermochemistry to be able to predict and control successful ignition under various conditions. This will also facilitate the development of reduced order ignition models that can be incorporated in computational analysis of critical transient combustion phenomena.

1.2.4 Forced ignition modeling and simulations

Computer simulations of complex physical phenomena are a vital part of the research and development of combustion systems. They allow for performance evaluations of a given system through numerical investigations without the need for costly experiments and prototypes. In the combustion community, a sudden increase in forced ignition modeling occurred in the 1980's as emissions standards became more strict. The issue of successful ignition of lean fuel/air mixtures became of great importance since this reduces NO_x emissions. Predictive models were required to deal with this matter.

Early models in the area of electrode-based spark ignition were proposed by Adelman [82] and Maly [83]. Adelman gave the first model accounting for the temporal dependence of spark energy input. However, some key parameters were left out of the model. Energy losses from the spark kernel due to conduction, radiation, and convection were neglected. The thermal ignition model by Maly took into account the non-stationary nature of the ignition process. One important conclusion from this work is that to ensure successful ignition, energy should be introduced at the highest possible power and shortest time interval possible.

In 1988, Kono et al. [84] developed a model that was used to simulate sparks between opposed electrodes in inert gas and validated through experiments. Unsteady mass, momentum, and energy conservation equations were solved with the assumption that heat transfer to the spark electrodes can be neglected. They found that the gas flow pattern produced by the spark-initiated shock wave has the greatest impact on the evolution of the spark kernel. In a subsequent study by the same authors, the species conservation equation, heat transfer to the spark electrodes using Fourier's law, and a global one-step reaction was added to the model to simulate combustion of stoichiometric propane/air [85]. The global one-step reaction was, $C_3H_8 + 5O_2 + 18.8N_2 \rightarrow 3CO_2 + 4H_2O + 18.8N_2$, with the following Arrhenius form used for the reaction rate: $k = 4.0 \times 10^{13} \exp(-E/\bar{R}T) \times [C_3H_8]^{0.5} [O_2]^{0.5}$.

Another opposed electrode simulation was performed by Kravchik and Sher [86], this time incorporating detailed chemical kinetics for the combustion of methane/air. The model commences approximately 60 ns after breakdown where it assumed thermodynamic equilibrium has been reached. The initial conditions are then a plasma channel diameter of 0.24 mm, peak temperature of 35,000 K, and pressure of 1.01 MPa. Conservation equations solved are of the general form: $\frac{\partial}{\partial t}(\rho\phi) + \vec{\nabla} \cdot (\rho\vec{V}\phi - \rho\Gamma_\phi\vec{\nabla}\phi) = S_\phi$, where ϕ is the general dependent variable, Γ_ϕ its associated transport coefficient, and S_ϕ the source term. Statistical thermodynamics is then used to evaluate thermodynamic and transport properties of the plasma at high temperatures. They noted that the kernel growth was a two-step process. The first part is a short duration (1-5 μs) where mass and energy transfer occur via a pressure wave and expanding plasma kernel where effects from chemical reactions are negligible. The second process is a long duration where mass and energy transfer occur through diffusion and thermal conduction as the flame gradually becomes self-sustained.

In the 2000's more detailed spark ignition simulations were reported, complemented by more complex experimental diagnostics. Kaminski et al. [87] used planar laser-induced fluorescence (PLIF) to study turbulent spark ignition in methane/air and compared the results with direct

numerical simulations (DNS). The DNS included a detailed chemical kinetic mechanism with 17 species and 52 reactions and a detailed transport model. Concurrently, Thiele et al. [88] performed detailed simulations of spark ignition, modeling the electric field between electrodes and spark plasma channel along with the flow, chemical kinetic, and transport models. In a separate study, this model was validated using PLIF and temperature measurements based on coherent anti-Stokes Raman scattering spectroscopy (CARS) [89]. More recently, studies have moved beyond basic ignition models to study the effects of electrode geometry [90, 91], fuel effects [92], and spark ignition in non-homogeneous mixtures [93].

Laser ignition simulations on the other hand, are much less advanced. Yan et al. [94] proposed a simple model for laser energy deposition into quiescent air. In their study, plasma chemistry was neglected; only capturing the evolution of the flow field. Two simulations were performed and compared: a 3D numerical solution of the unsteady Euler equations and a one dimensional calculation in a spherical polar coordinate system. Energy from the laser pulse was modeled as being deposited instantaneously in a constant volume. The area of energy deposition was modeled as a spherical high temperature region with initial radius, r_0 , and Gaussian temperature distribution $\Delta T = \Delta T_0 e^{-r^2/r_0^2}$, where ΔT_0 is the peak temperature variation determined by the total energy deposited. This peak temperature was calculated using Equation 1.1 where E is the input energy and λ is the absorption rate of the input energy.

$$\Delta T_0 = \frac{\lambda E}{\pi^{3/2} \cdot r_0^3 \cdot \rho_\infty \cdot c_v} \quad (1.1)$$

Morsy et al. [95, 96] modeled and simulated the flame kernel development in laser ignited methane/air mixtures. A semi-global two-step reaction mechanism was used to obtain reasonable results. The focal volume was assumed to be cylindrical with length and radius defined using diffraction limited optical theory. The peak temperature and pressure in the focal volume were set at 10,000 K and 10 atm, respectively, with a Gaussian distribution normal to the laser beam. Little justification was given for this choice of initial temperature

and pressure in the focal volume. Along the laser beam axis, the peak temperature and pressure were shifted toward the laser source. The asymmetric energy deposition resulted in the formation of a front lobe emanating from the main body of the flame back toward the laser source, as observed in laser ignition experiments.

Ghosh & Mahesh [97] compared three different models of laser-induced breakdown in air in order to determine the minimum level of complexity required to capture the correct physics with reasonable accuracy. In the first model, chemical reactions were neglected. The properties of the gas were those of air, and assumed to be constant. For the second and third models, a mechanism consisting of 11 species for plasma kinetics was included. The second model considered the effect of temperature variation on the thermodynamic and transport properties of air. The third model considered the effect of both temperature and pressure variation on the properties of air. The equations of state for the second and third models, solved along with the compressible Navier-Stokes equations, are therefore, $p = \rho R(T)T$ and $p = \rho R(T, p)T$, respectively. For each model, the flow field was found to evolve in a qualitatively similar manner. However, significant differences were observed in the initial pressure fields.

Detailed simulations have also been performed by Koga et al. [98] for the laser-induced breakdown and ionization process in air and by Joarder et al. [99] for the flow field following optical breakdown in air, accounting for radiation losses. A simplified laser-induced breakdown model was proposed by Tartar et al. [100] with the aim of providing accurate predictions of breakdown with only moderate computing resources and minimum input data. This type of model, correctly capturing the physics at reduced computational requirements, would be very useful to engine development for the transportation and energy industries. With that methodology in mind, an extension of this work to reactive mixtures would be a welcome addition to the laser ignition literature.

1.3 Scope and objectives of this work

Following the motivation and literature review above, a number of persisting challenges were identified. Firstly, there is still need for improved understanding of the parametric dependence of laser-induced optical breakdown on focusing optics, thermodynamic conditions, and gas type. Secondly, the division of available absorbed energy for ignition after optical breakdown has only been studied in air. The ultimate goal of laser ignition studies is to obtain ignition models. In order to have accurate models of laser ignition, parametric dependencies must also be investigated for combustible mixtures. Thirdly, new diagnostics could be introduced to better understand the thermodynamic conditions and plasma kernel structure immediately after breakdown. This would allow for more rigorous validation of laser ignition simulations apart from the usual temporal evolution of the laser-induced shock wave front. Further, we need to understand the flame quenching behavior of laser-ignited flames under lean conditions since this can affect power output and emissions in combustion systems. Another deficiency in laser ignition literature is characterization of fuel structure and chemical composition effects on successful ignition. Finally, these characteristics of laser ignition are better appreciated by comparing them with characteristics of spark ignition. Resolving these questions can provide greater prediction and control capabilities for laser ignition systems. This thesis seeks to contribute to the resolution of these outstanding questions. Specifically, this work seeks to:

- investigate early stages of laser ignition with the aim of establishing the influence of focusing optics, thermodynamic conditions, and chemical structure of fuels on optical breakdown, shock wave dynamics, and ignition.
- quantify thermomechanical differences between breakdown in non-reactive and reactive mixtures to isolate the effect of exothermicity on plasma and shock wave propagation. Knowing the conditions of the gas (burned/unburned) near the focal volume and quantifying the additional energy release from combustion during the first microsecond

after breakdown are of importance. The knowledge gained will help to develop accurate initial conditions for microsecond resolved simulations based on absorbed energy and early kernel geometry. This eliminates the need for nanosecond resolution of the ignition process.

- employ interferometric imaging techniques to identify and explain plasma dynamics as well as early flame behavior especially near flammability limits. This will give insight into the mechanisms controlling quenching of fuel-lean laser ignited flames as well as the time-scales involved.
- put laser ignition into context by contrasting with spark ignition. The rationale is that contrasting these two very different plasma-based ignition techniques allows for a direct study of the effects of energy transfer duration, spark geometry, and plasma temperature on ignition.

It will also be discussed how these can be used to develop an improved laser ignition model in subsequent work.

Chapter 2

Experimental procedure and analysis

This chapter describes the experimental methods used to address the objectives outlined in the previous section. It also presents the method of analysis employed to derive understanding from the experiments. The experiments use a constant volume combustion chamber, laser, and spark plug. The ignition events are monitored using schlieren, interferometry, and pressure measurements. The analysis includes the use of blast wave theory to capture the laser-induced shock wave, two-color interferometry to characterize the early phase of the laser ignition process, and front tracking for flame dynamics.

2.1 Experimental setup

Constant volume combustion chamber

The laser ignition experiments are carried out in a cylindrical stainless-steel combustion chamber that is 15.24 cm in diameter and 25.4 cm long, as shown in Figure 2.1. Optical access is provided on six sides. Sapphire windows with diameters of 2 cm provide access for the laser. These windows are modified to accommodate a spark plug for studies focusing on spark ignition. Quartz windows with diameters of 9 cm on the end walls are used for imaging diagnostics. The chamber is connected to a central manifold which is used for gas

delivery. A vacuum pump (Edwards, RV5) connected to the manifold is used to evacuate the chamber. Ultra high purity compressed gases (Airgas, 99.999%) are also connected to the manifold. A pressure transducer (Omega PX309-030A5V) on the manifold is used for mixture preparation using the method of partial pressures. For combustible mixtures, fuels are added first, followed by oxygen and nitrogen. The mixture preparation process involves residual velocities within the chamber which lead to rapid homogenization before the start of the ignition experiment. The relatively short time required for proper mixing is confirmed through CFD simulations of the mixture preparation process. From a typical simulation, it is observed that 30 seconds after closing the inlet valve, the maximum deviation from the required mean mass fraction of fuel is less than 7%. This is further reduced before the experiments, which usually take place about 2-5 minutes after the valve closure. The mixture is assumed to be stationary and confirmed by the decay of velocities in the chamber after the valve closure to about 3 mm/s after 30 seconds.

A pressure transducer (PCB Piezotronics 113B24) is mounted on side of the chamber. The transducer is used to measure dynamic pressure in the chamber during the experiments. A silicon sealant (Dow Corning RTV 732) is applied to the transducer mount in order to protect the transducer from thermal shock. The transducer operates on the piezoelectric effect whereby an electric charge is produced in response to an applied mechanical stress in certain piezoelectric materials [101]. Quartz crystals are used in this transducer to produce an electrical signal proportional to the change in pressure.

Laser ignition setup

The laser-induced processes investigated in this work use an Nd:YAG laser (Spectra-Physics Quanta Ray Pro 250). The laser is capable of 4 harmonics but the 2nd harmonic at 532 nm is used for this study. The pulse duration is 8 ns, the beam diameter is 1 cm, and the maximum

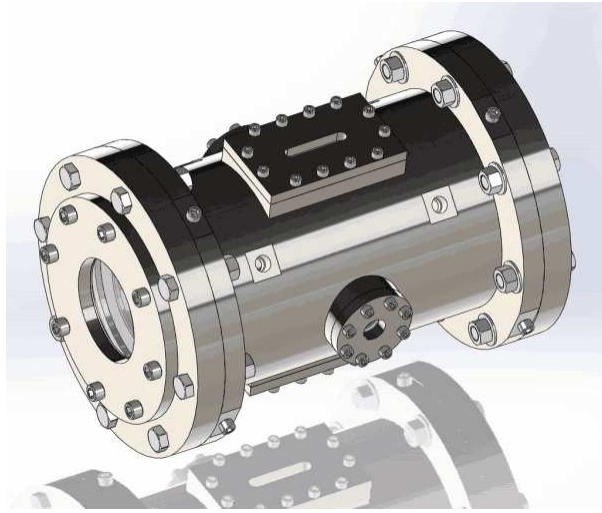


Figure 2.1: Outer view of constant volume combustion chamber, showing optical windows.

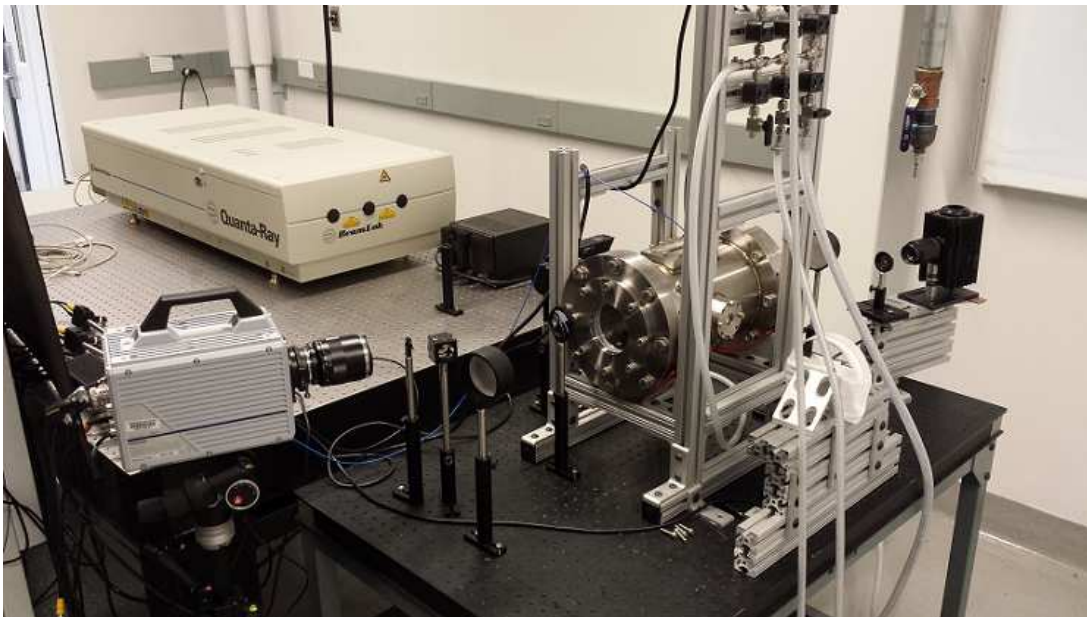


Figure 2.2: An overview of the experimental setup for laser ignition studies.

output is 800 mJ at the wavelength of 532 nm. The divergence of the laser beam is less than 0.5 mrad. Prior to reaching the focusing optics, a portion of the laser beam is redirected to a pyroelectric energy sensor (Ophir PE-25DIF) and power meter (Ophir Juno) by a variable attenuator (Thorlabs VBA05-532). The variable attenuator is calibrated to determine the split ratio at different settings. This allows for indirect determination of the incident laser energy. The laser beam is then focused to a spot inside the chamber by a 2.54 cm diameter convex lens. The residual energy after passing through the chamber is measured by a second pyroelectric energy sensor (Ophir PE-25) connected to a power meter. The absorbed energy inside the chamber is calculated by subtracting the residual energy from the incident energy. Reflective losses from the focusing lens (98% transmission) and sapphire windows (84.9% transmission) are taken into account when calculating the incident and absorbed energies. The accuracy of these calculations is confirmed by verifying that adopting them ensures that there is no absorption within the chamber under vacuum conditions. The laser ignition experimental setup is shown in Figure 2.2. A schematic of the setup including arrangement of the laser power meters is shown in Figure 2.3. This setup allows for the investigation of laser-induced breakdown, early phase of laser ignition, and the behavior of flames initiated by a focused pulsed laser beam.

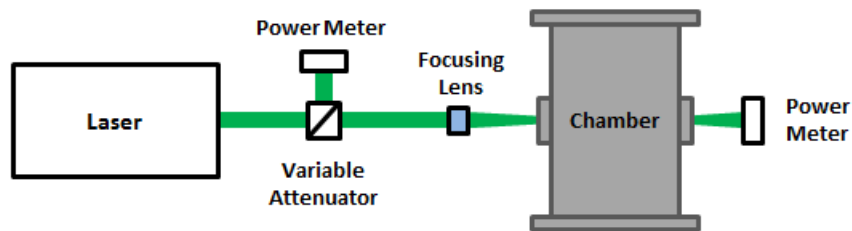


Figure 2.3: Experimental setup depicting the arrangement of laser power meters for measuring incident and absorbed laser pulse energies.

Spark ignition setup

The setup in Figure 2.2 is modified for spark ignition experiments. These experiments use a Champion 470 nickel copper alloy spark plug connected to an ignition coil (MSD Blaster) and powered by a 12V battery. The ignition circuit, as shown in Figure 2.4, is closed by a solid state relay (Omega SSRDC100VDC20) that is controlled by a Labview program specifying dwell times of the ignition coil. Dwell time is the amount of time during which the circuit is closed, allowing current to flow through the primary winding of the ignition coil. The current in the primary winding increases until it reaches a maximum which is dependent on the characteristics of the ignition coil. Upon opening the circuit, collapse of the magnetic field set up by the primary winding induces a current in the secondary winding, which if sufficiently high, causes dielectric breakdown in the spark plug gap. For this research, the dwell time is set at 5 ms which is a typical value for inductive discharge ignition systems [102].

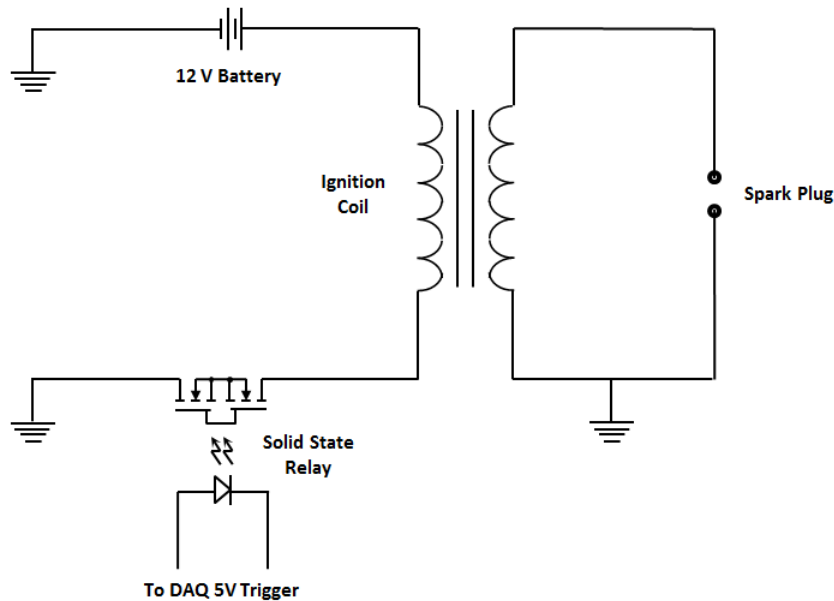


Figure 2.4: Spark plug ignition circuit.

The spark ignition system used in this study is similar to that used by Wolk et al. [103] where the energy was characterized to be 30 mJ. Energetic characterization for the current setup has not been performed. In light of this, the spark energy is estimated to be approximately 20-30 mJ.



Figure 2.5: Spark plug mounted in combustion chamber for spark ignition experiments.

A customized mount is used to hold the spark plug in the center of the chamber as shown in Figure 2.5. The mount is threaded into the optical ports on the side wall making the spark plug accessible for optical diagnostics. The mount is sealed through the use of o-rings and NPT threading to ensure that the chamber does not leak while still allowing the plug and ground wires to pass through to the spark plug.

Schlieren setup and hardware

Schlieren imaging is used to visualize the plasma, shock wave, and flame fronts during laser and spark ignition. In essence, schlieren imaging is a technique used to visualize density gradients based on the refractive index differences resulting from the gradients [104].

For this research, a Z-type schlieren system is utilized. The schlieren system is shown in Figure 2.6 with the laser ignition setup. A Light Emitting Diode (LED) is used as the light source. The light is focused to the center of a 0.9 mm adjustable iris. The opening of the iris is used to approximate a point source for the light. The light is then collimated between two 50 cm focal length mirrors. Next, part of the light is focused onto a knife edge and the remaining image is recorded by a high speed camera (Photron SA-4).

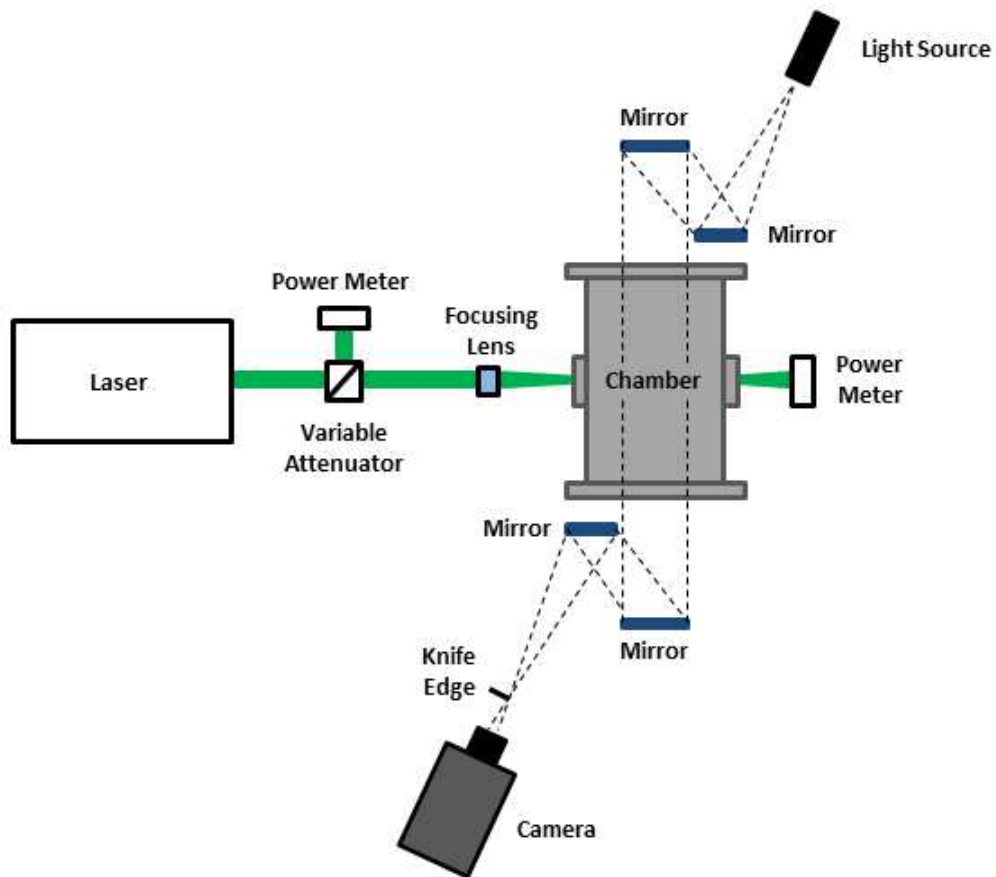


Figure 2.6: Schematic of the laser ignition experiment including the schlieren imaging system.

Interferometer setup and hardware

Like the schlieren imaging technique, interferometry picks up differences in refractive index. But unlike schlieren, interferometry measures refractive index changes relative to a reference so that the refractive indices and associated densities of the field can be measured. Here, the interferometer used is the Mach-Zehnder configuration as shown in Figure 2.7. The mirrors and beam splitters are 5.08 cm diameter, allowing a maximum viewing diameter of approximately 3 cm. The mirrors are of precision grade, $\lambda/10$ flatness, in order to reduce experimental errors due to the optics. The interferometer can be utilized using one or two light sources. A beam splitter combines the two light sources which then travel a common path through the interferometer. The light sources are a 10 mW Helium-Neon (He:Ne) laser (Thorlabs HNL100L) emitting at a wavelength of 633 nm and a 40 mW laser diode (Thorlabs DL5146-101S) emitting at a wavelength of 403.5 nm. Images are recorded using a high speed camera (Photron SA-4).

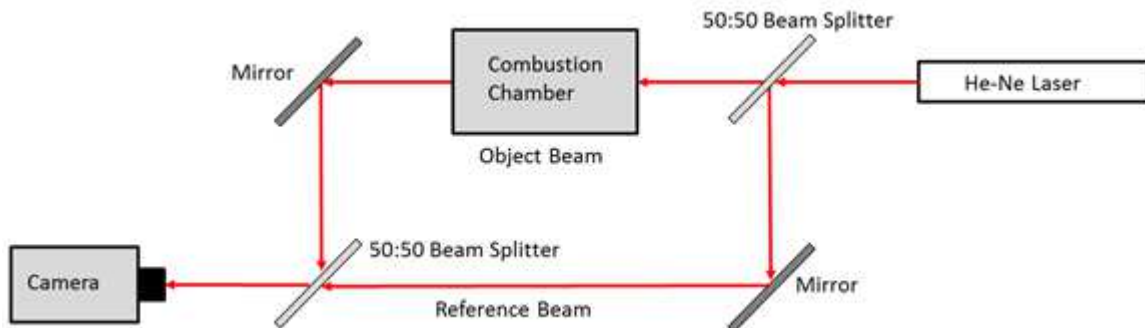


Figure 2.7: A schematic of the Mach-Zehnder interferometer used in this work.

Data acquisition hardware and software

The main data acquired in these experiments include high-speed images, signals from pressure transducers, and light emissions. These are timed with respect to the laser pulse or solid state relay. Because of the high speed and large file sizes involved, data acquisition is computer controlled. The computer-controlled acquisition of the data is realized using a National Instrument data acquisition board (USB-6356), LabVIEW programs, and hardware-specific

software packages. Different data acquisition setups are used for the laser and spark ignition experiments and are described below.

For laser ignition experiments, all data acquisition is triggered by the laser pulse. A digital delay generator (SRS DG645) is used to control the amount of time until data acquisition begins after the laser pulse. The high speed camera used for all optical diagnostics is triggered by the digital delay generator. The Photron camera software package is used to operate the high speed camera and to acquire the images. A LabVIEW program is used to acquire the pressure transducer data. A photodiode with a bandpass filter corresponding to the wavelength of the laser is used to synchronize the pressure transducer data with the images from the high speed camera. Laser energy is measured using the energy sensors and power meters previously described. The StarLab software package is used to control the power meters and for acquisition of the laser energy.

The spark ignition studies are controlled using a LabVIEW program. The program is used to trigger the solid state relay in the ignition circuit, firing the spark plug. At the same instance, the pressure transducer and the digital delay generator connected to the high speed camera are also triggered to begin data acquisition.

2.2 Principles of the experimental visualization techniques

The principles grounding schlieren and interferometry are outlined in this section. The section ends with a discussion of two-color interferometry.

2.2.1 Schlieren imaging diagnostic

Many phenomena of interest in physics and fluid dynamics cannot be observed directly. One example is a shock wave; an apparent discontinuity in a fluid which is normally invisible to

the naked eye. Certain imaging techniques are able to capture these phenomena by visualizing changes in the index of refraction of the fluid. Schlieren imaging takes advantage of the fact that optical inhomogeneities refract electromagnetic waves in proportion to the gradients of their refractive index. This is shown in the following equations for the components of the angular ray deflection in the x and y direction:

$$\epsilon_x = \frac{L}{n_0} \frac{\partial n}{\partial x}, \quad \epsilon_y = \frac{L}{n_0} \frac{\partial n}{\partial y} \quad (2.1)$$

where n is the refractive index, n_0 is the refractive index of the surrounding medium, and L is the path length along the optical axis [104]. The gradient of refractive index can be related to the prevailing density and temperature gradients. If one assumes ideal gas behavior, these are as follows:

$$\frac{\partial n}{\partial y} = \frac{n_0 - 1}{\rho_0} \frac{\partial \rho}{\partial y} = \frac{n_0 - 1}{T} \frac{\rho}{\rho_0} \frac{\partial T}{\partial y} \quad (2.2)$$

In schlieren imaging, the illuminance level corresponds to the first spatial derivative of refractive index. Therefore, phenomena such as shock waves, hot gas plumes, and low-luminescence flames, where density or temperature gradients are present, can be visualized.

2.2.2 Interferometry diagnostic

In order to extract more information about the changes in refractive index, a different imaging technique must be used. Laser interferometry allows for the direct measurement of changes in refractive index which can provide a wealth of information. There are many different types of interferometers. This work utilizes the Mach-Zehnder configuration, previously shown in Figure 2.7, for accuracy, simplicity, and low cost. Mach-Zehnder interferometers work by splitting a coherent light source into two separate paths, referred to here as an object and reference beam. For a finite fringe configuration, such as used in this work, the two beams are purposefully slightly misaligned. Along these two paths, the light travels slightly different

distances and when recombined, they are out of phase. This phase difference creates an interference pattern. If there is a disturbance in the path of the object beam that changes the refractive index, the path length of that light is also changed with respect to the reference beam. The result is a change in the interference pattern. For a Mach-Zehnder interferometer, this change is visualized as a shift in the fringe pattern where the change in refractive index occurred.

The change in fringe position can be related to the phase shift and the change in refractive index by [105]:

$$\Delta S = \frac{\Delta\phi}{2\pi} = \frac{1}{\lambda} \int_0^L [n - n_0] dl \quad (2.3)$$

where ΔS is the change in fringe number, $\Delta\phi$ is the phase shift between probe and reference beams, λ is the wavelength of the light source, L is the path length, n is the refractive index at the location of interest, and n_0 is the refractive index of the surrounding medium. For a 2π phase shift, the fringe shift is equal to one fringe and the optical path difference between the probe and reference beams is equal to one wavelength of the light source.

For axisymmetric phenomena, the change in fringe position as a function of refractive index can be given in polar coordinates as an Abel transform [106]:

$$\frac{\Delta\phi(y)}{2\pi} = \frac{2}{\lambda} \int_{r=y}^{r=\infty} [n(r) - n_0] \frac{2r dr}{\sqrt{r^2 - y^2}}, \quad \text{where } r^2 = y^2 + z^2 \quad (2.4)$$

where $\Delta\phi(y)$ is the phase shift and $n(r) - n_0$ is the local change in refractive index. Abel transforms are used in spherically or axially symmetric functions where three dimensional information is projected onto a two dimensional plane. This is the case for interferometric measurements using a high-speed camera with either a CCD or CMOS sensor. Since we are interested in determining the change in refractive index, this equation must be rearranged as

follows [106]:

$$n(r) - n_0 = -\frac{\lambda}{2\pi} \int_r^{r_\infty} \frac{\partial D(y)}{\partial y} \frac{dy}{\sqrt{y^2 - r^2}}, \quad \text{where } D(y) = \frac{\Delta\phi(y)}{2\pi} \quad (2.5)$$

Once the change in refractive index is determined, it can be related to change in density using the Gladstone-Dale relation [107]:

$$n(r) - n_0 = \kappa (\rho(r) - \rho_0) \quad (2.6)$$

where κ is the Gladstone-Dale constant, $\rho(r)$ is the local density and ρ_0 is the ambient density. The Gladstone-Dale relation essentially relates differences in refractive index to differences in density, postulating a relational constant. Finally, the equation of state can be used to determine temperature:

$$T = \frac{pM}{\rho R} \quad (2.7)$$

where p is pressure, M is the molar mass, and R is the gas constant.

Using interferometry, a number of thermodynamic properties can be quantified. The equations outlined above correspond to changes in index of refraction due to a single source. For plasma, which is a combination of electrons, molecules, atoms, and ions, the change in refractive index includes contributions from numerous sources. In order to define the thermodynamic state of plasmas, quantities such as electron and neutral species densities are of importance. These measurements require two-color interferometry in order to distinguish between the contributions to changes in refractive index arising from neutral particles from those arising from charged species. This is explained below.

Two-color interferometry

As explained above, for certain phenomenon, the changes in refractive index may include contributions from multiple sources. This is the case for plasma where the refractivity, β ,

defined as the index of refraction minus one ($n - 1$), is given as [108]:

$$\beta_{plasma} = (n - 1)_e + (n - 1)_m + (n - 1)_a + (n - 1)_i \quad (2.8)$$

In this equation the subscripts are, e : electrons, m : molecules, a : atoms, i : ions.

The contribution to the index of refraction in plasmas can be attributed to two main sources, free electrons and bound electrons in neutral species and ions [109]. For interferometric measurements, the phase shift, $\Delta\phi$, then becomes:

$$\Delta\phi = \Delta\phi_e + \Delta\phi_n \quad (2.9)$$

where $\Delta\phi_e$ is the phase shift due to electrons and $\Delta\phi_n$ is the phase shift due to neutral species (defined here as molecules, atoms, and positive ions).

The phase change due to free electrons is given as [110]:

$$\Delta\phi_e = -r_e\lambda \int_0^L \Delta n_e dl \quad (2.10)$$

where r_e is classical electron radius 2.82×10^{-13} cm, λ is the laser wavelength, and Δn_e is the change in electron density. The classical electron radius is the size the electron must have if it has no mechanical mass and instead all of its mass is due to its electrostatic potential energy [111].

The phase change due to neutral species is:

$$\Delta\phi_n = \frac{2\pi\beta}{\lambda\rho_0} \int_0^L \Delta\rho dl \quad (2.11)$$

where β is the refractivity related to index of refraction by $\beta = n - 1$, ρ_0 is ambient density at which β is specified, and $\Delta\rho$ is the change in neutral species density. The refractivity, β , is

nearly constant over the visible spectrum.

Interferometric measurements at a single wavelength only determine the overall change in refractive index. In plasmas, this is the summation of the change due to the sources previously mentioned. Alpher and White [112] introduced two-color interferometry as a way to decouple the change of refractive index due to free electrons from that of bound electrons in neutral species and ions. If measurements are then taken at two different wavelengths, λ_1 and λ_2 , producing respective phase shifts $\Delta\phi_1$ and $\Delta\phi_2$ and assuming β is independent of wavelength [109], the change in electron and neutral species densities, Δn_e and $\Delta\rho$ respectively, can be determined independently by:

$$\int_0^L \Delta n_e dl = \frac{1}{r_e} \frac{\Delta\phi_1\lambda_1 - \Delta\phi_2\lambda_2}{\lambda_2^2 - \lambda_1^2} \quad (2.12)$$

$$\int_0^L \Delta\rho dl = \frac{\rho_0}{2\pi\beta} \frac{\Delta\phi_1\lambda_2 - \Delta\phi_2\lambda_1}{\lambda_2/\lambda_1 - \lambda_1/\lambda_2} \quad (2.13)$$

An Abel transform, using Equations 2.4 and 2.5, can be used to spatially resolve these density values for axi-symmetric phenomena. Path integrated densities can be ascertained by:

$$\Delta n_e L = \frac{1}{r_e} \frac{\Delta\phi_1\lambda_1 - \Delta\phi_2\lambda_2}{\lambda_2^2 - \lambda_1^2} \quad (2.14)$$

$$\Delta\rho L = \frac{\rho_0}{2\pi\beta} \frac{\Delta\phi_1\lambda_2 - \Delta\phi_2\lambda_1}{\lambda_2/\lambda_1 - \lambda_1/\lambda_2} \quad (2.15)$$

In this work, two-color interferometry is used to measure neutral species density of the plasma immediately after spark and laser-induced breakdown. Single color interferometry is used to measure flame temperature at much later times when there are no significant contributions from free electrons to the index of refraction. Equipped with these principles, we can examine the early phase of the ignition process to determine electron density and temperature, as well

as the evolution of neutral molecules and ions. These thermodynamic conditions can then help us in properly characterizing the non-equilibrium processes that precede the emergence of a self-sustained flame.

2.3 Data processing

This section concerns the determination of quantitative information about shock wave dynamics, interferometry, and flame dynamics. Images obtained from schlieren and interferometry are processed using Matlab codes. The details of these codes are given below.

In order to determine the temporal evolution of the laser-induced shock waves, a Matlab code is used to extract the shock wave radius at a given time from schlieren images. The edge detection toolbox in Matlab is utilized to create a binary image with a black background and white lines where an edge is identified by changes in the image intensity. An example of a schlieren image of the shock wave and a post-processed image is shown in Figure 2.8. The shock radius is then manually extracted and scaled using a calibrated image. Two edges of the shock wave appear in the images due to the exposure time of the high-speed camera. The inner edge is chosen as the radius of the shock wave at the time the camera is triggered. Carrying out this analysis at different times with similar laser energy leads to a general picture of the temporal evolution of the shock wave.

Apart from the shock wave, the dynamics of the resulting flame can be also traced out. Locations of spark- and laser-ignited flames at different times are also extracted from schlieren images using a Matlab code. The temporal evolution of the flames are quantified by determining the distance between the lower edge of the flame front and a reference point of ignition as shown in Figure 2.9. The edge of the flame is detected by first examining an array of pixels along the center-line of the flame as shown in Figure 2.10a. The gradient of the image intensity along the center-line is plotted and the maximum gradient is used as the

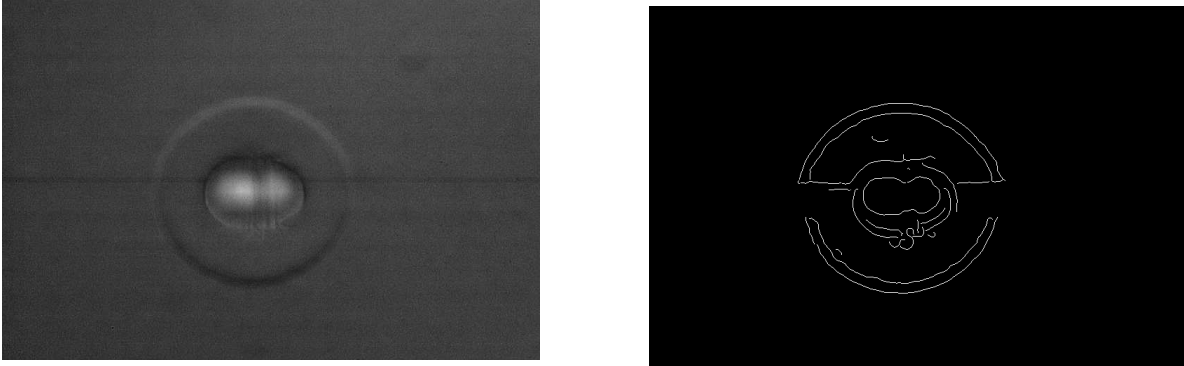


Figure 2.8: Schlieren image of laser-induced shock wave (left) and binary image showing edges of the shock wave (right).

flame front location. A plot of the gradient of the image intensity is given in Figure 2.10b. The flame location is then scaled using a calibration image. The schlieren images are read into the Matlab code in a loop to determine the temporal evolution of the flame. The time between schlieren images is determined from the frame rate of the high-speed camera. An example of the trajectory of a laser-ignited flame is given in Figure 2.11. These temporal evolutions allow for assessment of fuel and equivalence ratio effects on flame behavior and extinction.

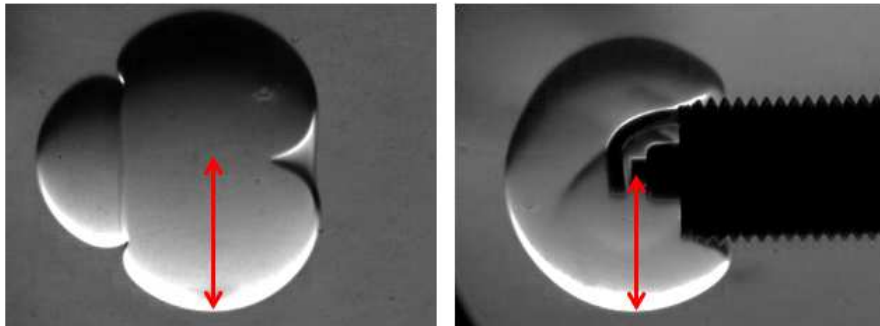


Figure 2.9: Quantifying the temporal evolution of the early flame kernels using the lower edge and the center of the energy reception focus.

Interferometric experiments should yield density and temperature fields. Figure 2.12 shows an example of a raw interferometric image of a laser-induced plasma and the associated shock wave at $1.5 \mu\text{s}$ after optical breakdown. A Matlab code is used to analyze the image by

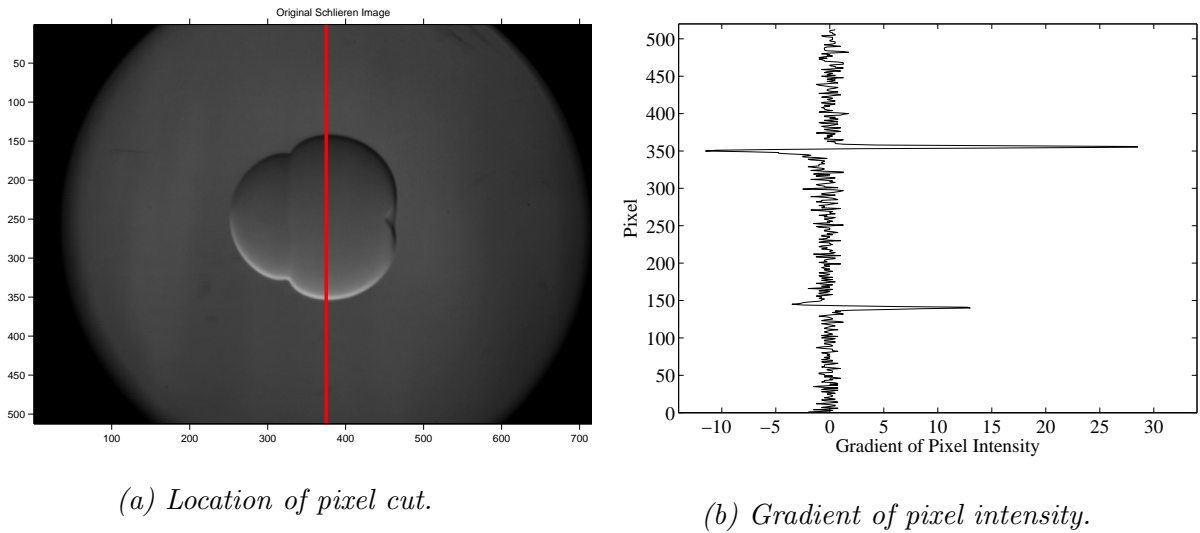


Figure 2.10: Schlieren image of laser-ignited flame showing location of analysis of the flame front and plot of the gradient of pixel intensity.

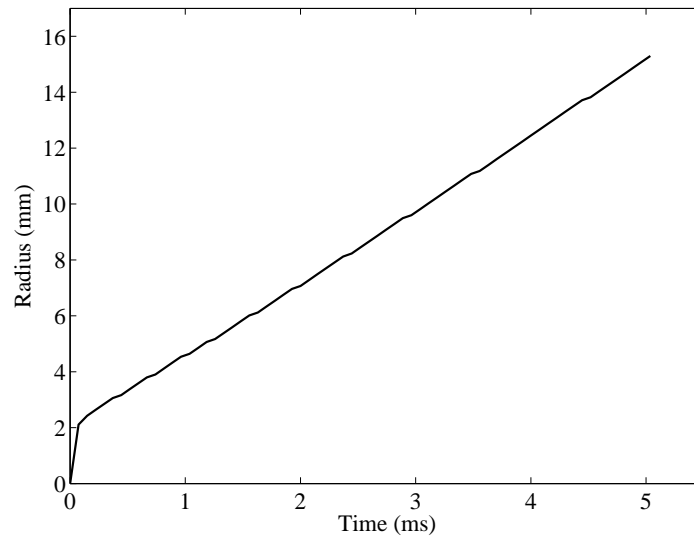


Figure 2.11: Example of the temporal evolution of a laser-ignited flame for a methane/air mixture at 1 atm and 300 K.

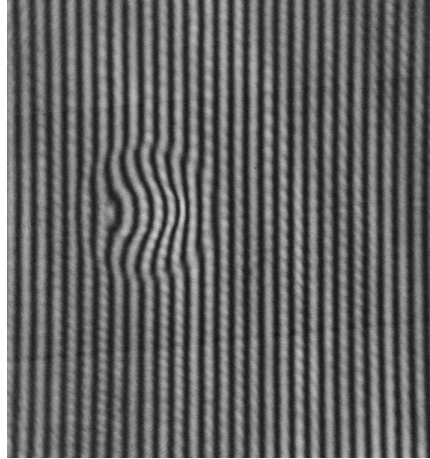
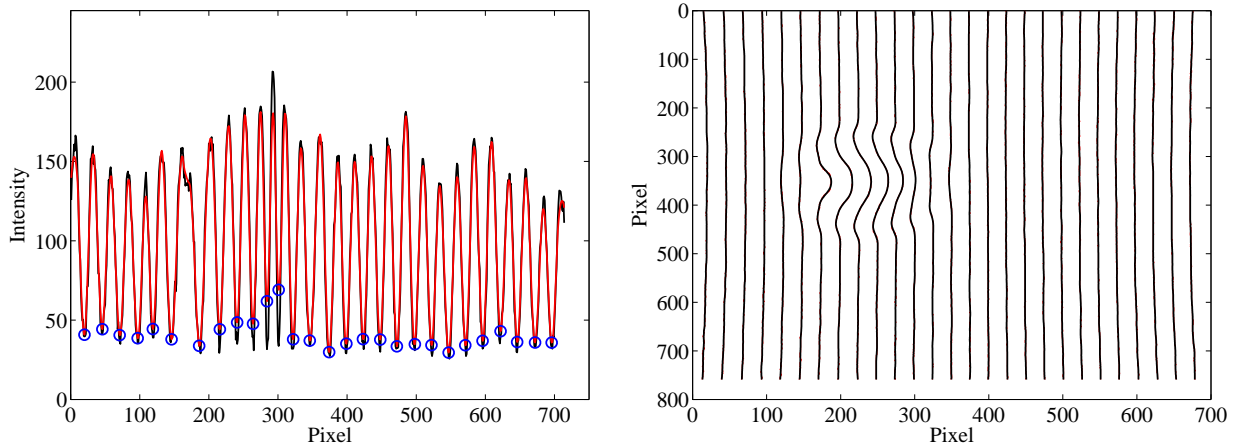


Figure 2.12: Interferometric image of laser-induced plasma and shock wave 1.5 μ s after optical breakdown.

discretizing the fringes, evaluating the fringe deflection, and computing the phase change. A more detailed description of this process is outlined below.

The first step in processing the interferometric images is discretizing the fringes. The Matlab code evaluates the intensity of each row of pixels in the image and locates the peak intensities, corresponding to the center of each fringe, as shown in Figure 2.13a. From this process, a matrix is produced containing the location, with respect to pixel number, of the center of each fringe which is plotted in Figure 2.13b. The distance between fringes is computed and the matrix is rescaled from pixels to fringe number. The undisturbed fringes along the edges of the image are then interpolated through the regions of localized fringe deflection, as shown in Figure 2.14a. From this, the magnitude of fringe displacement can be computed and multiplied by 2π to get the phase shift. The phase shift computed for this image is shown in Figure 2.14b. At this point, if one color interferometry is being used to study a flame, this result can then be used along with Equations 2.3 - 2.7 to calculate properties of interest such as density or temperature. For two-color interferometry, used here to study plasmas, further post-processing is required.

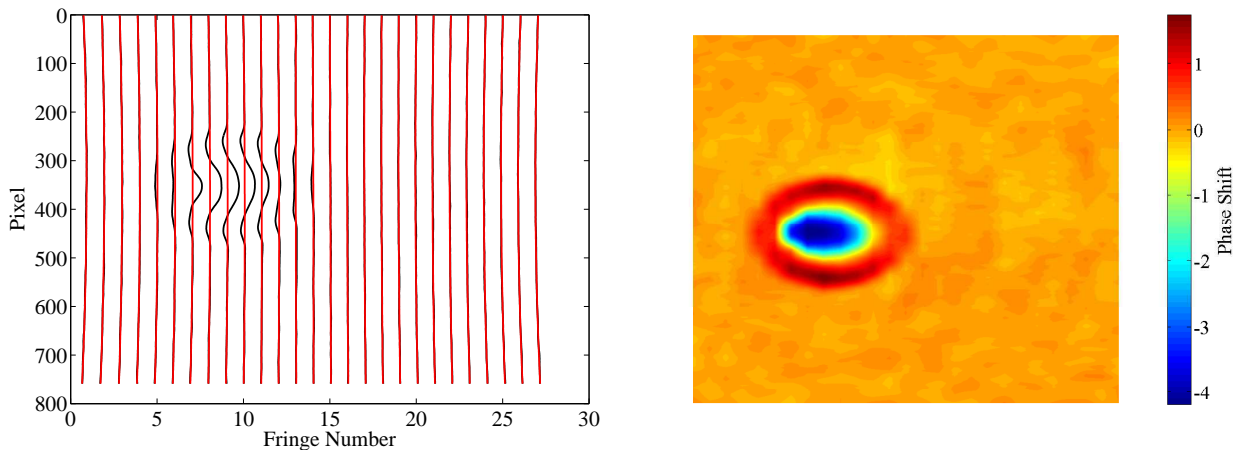
Two-color interferometry requires interferometric images to be recorded using two separate wavelengths from the coherent light sources. In this study, due to the limitation of having



(a) Pixel intensity and fringe locations (circles).

(b) Discretized fringes.

Figure 2.13: Pixel intensity plotted for a row of pixels from the interferometric image and the resulting discretized fringe locations.



(a) Undisturbed fringe location (red).

(b) Phase shift.

Figure 2.14: Discretized and undisturbed fringe locations used to calculate localized phase shift for interferometric images.

one high-speed camera, the images for the different wavelengths were recorded for separate spark- or laser-induced breakdown events. The energy for each breakdown event was held approximately constant in order to minimize shot-to-shot variations. Images for each wavelength are processed using the method previously outlined up to the point of calculating the phase shift for each image. The two images are then used to calculate path integrated gas

and electron densities using Equations 2.14- 2.15. If spatially resolved properties are needed, an Abel transform is performed and used with Equations 2.12- 2.13. Thus, it is possible to obtain quantitative data by combined use of the equations outline previously and image processing described here. These quantified findings can also be used in combination with simulations of the problem to shed light on the various contributions.

2.4 Outline of experiments

The objectives identified at the beginning are investigated and presented in three sections. The first section, Chapter 3, details the early phase of laser ignition. Chapter 4 investigates thermochemical effects on laser ignition by highlighting how fuel composition affects different phases of the ignition process. Finally, Chapter 5 explores how the ignition process can be dependent on the type of ignition system by comparing and contrasting laser and spark ignition. Further information about what is studied in each of these chapters and the experiments performed are detailed below.

Chapter 3 discusses the physics of the very early stages of laser-induced breakdown and ignition; up to 10 μs after breakdown. The optical breakdown threshold is discussed. A parametric study is undertaken to elucidate the influence of focusing optics, thermodynamic conditions, and fuel/air composition of the gas on this threshold. For focusing optics, the concentration will be on the focal length and how this affects the breakdown threshold. The focal lengths studied are in the range from 2.5 to 30 cm. Thermodynamic conditions will focus on changes in pressure, from 0.25 to 2.15 atm. Finally, fuel/air composition is also considered as optical breakdown thresholds in methane and biogas mixtures are compared with breakdown in air. A universal representation of the breakdown threshold is then utilized to facilitate comparison of the focal length and pressure measurements. Next, the dynamics of the plasma kernel and laser-induced shock wave are discussed. Schlieren imaging of the laser-induced

shock wave is used in conjunction with blast wave theory to determine how much energy is used to generate the shock in non-reactive and combustible mixtures. The combustible mixtures are methane/air and biogas/air at various equivalence ratios. Interferometry is utilized to capture the structure and thermodynamic conditions of the plasma kernel in non-reactive and combustible mixtures. The case of optical breakdown in air is then compared with results from CFD simulations.

The effects of fuel composition on laser ignition are discussed in Chapter 4. Minimum ignition energies for various fuels that are of interest to transportation and power generation are measured. These fuels include methane, biogas (60% CH₄, 40% CO₂), iso-octane, and E85 (85% ethanol, 15% iso-octane). Interferometry is used to investigate flame kernel structure and temperature for methane with varying degrees of CO₂ dilution. The different amounts of dilution, 25-50%, are used to simulate variations in biogas composition. Schlieren imaging is utilized to look at flame kernel development and the transition to a self-sustained flame for methane and biogas. Further, measurements of dynamic pressures inside the combustion chamber are used to highlight thermochemical effects of fuel/air compositions on the propagation of successfully ignited flames.

Finally, Chapter 5 highlights similarities and differences between laser ignition and conventional spark ignition. Interferometry is used to compare laser and spark produced plasmas in air. For combustible mixtures, schlieren imaging is utilized in conjunction with dynamic pressure measurements to contrast flame development for the two ignition technologies for methane, biogas, iso-octane, and E85 at different equivalence ratios.

Throughout the course of this work, a few parameters that are normally kept constant will be varied in order to highlight their effect on the ignition process. To avoid confusion, unless explicitly stated otherwise, the initial conditions inside the combustion chamber before ignition are room temperature (295 K) and pressure (1 atm), a focal length of 15 cm is used for laser ignition, and the biogas composition is 60% CH₄ and 40% CO₂.

2.5 Laser ignition simulations

In collaboration with Deshawn Coombs, a PhD student in our group, CFD simulations are used to compliment and validate experiments on laser-induced shock waves, yielding a better picture of the underlying physics. The rationale is that laser-induced breakdown and ignition involves a vast array of time and length scales. Numerical simulations provide access to earlier time resolutions and the associated flow field which can be difficult to determine experimentally. With a better understanding of the important physical characteristics, reduced-order models can be developed which accurately capture the relevant physics at reduced computational cost.

In this work, simulations of the laser-induced shock wave focus on optical breakdown in ambient air. The Navier-Stokes equations are solved using the commercial software Star-CCM+. The Navier Stokes equations in vector form can be written as,

$$\frac{\partial \mathbf{U}}{\partial t} + \frac{\partial}{\partial x_j} (\mathbf{F}_j^C - \mathbf{F}_j^V) = \mathbf{S} \quad (2.16)$$

where \mathbf{U} is the vector of conservative variables, \mathbf{S} is the source term vector, and \mathbf{F}_j^C and \mathbf{F}_j^V are the inviscid and viscous flux terms, respectively. The physical model used is explicit unsteady and the solution is advanced in time using a five step Runge Kutta method. In order to maintain stability of the simulation, particularly at early times where velocities are high, a linear CFL ramp is used to define the time step. The initial CFL number is 0.05 and starting at the 500th iteration, relaxes to a CFL of 0.5 by the 10,000th iteration. The solver is second order in space. Oscillations near the shock wave are controlled by the use of the Venkatakrishnan limiter.

In this study, the plasma is assumed to be in local thermodynamic equilibrium and the ideal gas model is used. Transport properties, such as conductivity and dynamic viscosity,

are modeled using a power law. The temperature dependence for specific heat is modeled using a polynomial equation. Chemical reactions in the plasma kernel as well as radiation heat transfer effects are neglected. A 2D simulation is performed due to the symmetry of laser-induced plasmas. These assumptions lead to the following expressions for the terms in the Navier-Stokes equations,

$$\mathbf{U} = (\rho, \rho u_i, \rho e)^T \quad (2.17)$$

$$\mathbf{F}_j^C = (\rho u_i, \rho u_j u_i + p \delta_{ij}, u_j (\rho e + p))^T \quad (2.18)$$

$$\mathbf{F}_j^V = (0, \tau_{ij}, u_i \tau_{ij} + q_{ij})^T \quad (2.19)$$

The simulation is performed on an 800,000 cell structured mesh. A rectangular domain of 1.25 cm by 2.5 cm is utilized with the center-line collinear to the incident laser beam being a symmetry axis. This gives a minimum cell size of 2.0833×10^{-5} m. The initial volume of energy deposition is assumed cylindrical in shape with radius and length prescribed using optical theory. This will be discussed in further detail in Chapter 3. Therefore, a rectangular shape for the initial plasma is used in the 2D simulation. Energy deposition is assumed to occur at constant volume by prescribing an initial temperature and pressure within the focal volume.

$$T_f = T_0 + \frac{E_a}{m \cdot c_v} \quad (2.20)$$

$$m = \frac{p_0 \cdot V_0}{R_g \cdot T_0} \quad (2.21)$$

$$p_f = p_0 (T_f/T_0) \quad (2.22)$$

The temperature after breakdown, T_f , based on the absorbed laser energy, E_a , is calculated using Equation 2.20. In this equation, T_0 is the initial gas temperature, c_v is the specific heat at constant volume, and m is the mass of the gas inside the focal volume. The mass is calculated

from the initial condition of the gas using the equation of state given in Equation 2.21. Once the temperature after breakdown is prescribed, the associated pressure after breakdown, p_f , is calculated using the equation of state as shown in Equation 2.22. The temperature and pressure are assumed constant over the focal volume.

Chapter 3

Laser-induced breakdown and shock wave dynamics

Laser ignition is a complex problem that includes many different processes occurring over a wide range of length and time scales. The early phase of laser ignition is particularly dynamic. The processes during this phase include: (1) optical breakdown creating an electrically conducting plasma (2) emergence of a shock wave due to the quick deposition of energy and (3) internal dynamics of the plasma kernel which eventually influences the dynamics of an emerging flame. An approximate timeline showing the time scales on which these processes occur is given in Figure 3.1. The processes leading up to the emergence of a flame kernel occur in a similar manner whether the optical breakdown occurs in a non-reactive mixture or a combustible mixture. As highlighted in the introduction to this work, this part of laser ignition is still not well understood. In particular, most fundamental studies on this phase of the laser-induced breakdown and ignition processes have taken place in air and have not quantified the differences in combustible mixtures. By comparing optical breakdown events in air with those of combustible mixtures, we may be able to gain more insight into what takes place during this very critical stage of the ignition process.

In this chapter three aspects of the early phase of laser ignition will be investigated. The first

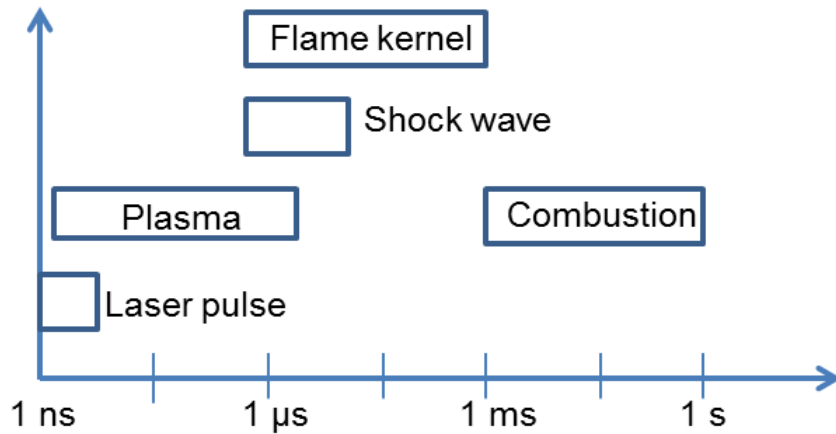


Figure 3.1: Approximate timeline of laser ignition from the start of the laser pulse to the end of combustion.

is the optical breakdown and the dependence of the breakdown threshold on focal length of the focusing optics, the pressure, and gas composition. It will end with a universal representation of the results. The second part will focus on the dynamics of the laser induced shock wave in air and in reactive mixtures. The blast wave theory will be used to interpret the dynamics of the shock front. It will end with ongoing collaboration using CFD simulations to reveal the shock induced flow field.

3.1 Laser-induced breakdown threshold

As previously mentioned, the first part of the ignition process is breakdown. The laser pulse energy or power density required to cause optical breakdown is called the breakdown threshold. This value is typically around 10^{11} W/cm². The exact threshold depends on a number of factors including characteristics of the incident laser beam, thermodynamic conditions of the gas, and the type of gas in which breakdown occurs. Below the breakdown threshold, the focused beam is transmitted through an optically transparent gas, which does not result in plasma formation and energy absorption. Knowledge of the threshold is therefore important for combustion initiation in engines to avoid misfires.

In this section, the focus will be on studying the effects of three main parameters on the breakdown threshold: focal length, pressure, and gas composition. The choice of focal length for laser ignition in combustion systems will largely be influenced by engine geometry. This could be vastly different depending on the intended application. For example in small automotive engines, short focal lengths would be required, however, in large gas turbines or spark ignition engines for power generation, long focal lengths may be needed in order to optimize the ignition point. Combustion systems also operate over a wide range of pressures and fuel compositions. It is critical that changes in these parameters do not lead to the inability to successfully initiate combustion. Therefore, these three parameters are among the most important to quantify in order to implement laser ignition in combustion systems.

In this work, optical breakdown thresholds are determined by the schlieren imaging technique to discern successful or unsuccessful breakdown events. For each gas at each condition, 30 breakdown attempts are recorded. Since optical breakdown is a stochastic event near the threshold, logistic regression of the data is then utilized to determine the point at which the probability of successful breakdown is 50%, setting this value as the breakdown threshold. There are two sources of uncertainty for these measurements. There is a 3% uncertainty due to the power meter accuracy and a precision error estimated as $\pm 5\%$ of the probability based on the logistic regression of the data. The overall uncertainty is calculated as the root sum of the squares of both uncertainties. An example of the logistic regression for one of the data sets, identifying the breakdown threshold and the precision error, is shown in Figure 3.2.

3.1.1 Effect of focal length on breakdown threshold

The method outlined above is applied to determining the optical breakdown threshold in atmospheric air for focal lengths from 2.5 to 30 cm. The results for the incident laser energy required for breakdown, E_B , are plotted in Figure 3.3. The energy required for breakdown decreases with focal length until it reaches a minimum at 5 cm, then increases again at 2.5

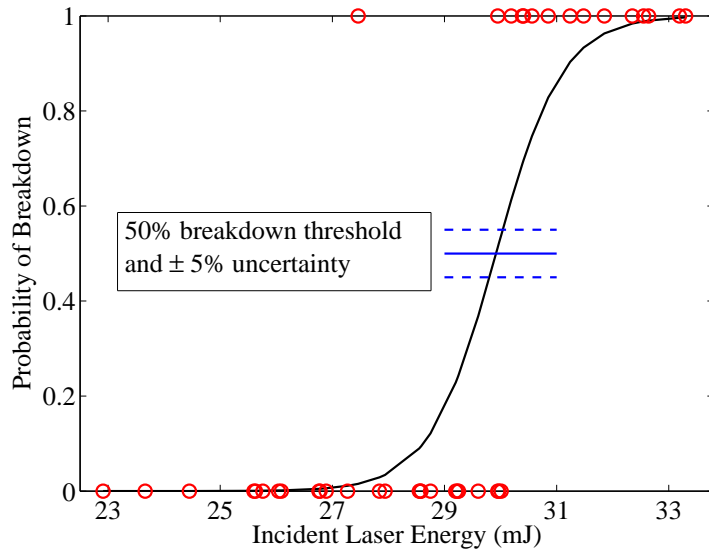


Figure 3.2: Logistic regression for breakdown in air using a focal length of 25 cm. Red circles signify successful (1) and unsuccessful (0) breakdown events.

cm. The increase in energy at focal lengths below 5 cm is consistent with results by Bak et al. [113]. They attributed the increase at lower focal lengths to an increase in the distortion of the laser pulse wavefront due to spherical aberrations.

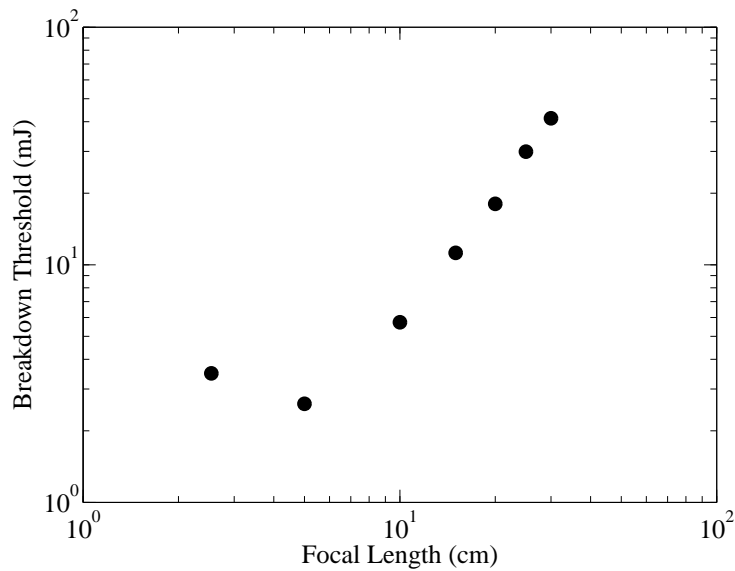


Figure 3.3: Variation of breakdown energy threshold with lens focal length. The gas is air at $T = 300\text{ K}$, $p = 1\text{ atm}$.

As the focal length decreases, the laser beam is more tightly focused and a lower incident energy is required to produce the same intensity of laser light in the focal volume. For a gas at a given initial condition and molecular structure, it is of interest to know whether this intensity stays constant. To test this, the previous results can be converted to a power density, I_B in W/cm², by using Equation 3.1.

$$I_B = \frac{1}{\pi} \left(\frac{E_B}{r_0^2 \tau_p} \right) \quad (3.1)$$

$$r_0 = f(\alpha/2) \quad (3.2)$$

In this equation, τ_p is the laser pulse duration and r_0 is the focal spot radius [22]. An estimate for the focal spot radius can be made using the diffraction-limited spot size from optical theory, given by Equation 3.2, where α is the divergence of the laser beam [19].

The diffraction limited spot size, typically used in optical breakdown threshold calculations, is the theoretical minimum focal volume that can be achieved for a perfectly focused Gaussian beam. In reality, spherical aberrations can arise in focusing optics due to light at the outer edges of the lens being focused to a different point than the light near the center. The presence of spherical aberrations therefore means the actual focal radius of the laser beam is larger than the diffraction limited radius. The effect of spherical aberrations on the focal radius increases for shorter focal length lenses. Aspheric or doublet lenses can be utilized to help minimize spherical aberrations. In this work, plano-convex lenses are used, therefore, spherical aberrations must be accounted for when converting the energy threshold, E_B , to power density, I_B . The increase in the focal spot diameter, d_a , can be determined from:

$$d_a = k(n, p, q) \left[\frac{D_L}{f} \right]^3 s_2 \quad (3.3)$$

Where f is the focal length, D_L is the diameter of the top hat beam mode of the incident laser beam on the focusing lens, and s_2 is distance from lens. Here the function k depends on

n , p , and q in the manner,

$$k(n, p, q) = \pm \frac{1}{128 n (n - 1)} \left[\left(\frac{n + 2}{n - 1} \right) q^2 + 4 (n + 1) p q + (3n + 2) (n - 1) p^2 + \frac{n^3}{n - 1} \right] \quad (3.4)$$

Where n is the index of refraction, q is the lens shape factor (1 for plano-convex), and $p = 1 - 2(f/s_2)$ [114].

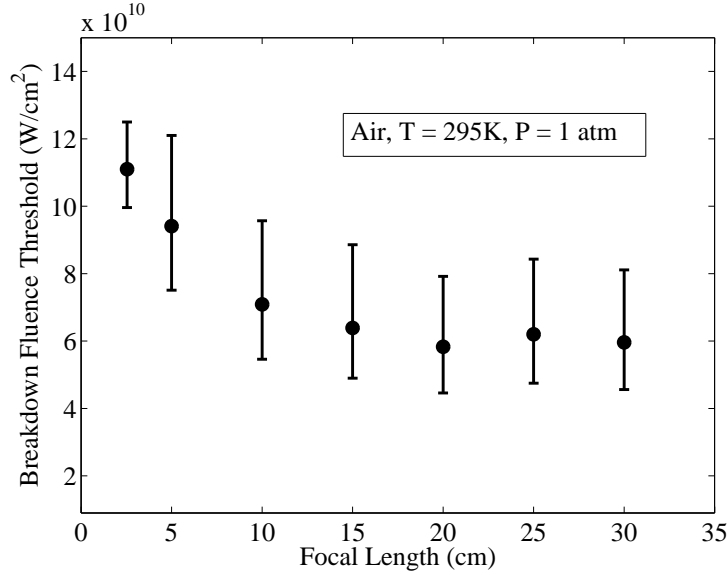


Figure 3.4: Variation of breakdown power density threshold with lens focal length, accounting for spherical aberrations due to the focusing lens. The gas is air at $T = 300$ K, $p = 1$ atm.

With these considerations and corrections, the results for breakdown threshold over a range of focal lengths are shown in Figure 3.4. The large errors in the power density values are due to the uncertainty about the divergence of the laser beam used in the calculation of the focal spot radius since this can vary from the initial value given by the manufacturer. Here it is considered that the nominal value is 0.35 mrad with an error of ± 0.05 mrad. Given the systematic nature of the error, the trend revealed is unaffected by the error size. We see that, accounting for spherical aberrations, the power density remains fairly constant for focal lengths that are 10 cm or longer. There is a slight increase at shorter focal lengths. This behavior has also been observed by other researchers and may be due to diffusion

losses [17, 18, 21]. For very short focal lengths and therefore small focal volumes, there may be an appreciable number of electrons diffusing out of the plasma region during the breakdown process.

3.1.2 Effect of pressure on breakdown threshold

The same experimental procedure above is used for a single focal length of 15 cm to investigate the effect of pressure on the breakdown threshold in air. The range of pressures used here is 0.25 to 2.15 atm. The results for breakdown threshold in terms of energy, E_B , and power density, I_B , are shown in Figures 3.5 and 3.6, respectively.

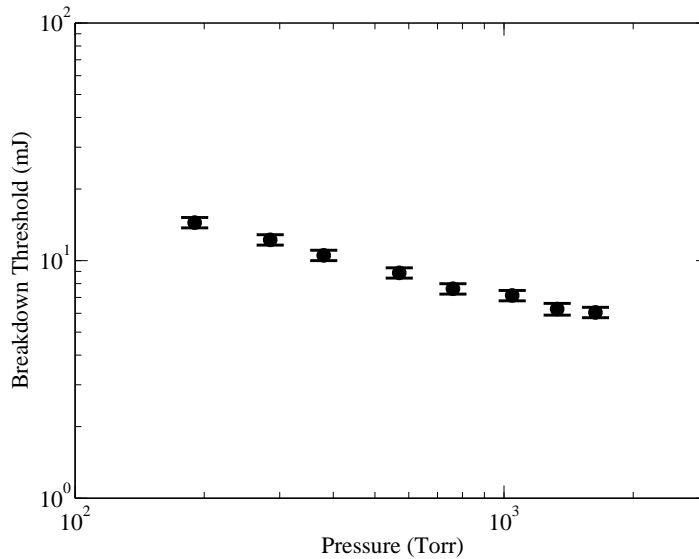


Figure 3.5: Variation of breakdown energy threshold with chamber pressure. The gas is air at $T = 300\text{ K}$ and a focal length of 15 cm.

The breakdown threshold is observed to decrease with pressure. This trend is contrary to that of spark plugs which follow Paschen's Law [115] and whose breakdown threshold increases with pressure. The laser behavior is advantageous since combustion systems are increasingly designed to operate at higher pressures. Reduced energy requirements for breakdown at elevated pressures would mean that smaller laser systems can be used, thereby reducing their

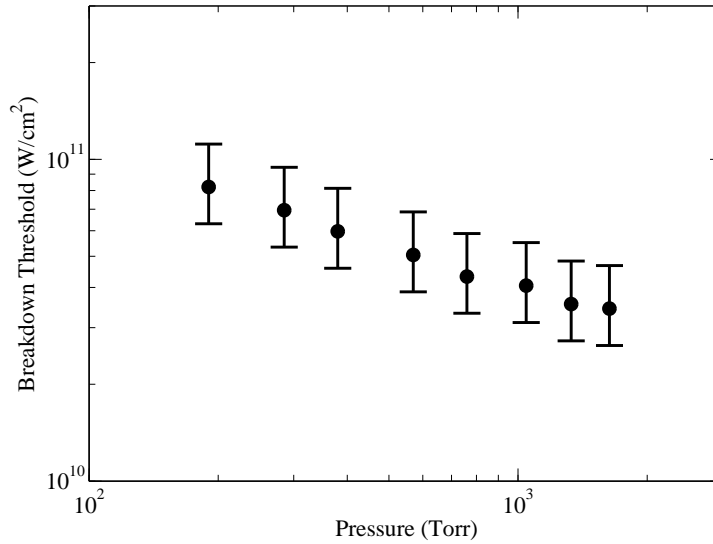


Figure 3.6: Variation of breakdown power density threshold with chamber pressure. The gas is air at $T = 300$ K with a lens of $f = 15$ cm. The larger uncertainty is associated with errors in the estimate of focal geometry.

cost and weight.

3.1.3 Effect of gas composition on breakdown threshold

It has been reported in the literature that the nature of the gas plays an important role in the breakdown threshold. For pure gases, which have received the greatest attention, large variations in the threshold value are observed. Relatively few studies have focused on mixtures of gases, especially combustible mixtures. Those that have studied fuel/air mixtures have investigated heavy fuels, such as cyclohexane and diesel fuel. Their results showed no differences in the breakdown threshold. But this might be due to the rather small proportion of fuel in mixtures of large hydrocarbons with air. The proportion of fuel in the mixture would be higher for mixtures of light hydrocarbons and air. However, the breakdown threshold in fuel/air mixtures of light hydrocarbon fuels has not been investigated. Some of the first applications of laser ignition are likely to use lighter fuels, such as methane. It is therefore

important to extend the analysis of breakdown threshold to these types of fuel/air mixtures.

To study the effect of gas compositions on breakdown threshold in combustion systems, the breakdown threshold for air was compared with that of fuel/air mixtures of methane and biogas (60% CH₄/40% CO₂) at an engine relevant equivalence ratio of $\phi = 0.65$. This test was conducted for the same range of pressures previously outlined. The breakdown energy threshold, E_B , for all three gases studied is shown in Figure 3.7 as a function of pressure. It is observed that all the gases have the same breakdown threshold, within experimental error, at all the pressures studied. The power density, I_B , is shown in Figure 3.8.

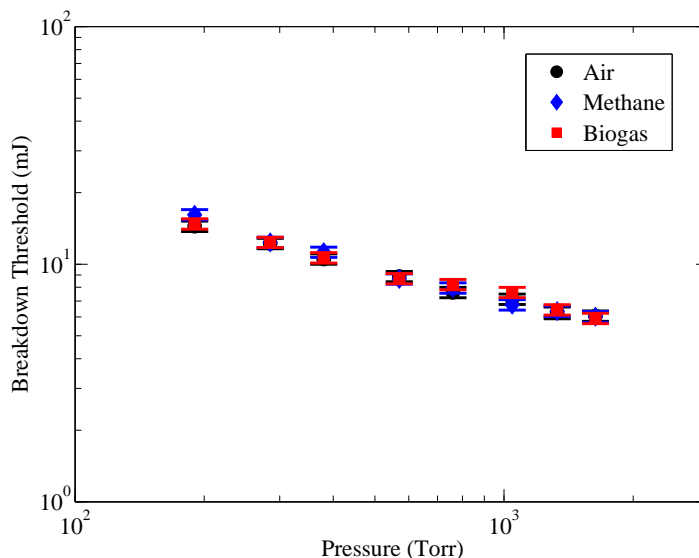


Figure 3.7: Breakdown energy threshold for air and mixtures of methane/air and biogas/air at $\phi = 0.65$, $T = 300$ K, and $f = 15$ cm.

The breakdown threshold measured here has a pressure dependence of approximately $p^{-0.4}$ for all gases. This follows the form of p^{-n} in accordance with the inverse bremsstrahlung absorption process for laser-induced breakdown observed by other researchers [116, 50, 14]. In this mechanism, initial free electrons in the gas and those produced through multiphoton ionization are accelerated by further absorption of the laser photons. With sufficient energy, the electrons can ionize molecules and create more free electrons through collisions in a process called collisional cascade. As such, the ionization potential of the gases might explain

the observed trends.

The ionization potentials of oxygen and nitrogen are 12.07 eV and 15.58 eV, respectively. The mean ionization potential for air is therefore greater than the ionization potential of methane which is 12.61 eV. In studies of pure gases, such as the one by Phuoc [2], this results in a lower breakdown threshold for methane than air. For combustible mixtures, where the amount of fuel is small compared to air, the effect of CH_4 is negligible. This is also true even for biogas with the addition of CO_2 , which has a lower ionization potential than air of 13.8 eV. These results show that the first step in the ignition process, breakdown, is minimally affected by changes in fuel composition for engine relevant equivalence ratios for light hydrocarbon fuels. This study therefore establishes that under similar environmental conditions, laser breakdown thresholds are not strongly sensitive to combustion gas type or ionization potential differences, since any significant differences in ionization potentials are masked by the higher percentage of nitrogen and oxygen in the fuel/air mixture.

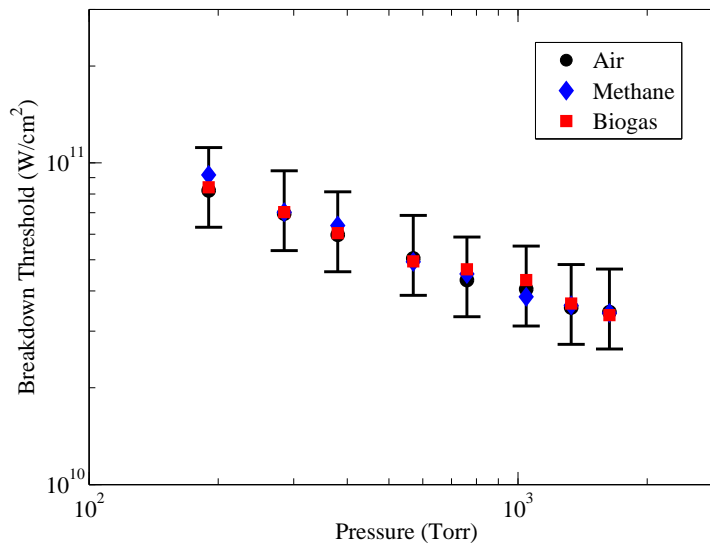


Figure 3.8: Breakdown power density threshold for air and mixtures of methane/air and biogas/air at $\phi = 0.65$, $T = 300$ K, and $f = 15$ cm.

3.1.4 Universal representation of breakdown threshold

In order to improve our understanding of laser-induced breakdown, it is beneficial to have a universal representation of the parameters affecting breakdown threshold, independent of the applied frequency of the electromagnetic radiation. This facilitates comparison of experimental data with theoretical predictions as well as comparing distinctly different types of breakdown (e.g. optical and microwave breakdown). The procedure for creating a universal representation has been reported previously in literature and is briefly outlined here [19, 22, 117].

The breakdown power density threshold, I_B , as previously measured, is obtained from the breakdown energy threshold, E_B :

$$I_B = \frac{1}{\pi} \left(\frac{E_B}{r_0^2 \tau_p} \right) \quad (3.5)$$

Since the laser light is an electromagnetic wave, the associated electric field can be calculated from the power flux of the laser using:

$$E_{field} = 1.94 \times 10^4 \sqrt{I_B} \quad (3.6)$$

For high frequency electromagnetic waves, the strength of the electric field required for breakdown varies with the applied frequency. The concept of an effective electric field was purposed to remove the effect of applied frequency in order to compare breakdown processes caused by wavelengths across the electromagnetic spectrum. This allows for a comparison of the effectiveness of the electric field in coupling its energy to the electron. The actual electric field, E_{field} , is therefore converted to the effective electric field, E_{eff} , using:

$$E_{eff} = E_{field} \left(\frac{v_c^2}{v_c^2 + \omega^2} \right)^{1/2} \quad (3.7)$$

Which under certain circumstances can be considered an equivalent DC field.

The electron collision frequency can be calculated by $\nu_c = \beta \times 10^9 p$, where p is in torr. The parameter β is dependent on the gas and is 5.3 for air [22]. The applied frequency is calculated as $\omega = 2\pi (c/\lambda)$, with c and λ being the speed of light in a vacuum and applied wavelength, respectively. For laser frequencies in the range studied here, $(\omega/\nu_c) \gg 1$, Equation 3.7 can be simplified to:

$$E_{eff} \approx E_{field} \left(\frac{\nu_c}{\omega} \right) \quad (3.8)$$

A few crucial parameters contributing to breakdown, besides the electric field strength, must be accounted for in order to allow for a universal representation. One of these, the frequency of applied energy, has been accounted for by E_{eff} . Another contributing factor is the pressure of the gas in which breakdown occurs. Finally, the spatial scale over which this energy deposition occurs is important. This can be accounted for using a characteristic length scale called the diffusion length, Λ . This is essentially the distance over which a particle should diffuse in order to be lost from the plasma [117]. The diffusion length, Λ , for laser focused plasmas is given,

$$\left(\frac{1}{\Lambda} \right)^2 = \left(\frac{\pi}{l_0} \right)^2 + \left(\frac{2.40}{r_0} \right)^2 \quad (3.9)$$

This equation takes into account the focal volume of the laser beam. The diffraction limited volume is defined by the radius, $r_0 = f(\alpha/2)$, and length, $l_0 = (\sqrt{2} - 1) (\alpha/d) f^2$, where f is the focal length, α is the divergence of the laser beam, and d is the diameter of the unfocused beam.

Using the method outlined above, data can be compared over a wide range of frequencies, pressures, and diffusion lengths. In this work, the results of pressure and focal length dependence on breakdown, presented previously, are compared with microwave breakdown data and a theoretical threshold for breakdown by collisional cascade processes. The theoretical collisional cascade calculations come from an empirical correlation derived from microwave

breakdown data by MacDonald [117]. The threshold power density is given by,

$$I_{B(CC)} = 1.44 \times 10^6 (p^2 + 2.2 \times 10^5 \lambda^{-2}) \quad (3.10)$$

In previous studies, this theory has been extended to optical wavelengths as short as 193 nm.

In Figure 3.9, the effective electric field times diffusion length, $E_{eff}\Lambda$, is plotted as a function of the product of pressure and diffusion length, $p\Lambda$. Pressure and focal length data can now be plotted together along with the theoretical calculations for collisional cascade and microwave breakdown. A scaling factor of 1.9 was used for the focal length measurements and 2.2 for the pressure measurements to facilitate comparison with collisional cascade theory. This scaling factor was used by other researchers as well in construction of a universal plot [19, 22]. Two main factors contribute to the necessity of this scaling factor for comparison. Firstly, although extended to a wavelength of 532 nm in this work, the collisional cascade theory was formulated from microwave breakdown data at pressures well below atmospheric. This may lead to discrepancies when extrapolated to much different conditions. Additionally, theoretical calculations do not account for the presence of water vapor and dust particles in the air which can significantly reduce the breakdown threshold through concentrated photon absorption [118].

In general, good agreement between the trends for the pressure and focal length data is observed. Additionally, both data sets have reasonable agreement with collisional cascade theory. This result shows that for the breakdown process at this wavelength, collisional cascade dominates over multiphoton ionization as expected for a laser wavelength of 532 nm. Slight differences can be seen for low pressures between the pressure data and focal length data as well as collisional cascade theory. Multiphoton ionization becomes more prominent at low pressures and this may be reflected by the slight deviation in the pressure data far below 1 atm.

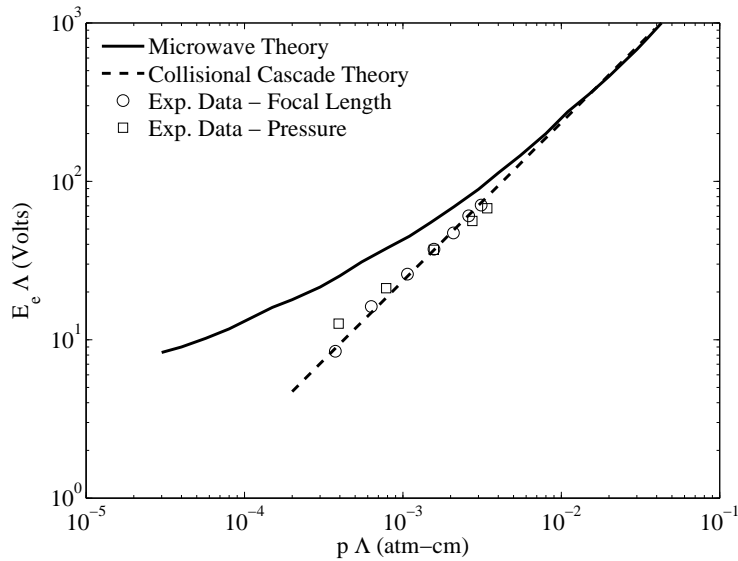


Figure 3.9: Universal plot for laser-induced breakdown in air at $T = 300$ K showing results for focal length and pressure.

From the foregoing, it can therefore be said that the effects of pressure and focal length on the plasma formation process are such that they admit of a unified theoretical account. The plasma formation process for the laser wavelength studied here, 532 nm, accords with the collisional cascade theory.

3.2 Dynamics of laser-induced shock waves

Immediately following breakdown, a high temperature plasma kernel is produced. Accompanying this process is the formation of a shock wave which detaches from the plasma kernel within the first microsecond after breakdown. The shock wave is formed due to the much shorter time scale of laser energy deposition compared to the acoustic time scale of the gas. Pressure waves created from the laser energy deposition therefore coalesce into a shock wave which then distributes energy away from the focal volume to the surrounding gas.

There is minimal quantitative information in the literature on the characteristics of plasma

kernels and shock waves in combustible mixtures or the effects of gas composition on such waves. However, it is after this stage that exothermic chemical reactions initiate the formation of a flame kernel which will determine whether or not successful ignition is achieved. It is therefore critically important to determine whether gas type and composition have an effect on this early stage of the ignition process. In this work, the shock wave propagation is used in conjunction with the blast wave theory to facilitate comparison of laser-induced breakdown in non-reactive mixtures with the early phase of ignition for methane and biogas.

3.2.1 Blast wave theory

The blast wave theory was developed in the 1940's for studying the evolution of spherically expanding strong shock waves. In essence, it gives the temporal evolution of a shock front

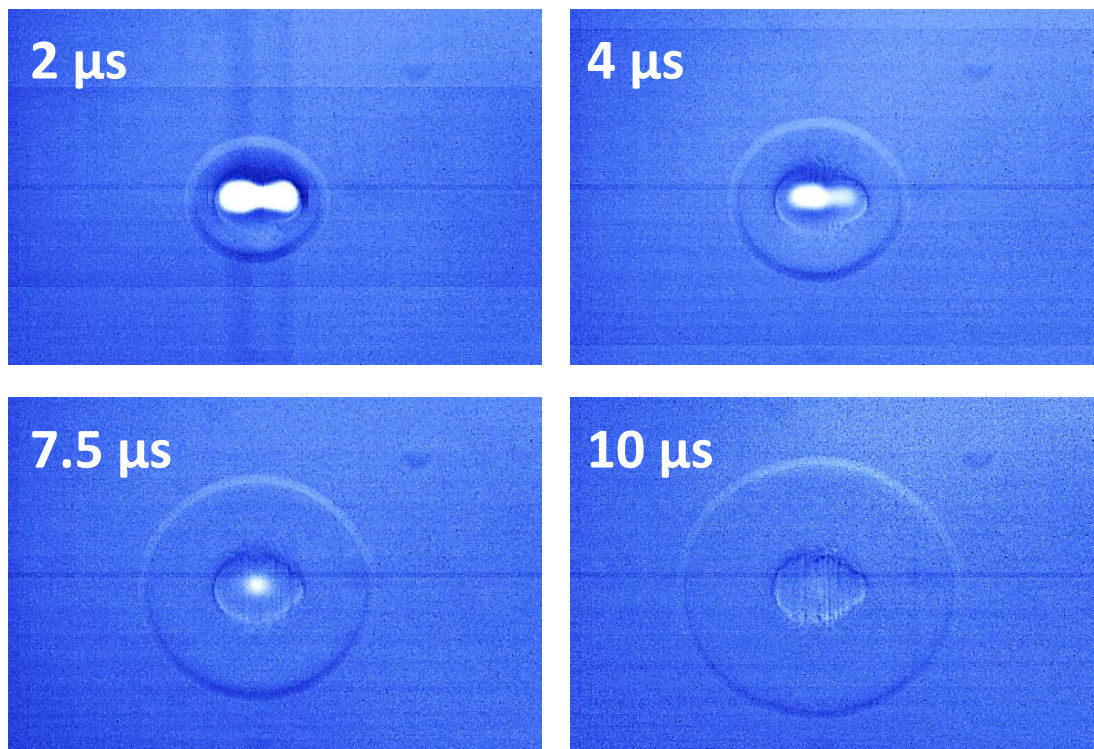


Figure 3.10: Schlieren images showing the evolution of a laser-induced shock wave in air.

emanating from a point-like rapid deposition of a given amount of energy. Self-similar solutions to this problem were independently derived by Taylor [42] and von Neumann [119]. During this time period, the aim of this work was to study thermonuclear detonations. Therefore, the equations were derived assuming a very high pressure gradient across the shock front. This is only true for strong shock waves with high Mach numbers. A number of subsequent models were derived independently, extending the range of conditions captured by the models to shock waves of intermediate strength as well as cylindrical and plane shock waves. The same general assumptions are used in each of the theoretical solutions. The main assumptions are: (1) the energy is assumed to be instantaneously released from a single point (2) the shock is similar in all directions at all times, changing only its linear dimensions with time (3) the gases involved are perfect with constant specific heat ratios and (4) energy losses from ionization and radiation are neglected.

Using the blast wave theory, the temporal evolution of a shock front can be determined given the initial energy input. Conversely, if the distance of a shock front from its origin is measured as a function of time, the blast wave theory can be applied to deduce the energy required to produce the shock wave. Additionally, when combined with the Rankine-Hugoniot shock relations, the conditions at the shock front including velocity, pressure, and temperature can be computed.

Gebel et al. [41] recently compared many blast wave models to see how well they fit experimentally obtained trajectories for laser-induced shock waves in air. Their results show the blast wave models by Brode [120] and Jones [121] most accurately describe the shock radius evolution. The often used Taylor-Sedov blast wave theory [42] only captures the dynamics of the laser-induced shock wave well at very early times. However, at times greater than about $2 \mu\text{s}$ the shock wave begins to propagate below Mach 2 and the Taylor-Sedov solution is no longer valid. The Jones blast wave theory is therefore used in this work to find the point blast energy which best fit the experimentally obtained shock wave trajectories. A comparison of

the Taylor-Sedov and Jones blast wave theories with an experimental data set is shown in Figure 3.11.

The equation developed by Jones for the evolution of a strong to intermediate strength spherically expanding shock wave is:

$$\tau = 0.543 \left[\left(1 + 4.61x(t)^{5/2} \right)^{2/5} - 1 \right], \quad (3.11)$$

where τ and $x(t)$ are non-dimensional quantities such that,

$$\tau = c_0 \frac{t}{r_0} \quad (3.12)$$

$$x(t) = \frac{r(t)}{r_0} \quad (3.13)$$

$$r_0 = \left[\frac{6.25E_0}{B\gamma p_0} \right]^{1/3} \quad (3.14)$$

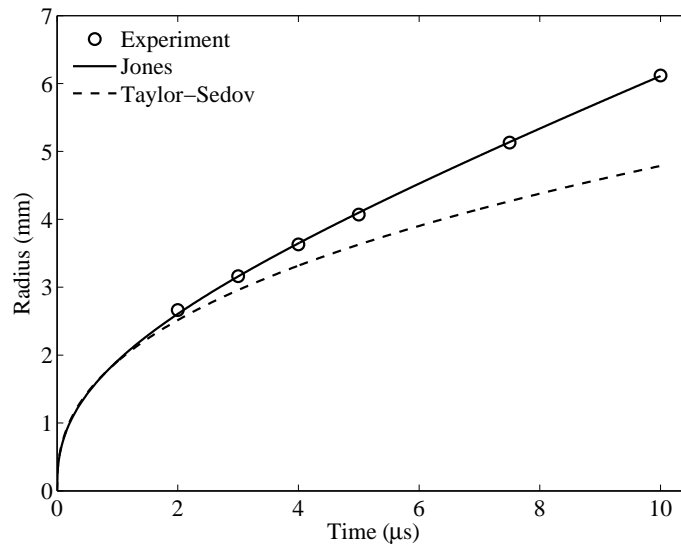


Figure 3.11: Comparison of Taylor-Sedov and Jones blast wave theories with experimental data for 25.2 mJ of absorbed laser pulse energy in air at $T = 295$ K, $p = 1$ atm. Both blast wave theory calculations use a point blast energy of 22.4 mJ.

Here, t is the dimensional time, r is the radius, r_0 is the reference radius, c_0 is the speed of sound, γ is the specific heat ratio, p_0 is the pressure of the undisturbed gas, and B is a numerical constant depending on the geometry of the shock wave and the specific heat ratio, γ . The equations to calculate B are given in [122] and are summarized below.

B is the integral of a geometry dependent function of a series of distribution functions developed to represent pressure, density, and flow velocity at all points in the blast wave. The distribution function f is related to the pressure ratio across the front, ψ the density ratio, and ϕ the radial velocity of the front. In order to compute B , given by Equation 3.15, it is necessary to integrate the differential equations of the distribution functions following Equations 3.16 - 3.18.

$$B = 4\pi \int_0^1 \left(\frac{1}{\gamma(\gamma-1)} f + \frac{\psi \phi^2}{2} \right) \eta^2 d\eta \quad (3.15)$$

$$\frac{df}{d\eta} = f' = \frac{f [-3 \cdot \eta + \phi (3 + 1/2 \cdot \gamma) - (2 \cdot \gamma \cdot \phi^2) / \eta]}{(\eta - \phi)^2 - f/\psi} \quad (3.16)$$

$$\frac{d\phi}{d\eta} = \phi' = \frac{(1/\gamma) (f'/\psi) - 3/2 \cdot \psi}{\eta - \phi} \quad (3.17)$$

$$\frac{d\psi}{d\eta} = \psi' = \frac{\psi [\phi' + 2(\phi/\eta)]}{\eta - \phi} \quad (3.18)$$

In these equations, the independent, η , is a dimensionless variable given by the ratio $\eta = r/R$ where R is the distance from the origin to the shock front and r is an intermediate point. To initialize the computation, boundary conditions at the shock front are required. The boundary conditions are given by [122]:

$$f_1 = \frac{2 \cdot \gamma}{\gamma + 1} \quad ; \quad \phi_1 = \frac{2}{\gamma + 1} \quad ; \quad \psi_1 = \frac{\gamma + 1}{\gamma - 1} \quad (3.19)$$

The distribution functions are first evaluated to create a table of values from $\eta = 0$ to 1. Next, B is found by numerically integrating from the table. In this work, the Runge-Kutta method (RK4) is used for evaluating the distribution functions and Simpson's rule is utilized for numerical integration of the parameter B . The values obtained for the gases used in this work are provided in Table 3.1.

	Air	CH ₄ /N ₂	CH ₄ /Air $\phi = 1$	CH ₄ /Air $\phi = 0.6$	Biogas/Air $\phi = 1$	Biogas/Air $\phi = 0.6$
γ	1.400	1.390	1.389	1.393	1.382	1.388
B	5.319	5.461	5.475	5.417	5.579	5.490

Table 3.1: Values for the ratio of specific heats, γ , and geometry parameter, B , for gases used in this study.

In this work, the blast wave theory outlined above is used to compare the strength of laser-induced shock waves in various gases. In conjunction with Equation 3.11 and experimentally obtained shock radii, a least-squares method is used to determine the initial energy, E_0 , required to produce the observed shock wave.

3.2.2 Laser-induced shock waves in combustible mixtures

The propagation of laser-induced shock waves is captured in six different mixtures using schlieren images. The six gases are: air, a stoichiometric methane/air mixture, an equivalent non-reactive methane mixture where air was replaced with N₂, a stoichiometric biogas/air mixture, a lean methane/air mixture at $\phi = 0.6$, and a lean biogas/air mixture at $\phi = 0.6$. Due to limitations on the speed of the camera used in this study, a single image at a specified delay time is recorded for each breakdown event. The delay times are set at 2, 3, 4, 5, 7.5, and 10 μs using a digital delay generator connected to the camera and triggered by the laser

pulse. Five breakdown events at a fixed laser pulse energy are averaged for each delay time. The incident laser pulse energy is kept within $\pm 3\%$ and absorbed laser energy within $\pm 4\%$ to ensure good shot-to-shot reproducibility. Three different laser pulse energies are used to induce the shock waves. For these laser pulse energies, the absorbed laser energies, E_{absorbed} , are 3.8 ± 0.15 mJ, 12.2 ± 0.3 mJ, and 25.2 ± 0.5 mJ. The captured images are scaled with distance calibrations and a Matlab code, outlined in Chapter 2, is then used to determine from the schlieren images, the shock radii at different times. Once the temporal evolution of the shock front is obtained, the energy required to reproduce this shock trajectory can be deduced using the blast wave theory.

There are three main sources of uncertainty for the shock wave radius measurements: (1) variability in the laser deposition energy (2) errors due to scaling of the shock wave images and location of the shock front as determined by the Matlab code and (3) time delays between the triggering and camera image acquisition. Precision errors due to variability in the absorbed laser energy by the gas are reported in the first column of Table 3.2. The reported values are $+/-$ one standard deviation. Since the shock wave radius scales with energy, a polynomial fit between the shock radius and energy is used to correlate how the uncertainty in energy corresponds to an uncertainty in the shock wave radius. For the lowest absorbed energy, 3.8 mJ, the uncertainty in radius due to variability in energy is ± 0.017 mm. The highest absorbed energy, 25.2 mJ, has an uncertainty of ± 0.022 mm. The precision error associated with scaling and uncertainty in the shock front from the Matlab code is ± 2 pixels, which corresponds to ± 0.069 mm. The greatest uncertainty in the shock front position at a given time is due to a bias error of up to $0.5 \mu\text{s}$ in the time at which the image is captured. There is a 100 ns uncertainty associated with the Q-switch trigger on the laser and digital delay generator used to trigger the camera. Up to a 400 ns uncertainty is associated with the time between the trigger input to the camera and the lens opening. The time uncertainty was multiplied by the approximate velocity of the shock wave at each time delay in order to determine the uncertainty in the position of the shock front. The overall uncertainty,

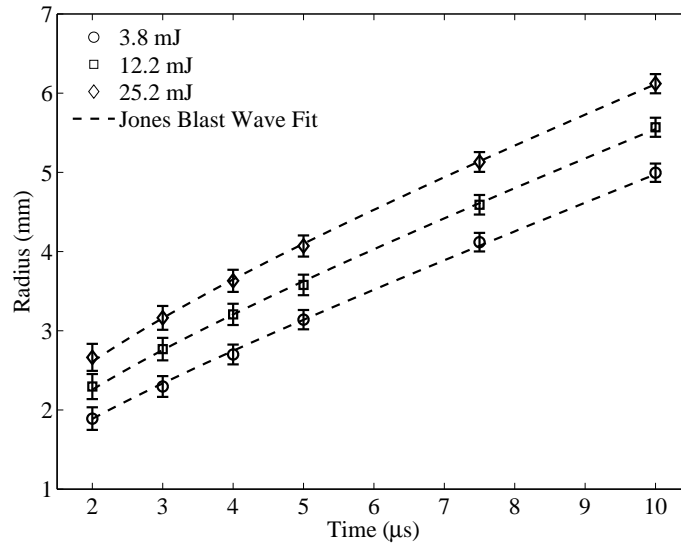


Figure 3.12: Experimental data (symbols) and Jones blast wave theory (lines) for three different absorbed laser pulse energies in air at $T = 295\text{ K}$, $p = 1\text{ atm}$.

represented by the error bars in the figures in this section, is the square root of the sum of the squares of the precision and bias errors reported here.

The experimentally obtained shock wave trajectories and corresponding curve fit using the blast wave theory for air at three different absorbed laser energy levels are shown in Figure 3.12. As expected, the shock radius scales with absorbed energy. The highest absorbed energy produces a shock wave encompassing the greatest area at a given instance in time. From the blast wave theory, this corresponds to the largest point blast energy required to produce the shock wave.

The point blast energies determined from the experimental data using the blast wave theory are provided in Table 3.2, compared with the absorbed laser energy during breakdown. For 25.2 mJ of absorbed energy, the point blast energy for air was found to be 22.4 mJ, which is 89% of the absorbed energy. This is in accordance with other researchers who have reported blast wave energies accounting for up to 95% of the absorbed laser energy [99].

The point blast energies for stoichiometric methane/air are appreciably higher than those in

$E_{absorbed}$	Air	CH ₄ /N ₂	CH ₄ /Air $\phi = 1$	CH ₄ /Air $\phi = 0.6$	Biogas/Air $\phi = 1$	Biogas/Air $\phi = 0.6$
25.2 ± 0.5	22.4	22.6	25.5		24.7	
12.2 ± 0.3	9.9		11.2	10.6		
3.8 ± 0.15	3.4		4.5	4.0		3.8

Table 3.2: Point blast energies, in mJ, calculated using Jones blast wave theory compared to absorbed laser energy, $E_{absorbed}$, in mixtures at $p = 1$ atm, $T = 295$ K.

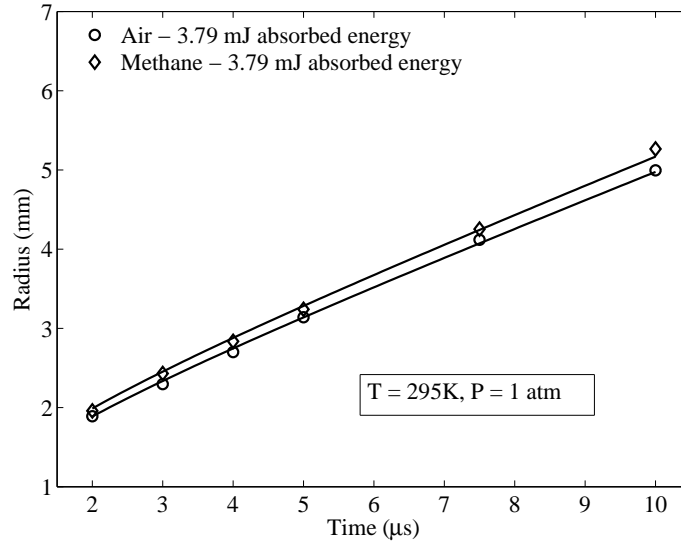


Figure 3.13: Experimental data (symbols) and Jones blast wave theory (lines) for 3.79 mJ of absorbed laser pulse energy in air and methane at $T = 295$ K, $p = 1$ atm.

air for all three energy levels investigated. For the lowest energy level, $E_{absorbed} = 3.8$ mJ, the point blast energy for stoichiometric methane/air is higher than the absorbed laser energy. The higher point blast energies indicate that there is additional energy release within one microsecond after breakdown, after which time the shock wave detaches from the plasma kernel. This is likely due to combustion of the fuel/air mixture near the focal volume, caused by the extreme thermodynamic conditions within the plasma kernel. A comparison of the shock wave trajectories for air and methane is give in Figure 3.13.

To ensure that the higher energy values are due to heat release through combustion, a non-reactive mixture of methane and nitrogen has also been studied. This mixture contains

the same percentage of methane as the stoichiometric methane/air mixture. For 25.2 mJ of absorbed energy, the shock wave trajectory shows a point blast energy of 22.6 mJ for non-reactive methane/N₂ which is very similar to the result of 22.4 mJ for air. This is also much less than the result of 25.5 mJ for stoichiometric methane/air confirming that an appreciable amount of energy is released through combustion in the focal region prior to emergence of the shock.

Various gas compositions for combustible mixtures are also compared in Table 3.2. For methane/air, lean mixtures are found to have lower blast energies than stoichiometric mixtures but still higher than those of air. Lean mixtures have a lower amount of fuel in a given volume of the gas compared to stoichiometric mixtures. This means they have a lower amount of chemical energy that could be released per unit volume, consistent with the results of this study.

Biogas/air mixtures are also investigated. The point blast energy for biogas/air is higher than air, but lower than its equivalent methane/air mixture for each condition studied. Again, a lower amount of fuel will be in a given volume of gas for biogas than methane due to dilution caused by the CO₂ in the biogas mixture. Additionally, the participation of CO₂ in chemical reactions may decrease the exothermicity of a given volume.

Higher point blast energies have been observed for all of the reactive mixtures used in this study compared with the blast energies for air and non-reactive methane/N₂. This shows that there is appreciable energy release from the mixture near the focal volume at time scales less than 1 μ s which contributes to the ignition process. In the literature, it is typically assumed that in reactive mixtures, the time scale for ignition is on the order of milliseconds and events on microsecond time scales contribute little to the ignition process. However, from extending this type of analysis to combustible mixtures, it is found that this may not be the case. In laser-ignition, the extremely high temperature in the focal volume appear to induce exothermic reactions on sub-microsecond time scales. The heat release and radicals

generated from these exothermic reactions are the initial steps in formation of the flame kernel and therefore critical to the ignition process. In addition, knowing how much energy is released and the strength of the blast wave during this phase of the ignition process will aid in modeling laser ignition. This information from the blast wave analysis may be used towards creating truncated ignition models without going into the details of the plasma physics.

3.3 Internal dynamics of the plasma kernel

After the shock wave dissipates energy away from the focal volume, a high temperature plasma kernel persists in the region. This plasma kernel initiates the combustion process and influences the dynamics of the emerging flame kernel. Understanding this process and quantifying the conditions in this region is an important first step toward developing laser ignition models which accurately represent the physics and thermodynamics of the ignition process. Interferometry is utilized in this work to gain better insight into the thermodynamic conditions and the dynamics of the plasma kernel following optical breakdown.

Single-color interferometry is utilized to perform a qualitative assessment of the plasma kernel density to confirm the results in the previous section. The interferometry technique was described in Section 2.2.2. The phase shift in air, methane/air, and biogas/air at $\phi = 0.6$ are compared at $5 \mu\text{s}$ after breakdown in Figure 3.14. The incident laser energies and absorbed laser energies for all cases are approximately 22 mJ and 9 mJ, respectively. This is a qualitative assessment of the plasma kernel density in these three mixtures because the contributions to phase shift this early after breakdown come from both the electron density and gas density. In each of the images, the shock wave can be seen with a positive phase shift surrounding a region with negative phase shift in the center (the plasma kernel). A stronger negative phase shift, encompassing a larger area, is observed in the methane/air and biogas/air mixtures than in air. In the previous section it was observed that additional energy release in the

combustible mixtures occurs on these microsecond time scales. These images complement those results since additional energy release in the combustible mixtures would lead to a larger plasma kernel with a higher temperature and therefore lower density, as observed here.

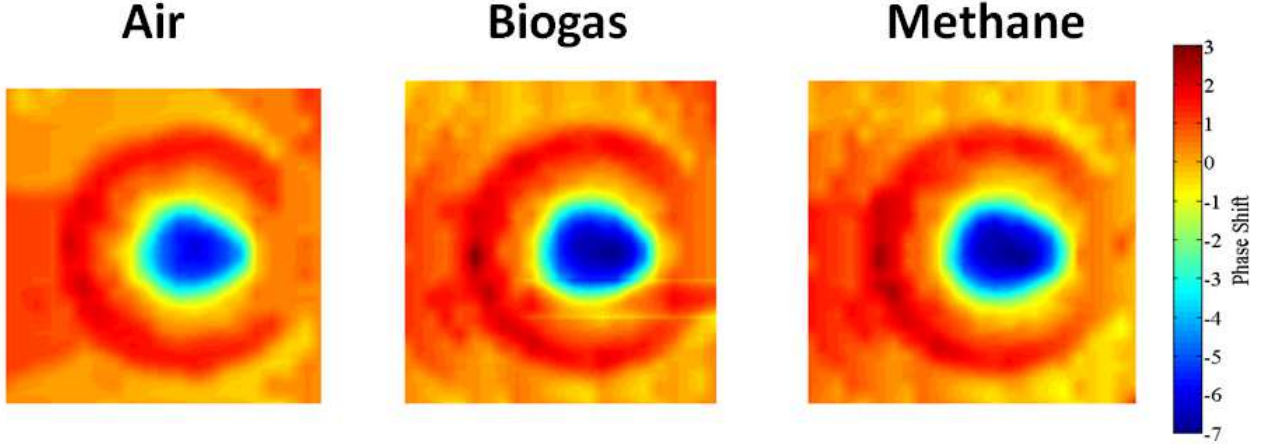


Figure 3.14: Phase shift at $5 \mu\text{s}$ after breakdown measured by one-color interferometer for air, methane, and biogas at $\phi = 0.6$.

In order to quantify the conditions in the plasma kernel, two-color interferometry is utilized for breakdown in air. Interferometric images have been obtained at 0.5 , 1.5 , and $5 \mu\text{s}$ after breakdown for an incident laser pulse energy of 12.3 mJ . Data processing was performed using the method outlined in Section 2.3 in conjunction with Equations 3.20 and 3.21 to yield line-averaged gas density and line-averaged electron density as shown in Figures 3.15 and 3.16 for $1.5 \mu\text{s}$ after the optical breakdown.

$$\Delta n_e L = \frac{1}{r_e} \frac{\Delta\phi_1 \lambda_1 - \Delta\phi_2 \lambda_2}{\lambda_2^2 - \lambda_1^2} \quad (3.20)$$

$$\Delta\rho L = \frac{\rho_0}{2\pi\beta} \frac{\Delta\phi_1 \lambda_2 - \Delta\phi_2 \lambda_1}{\lambda_2/\lambda_1 - \lambda_1/\lambda_2} \quad (3.21)$$

A more informative approach is to look at the evolution of the actual density field. To do this, an Abel transform is performed on a cross section through the center of the plasma kernel. The results at three different delay times after breakdown are shown in Figure 3.17 providing a temporal evolution of the plasma kernel. An extremely low density is observed

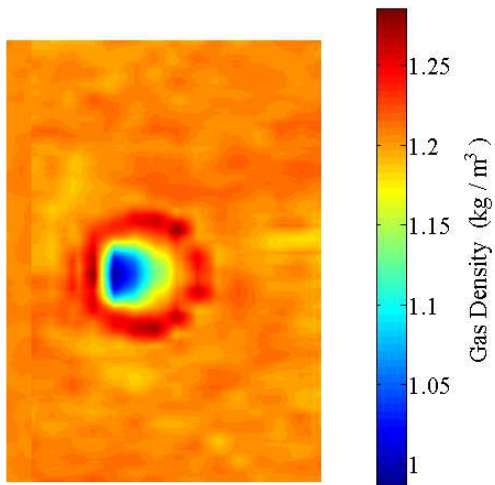


Figure 3.15: Line-averaged gas density measured with two-color interferometer at $1.5 \mu\text{s}$ after breakdown in air for an incident laser pulse energy of 12.3 mJ .

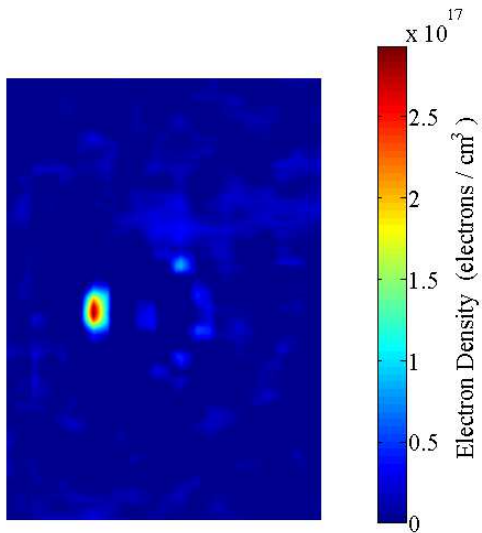


Figure 3.16: Line-averaged electron density measured with two-color interferometer at $1.5 \mu\text{s}$ after breakdown in air for an incident laser pulse energy of 12.3 mJ .

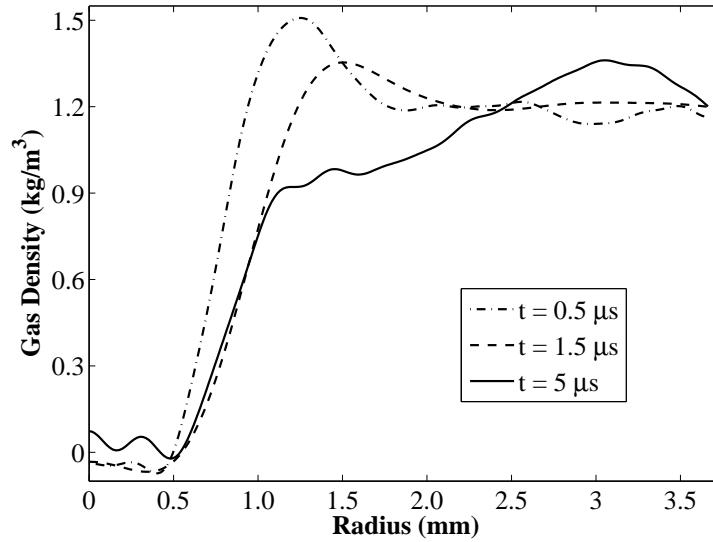


Figure 3.17: Spatial and temporal evolution of the gas density in the laser-induced plasma.

in the center of the plasma kernel which persists up to the last recorded time of 5 μs . The evolution of the shock wave can also be seen, marked by the movement of the density peak to a greater radius with increasing time.

At the center of the plasma, at 0.5 and 1.5 μs , negative densities are calculated. These are non-physical and arise due to errors from two main sources. Firstly, the use of a single camera for this study means the 403 nm and 633 nm interferometric images come from different breakdown events. Although all precautions are taken to ensure shot-to-shot reproducibility, slight differences between the breakdown events can arise as errors in the density calculation. Second, due to the nature of the Fourier-based algorithm used to perform the Abel inversion, small errors in measurement at center of the fringe profile can become amplified during the calculations.

3.4 Comparison of experimental and simulation results

There are many challenges in obtaining accurate, high temporal resolution experimental data during the early stages of laser ignition. Immediately after optical breakdown ($< 1 \mu\text{s}$), broadband bremsstrahlung emissions hinder observational access into the absorbing gas volume. At later times, the shock wave and other processes happen quickly, leading to difficulties in obtaining time-resolved data. To resolve these problems, experiments should be complemented by computational fluid dynamics (CFD) simulations which can probe time-scales otherwise unobtainable through experiments. In this work, the experimental data set previously outlined is compared with simulations of laser-induced breakdown in air. The simulation methodology has been discussed in detail in Section 2.5.

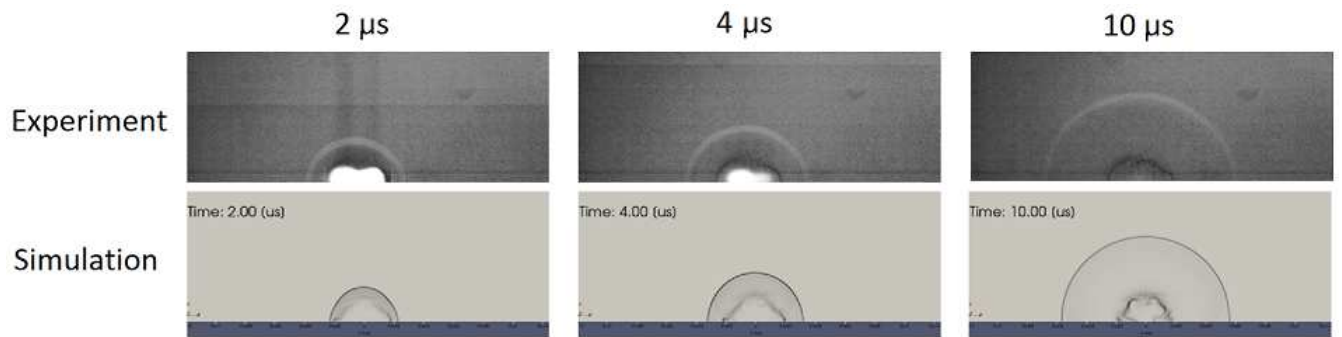


Figure 3.18: Comparison of experimental and simulated density gradient fields in laser-induced shock waves in air at $p = 1 \text{ atm}$, $T = 300 \text{ K}$ and $E_{\text{absorbed}} = 25.2 \text{ mJ}$.

Schlieren images are compared with the density gradient from the simulation for 25.2 mJ of absorbed energy in Figure 3.18. There is generally good agreement in the shock position between the simulation and experimental data. This is highlighted in Figure 3.19, which compares the shock radius for all three energy levels investigated.

The density profiles for a cross section of the plasma kernel are shown in Figure 3.20. The extremely low density observed in the center of the plasma kernel using interferometry is confirmed in the simulation, where the density is found to be as low as 0.015 kg/m^3 . Although errors contributed to slightly negative densities being calculated in the interferometric

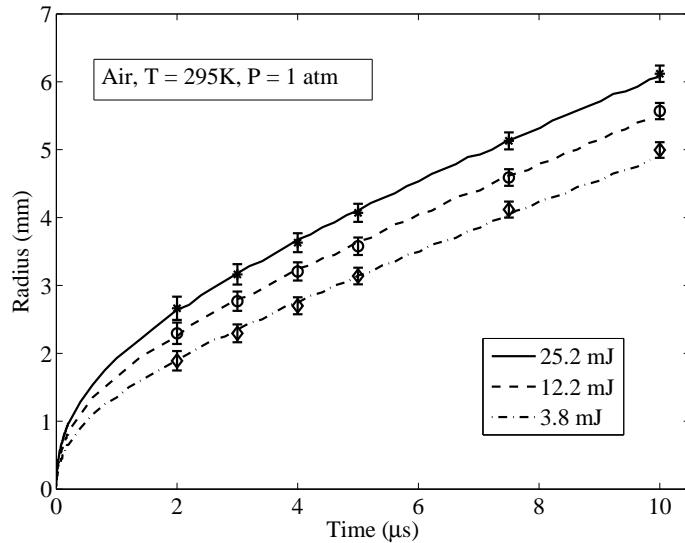
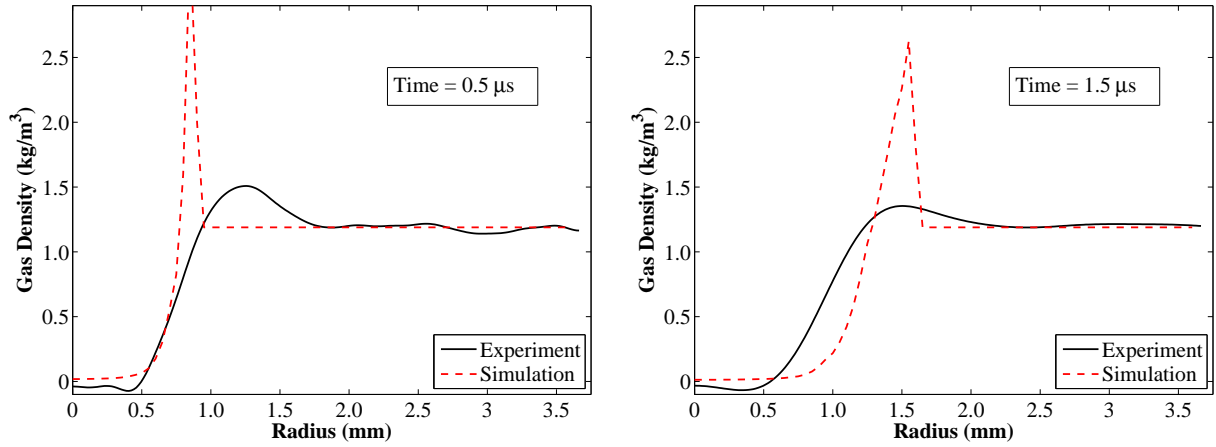


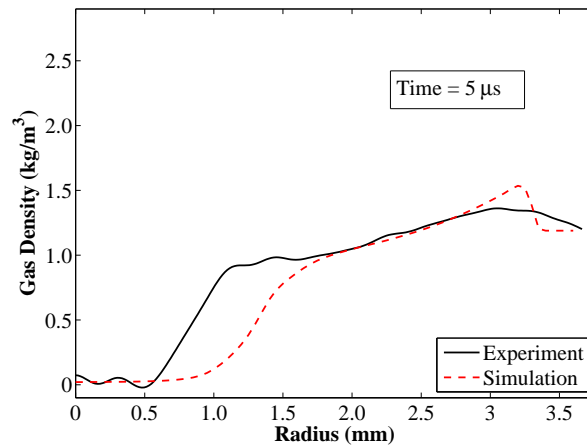
Figure 3.19: Temporal evolution of the shock front in air initially at $p = 1 \text{ atm}$, $T = 300 \text{ K}$.

measurements, a maximum difference of only 6% of the ambient density is observed between the simulation and experimental values at the center of the plasma.

Two main differences in the density profiles are noted. Firstly, the density in the shock wave has a lower peak in the experiment and the profile of the shock wave is broader than the sharp peak in the simulation. This can partially be explained by the spatial resolution of the interferometric images and the exposure time of the camera used to capture the images. The shock wave moves during the exposure time, so the value captured by the interferometer is an average for the shock wave over $1 \mu\text{s}$. The time resolution for the simulation is much greater so that it more accurately captures the position and conditions at the shock front. Secondly, there is a difference in the size of the low density region. At $0.5 \mu\text{s}$ the experiment and simulation are in good agreement with regards to the size of the low density region. At later times, the size grows in the simulation which is not reflected in the experimental results. It has been reported in literature on other laser-induced breakdown simulations that the size of the low density region remains approximately constant [94]. Therefore, this behavior may be due to errors made in the modeling approach for this simulation.



(a) Gas density profile $0.5 \mu\text{s}$ after breakdown. (b) Gas density profile $1.5 \mu\text{s}$ after breakdown.



(c) Gas density profile $5 \mu\text{s}$ after breakdown.

Figure 3.20: Comparison of the spatial and temporal evolution of the gas density in the laser-induced plasma obtained through experiment (solid black line) and simulation (red dashed line).

The simulation results also allow for insight into quantities such as temperature and velocity fields which are not accessible to direct experimental measurement. The development of the velocity field obtained through the simulation is shown in Figure 3.21. After breakdown, the region of low density originating from the focal volume is asymmetrical. It quickly changes to spherical as it expands with the shock wave. As the shock wave detaches from the low density hot core, the core collapses inducing vortices near the center of the shocked region due to the original asymmetry of the laser energy deposition. The formation of these vortices that can be seen at 16 and 20 μs in Figure 3.21. These simulations complement the picture obtained through schlieren imaging and blast wave interpretation.

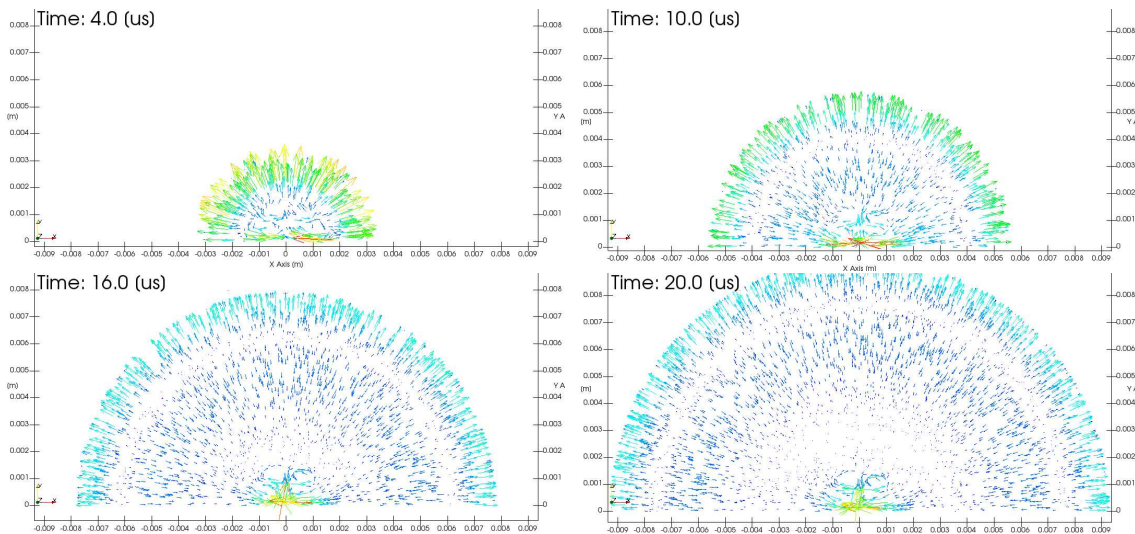


Figure 3.21: Evolution of velocity field, arising from a laser-induced shock wave in air initially at $p = 1 \text{ atm}$, $T = 300 \text{ K}$ with $E_{\text{absorbed}} = 25.2 \text{ mJ}$.

Chapter summary

To summarize, this chapter has focused on the early phase of laser ignition, investigating optical breakdown, laser-induced shock waves, and the internal dynamics of the plasma kernel. The dependence of the optical breakdown threshold on focal length, pressure, and gas composition has been studied. The breakdown threshold in combustible mixtures of light hydrocarbon fuels has been investigated for the first time, revealing that the threshold remains the same as that of air. A universal representation of the focal length and pressure data

was utilized to collapse them onto one curve which facilitated comparison with theoretical collisional cascade and microwave breakdown thresholds. The data was found to agree well with the trend for the theoretical collisional cascade threshold, which is presumed to be the dominant method of breakdown for wavelengths of 532 nm, used in this study.

Laser-induced shock wave trajectories were recorded for air and various combustible mixtures using schlieren imaging. The data was used in conjunction with the blast wave theory to understand how much energy is used to generate the shock wave. The combustible mixtures were found to have higher blast wave energies than air, indicating additional energy release from combustion. It has been presumed in the literature that energy release from combustion is negligible on these time scales, although no experiments in combustible mixtures had been performed to confirm this. The additional energy release was seen for all combustible mixtures studied. Shock wave energies greater than the absorbed laser energy by the gas were observed for some mixtures with high methane content per unit volume of gas.

Interferometry was also utilized to study the dynamics of the plasma kernel after breakdown. Single-color interferometric images were utilized to confirm the findings from the shock wave study. Two-color interferometry was used to quantify the thermodynamic conditions of the gas after breakdown in air. The results from these experimental studies were then compared to results from simulations of laser-induced breakdown, confirming the strength of the blast wave theory to capture the essence of the dynamics of the laser-induced shock waves.

Chapter 4

Fuel effects on laser-induced ignition

This chapter focuses on the effects of fuel type and composition on key aspects of laser-initiated combustion. It first looks at the variation of minimum required laser energies. It then examines the flame kernel formation and ends with the investigation of fuel effects on self-sustained flame propagation.

Two aspects motivate this part of the work: increasing demand for fuel flexibility and a shift toward lean combustion in combustion systems. Among the advantages of lean combustion are increased fuel efficiency and lower maximum combustion temperatures which can impede the formation of some harmful emissions, such as nitrous oxides (NO_X). Although lean combustion is beneficial for overall engine performance, initiation of the combustion process under these conditions is challenging. Understanding the dynamics of the ignition process in the lean combustion regime is a critical area of research in combustion science.

Regarding the demand for fuel flexibility, the idea is to increase energy sustainability. Increasingly considered are biorenewable fuels which can be derived from a number of sources including sugars, plants, and household waste [123]. The composition of some of these fuels, such as biogas and syngas, can vary widely depending on the source and method of production. If the variations in fuel compositions are high enough to affect combustion initiation, this may ultimately lead to adverse affects on engine performance and emissions. It is therefore

necessary to examine the impact of the thermochemical properties of these fuels on ignition dynamics. For laser ignition, previous studies have primarily focused on methane. Relatively few comparative studies of fuel effects on laser ignition have been carried out. In order to successfully implement laser ignition systems, detailed investigations into the role of fuel composition in the ignition process are needed.

In this work, two main classes of fuels are considered; those primarily used in stationary power generation applications, methane and biogas (60% CH₄, 40% CO₂), and those primarily used in transportation systems, iso-octane and E85 (85% ethanol, 15% iso-octane). Some stages of the ignition process are investigated in this chapter. A more detailed treatment of the ignition process is undertaken for methane and biogas.

First, a critical property in the transition from a flame kernel to a self-sustained flame is considered, the minimum ignition energy. The two classes of fuels, iso-octane/E85 and methane/biogas, are both studied in this section. It is shown how different properties of the fuels can be used to explain trends observed in the minimum ignition energy measurements. Next, the laser-induced flame kernel is investigated for methane and biogas. The effect of carbon dioxide in the fuel is considered by comparing flame kernel development for these two fuels. Certain characteristics of flame kernel development are highlighted which may lead to a higher propensity for flame quenching with biogas. Finally, chamber pressure measurements are used to highlight thermochemical effects of fuel/air compositions on the propagation of successfully ignited flames.

4.1 Minimum laser ignition energies

After laser-induced breakdown in a fuel/air mixture, a flame kernel is formed. Successful combustion is critically dependent on the successful transition of the flame kernel to a self-sustained flame. Under certain conditions the flame kernel may fail, resulting in a quenched

flame as shown in Figure 4.1. This leads to misfires in combustion systems, adversely affecting their performance. In order to ensure successful operation of combustion systems utilizing these types of fuels, we must have knowledge of how fuel composition affects the threshold for successful ignition and subsequent propagation of these flames. The thresholds for self-sustained laser-ignited flames are defined by minimum ignition energy, MIE, and minimum pulse energy, MPE.

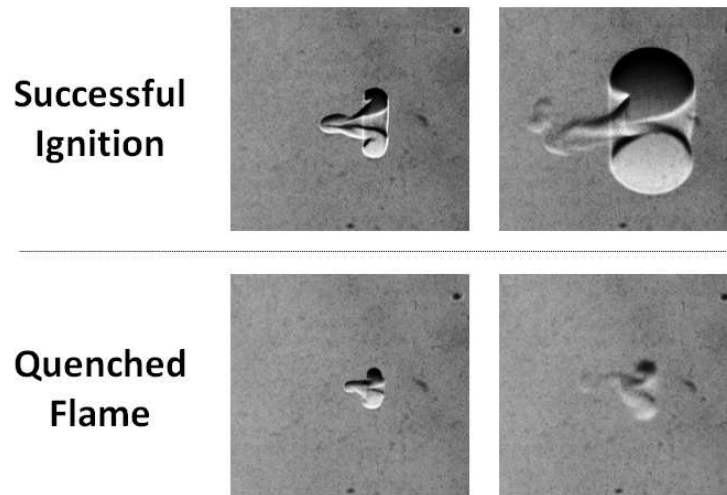


Figure 4.1: Example of successful and quenched flame kernels.

In order to determine ignition thresholds, schlieren imaging is used to identify successful or unsuccessful ignition events. Quenched ignition events, particularly prominent under lean conditions, are counted as failed ignition irrespective of the initial flame emergence. These are also evident in the chamber pressure histories since no appreciable rise in pressure is observed for quenched ignition events. Following the method for breakdown threshold outlined in Section 3.1, MIE and MPE are determined using the logistic regression approach to identify the energy at which the probability of successful ignition is 50%.

Minimum ignition energies can depend upon a number of factors including initial conditions of the fuel/air mixture and properties of the fuel itself. The following subsections address two groups of fuels with quite different reasons for the observed trends in ignition energy. This shows that no one specific fuel property allows one to fully predict the ignition behavior

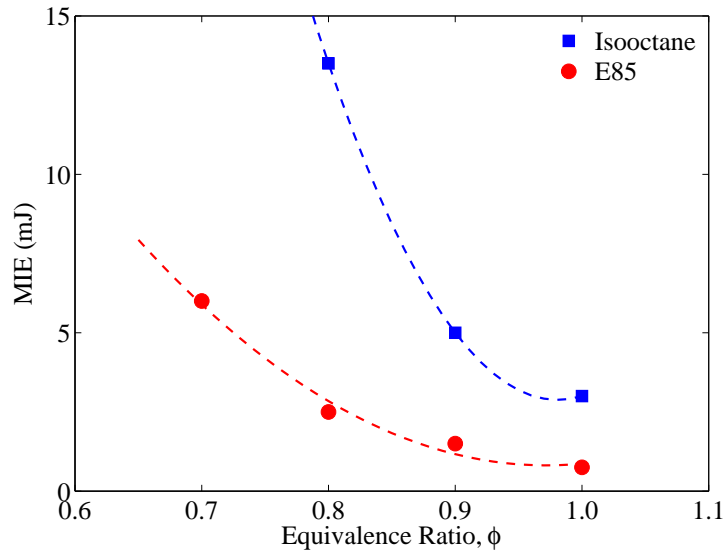


Figure 4.2: Laser ignition of iso-octane and E85, focal length of 15 cm, $p = 1$ atm, and $T = 300$ K.

without prior knowledge gained through experimental investigation. It is therefore important to determine ignition behavior for a wide range of fuels that may be used with future laser ignition systems. In this section, MIE and MPE for iso-octane and E85 will be studied first, followed by methane and biogas.

4.1.1 Iso-octane and ethanol blends

Figures 4.2 and 4.3 show MIE and MPE, respectively, for laser ignited iso-octane and E85 mixtures from lean to stoichiometric conditions. The ignition energies are lowest near stoichiometric conditions and increase as the mixture becomes more fuel-lean. This trend is observed in the ignition energies for all fuels since the adiabatic flame temperature and laminar burning velocity decrease under lean conditions, making it more difficult for a flame to be sustained.

MIE and MPE for E85 are found to be lower than iso-octane under all the conditions studied. This shows that the addition of ethanol greatly reduces the energy required for ignition. The

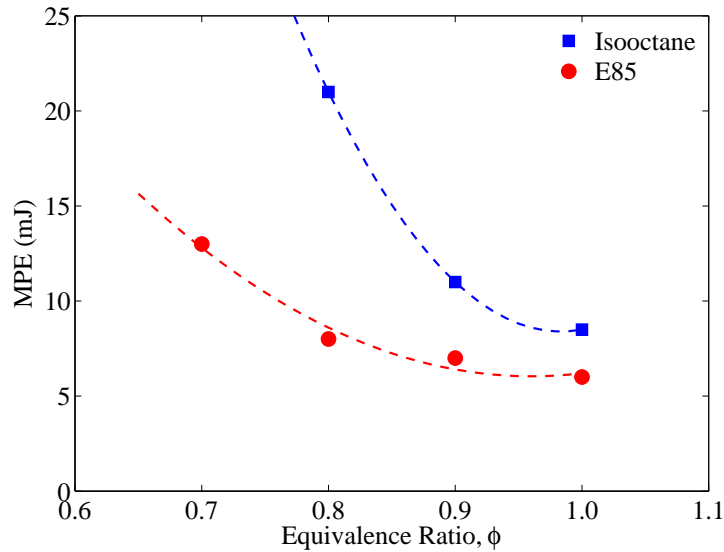


Figure 4.3: Laser ignition of iso-octane and E85, focal length of 15 cm, $p = 1$ atm, and $T = 300$ K.

reduction in MIE and MPE for E85, in comparison with iso-octane, is found to be smaller near stoichiometric conditions. Under lean conditions, the ignition energies for iso-octane increase drastically, limiting the equivalence ratios that can be successfully ignited with practically realizable laser energies. As mentioned previously, there are a number of factors that can contribute to the differences in MIE and MPE measured here.

One factor that can play a role in differences in ignition energy between fuels is the adiabatic flame temperature (AFT). The AFT for ethanol and iso-octane are given in Figure 4.4. The difference between the flame temperatures for these two fuels is within 2%. The difference between iso-octane and the blended fuel E85 would be even less. Therefore, it is not expected that AFT contributes strongly to the difference in ignition energies.

Another fuel property to consider is the laminar burning velocity (LBV). For this parameter, there is an appreciable difference between the two fuels. Figure 4.5 gives the LBV for ethanol and iso-octane. Under stoichiometric conditions, ethanol's LBV is higher than iso-octane's by approximately 20%. It has been noted in the literature that the difference in flame speed

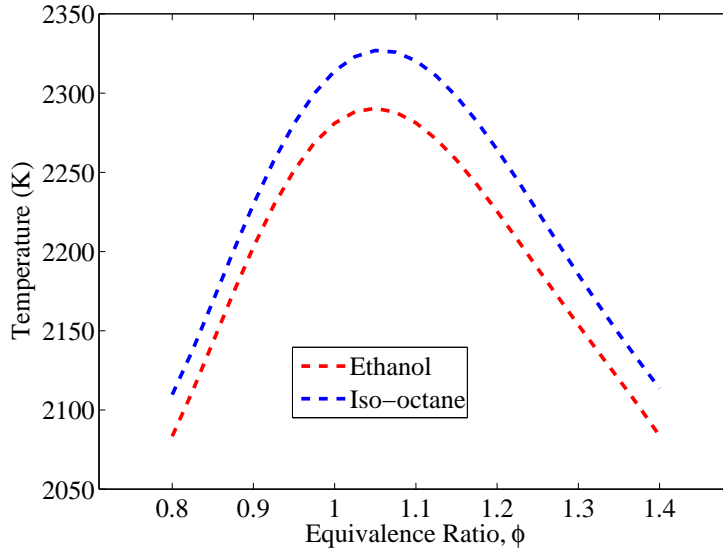


Figure 4.4: Constant pressure adiabatic flame temperature for various equivalence ratios of iso-octane/air and ethanol/air with initial conditions of $p = 1 \text{ atm}$, $T = 300 \text{ K}$.

between these two fuels may be even higher at very early times when the flame kernel is small and highly stretched [124]. This has to do with the different Lewis numbers of the two fuels and the effect smaller Lewis number has on increasing the flame speed for highly stretched flames.

The Lewis number is defined by the ratio of thermal diffusivity to mass diffusivity and it is an important quantity in the study of diffusion flames where there is considerable heat and mass transfer from the burned to the unburned mixture. The equation for Lewis number is [125],

$$Le = \frac{\alpha}{D} = \frac{\lambda}{\rho_u \cdot c_p \cdot D_m} \quad (4.1)$$

Where α is the thermal diffusivity, D is the mass diffusivity, λ is the thermal conductivity, c_p is the specific heat capacity at constant pressure, and D_m is the mixture-averaged diffusion coefficient.

Chen et al. [9] have performed numerical and experimental studies on how Lewis number affects minimum ignition energy. They note that a higher Lewis number correlates with

a larger critical radius of the flame kernel that must be achieved in order for the flame to be sustained. A higher ignition energy is therefore required to obtain the larger critical radius, leading to an increase in MIE for high Lewis number fuels. The Lewis number for stoichiometric ethanol is approximately 1.2 and iso-octane is approximately 1.8, 50% higher than ethanol [124]. This reasoning agrees well with the observed trend for MIE and MPE of iso-octane and E85 measured in this work.

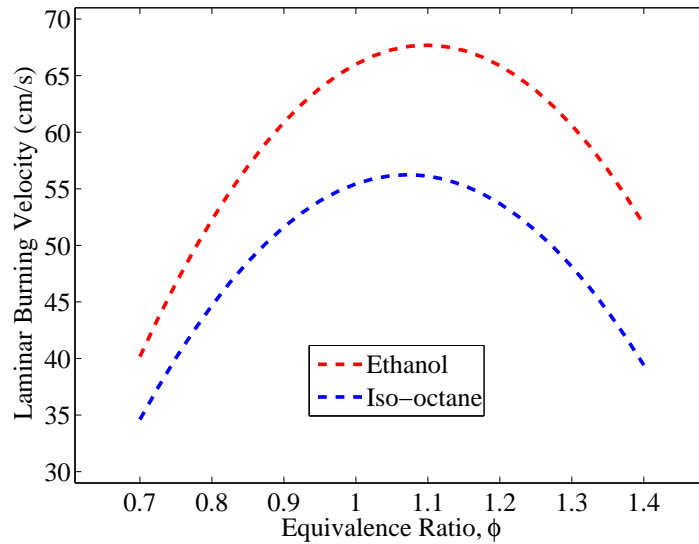


Figure 4.5: Laminar burning velocity for various equivalence ratios of iso-octane/air and ethanol/air with initial conditions of $p = 1 \text{ atm}$, $T = 300 \text{ K}$.

These observations suggest that the early flame kernel development may be much faster for the ethanol blend producing a larger, more robust kernel. The addition of ethanol to gasoline mixtures may be beneficial for combustion engines using laser ignition since it would reduce the energy requirements of the laser, thereby reducing the size and cost of the ignition system. The investigation of ignition energies will now turn to lighter hydrocarbon fuels, namely methane, and fuels which include diluent gas, such as biogas. These are typically used in stationary power generation.

4.1.2 Methane and biogas

Quenching is of particular concern for fuels with low energetic content such as biogas. This makes the determination of minimum ignition energies very important for these types of fuels to ensure successful combustion for given initial conditions of the gas. For biogas, comparison of the ignition energies with methane also provides a convenient method for studying the effects of CO₂ on biogas ignition.

Figure 4.6 shows a comparison of MIEs for methane and biogas at atmospheric conditions for a range of equivalence ratios. For stoichiometric mixtures, methane has a MIE of 1.5 mJ and biogas is 3.25 mJ. At $\phi = 0.6$, the MIE increases to 4.5 mJ for methane and as high as 10.5 mJ for biogas. The MIE for biogas is approximately double the MIE of methane for all equivalence ratios studied. The MPE for methane and biogas under the same conditions are shown in Figure 4.7. Again, the MPE of biogas is higher than that of methane for all equivalence ratios. For stoichiometric mixtures, the MPE is 17.6 mJ for methane and 19 mJ for biogas. At $\phi = 0.6$, these values increase to 20.5 mJ and 24 mJ, respectively. The difference in MPE between the two fuels is roughly the same as the difference in MIE across the range of equivalence ratios. The differences do not exactly match due to the stochastic nature of the laser energy absorption during breakdown.

As previously shown, the breakdown threshold for a given condition is essentially constant for both methane and biogas mixtures. This breakdown threshold for a range of equivalence ratios is shown in Figure 4.7, compared to the minimum pulse energy. Above the breakdown threshold but below the MPE, a flame will quench shortly after ignition. For methane, the breakdown threshold and MPE nearly coincide for equivalence ratio, ϕ , from 0.7 to 1.0. The result is a high probability that breakdown, even near the threshold, will result in successful ignition. There is a non-negligible gap between these values for biogas and it is observed that if the pulse energy is held very close to the breakdown threshold, successful ignition is sporadic

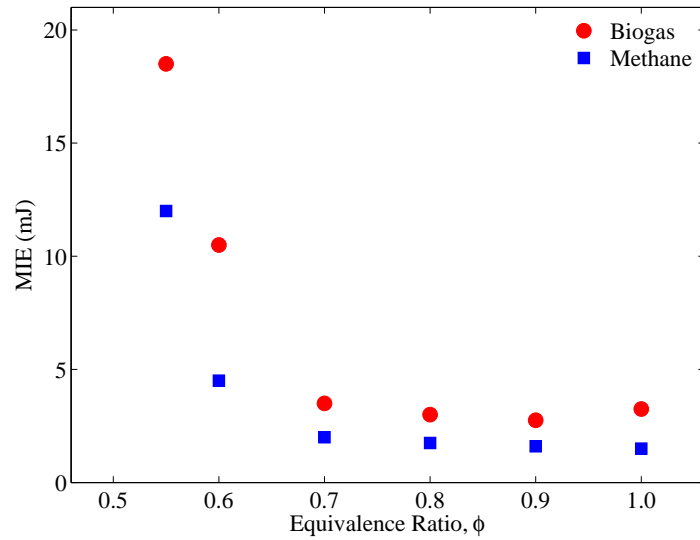


Figure 4.6: Minimum ignition energies at various equivalence ratios of methane/air and biogas/air mixtures, focal length of 15 cm, $p = 1$ atm, and $T = 300$ K. These increase rapidly near the lean limit.

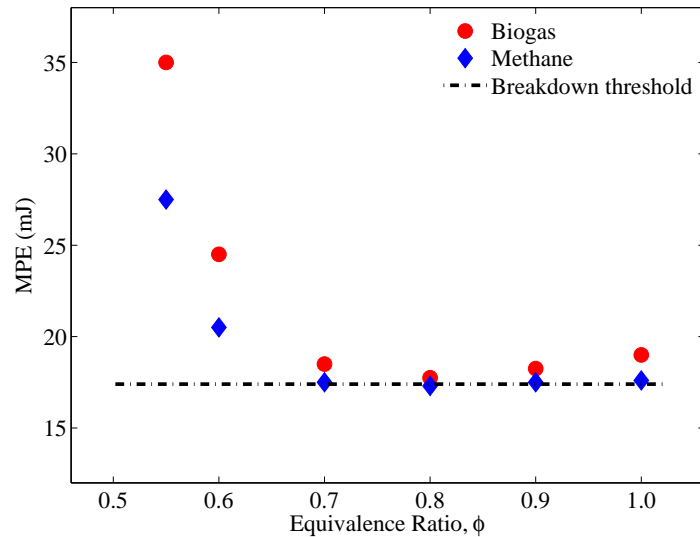


Figure 4.7: Minimum pulse energy for various equivalence ratios of methane/air and biogas/air. Dashed line represents approximate breakdown threshold for methane and biogas mixtures, for a focal length of 15 cm, $p = 1$ atm, and $T = 300$ K.

with most ignition events resulting in quenched flames. Under lean conditions, the MPE for both fuels increases drastically with respect to the breakdown threshold. For equivalence ratios less than $\phi = 0.7$, laser pulse energies close to the breakdown threshold always result in quenched flames. The large difference in ignition energies between methane and biogas for very lean conditions can be explained by the fact that a larger plasma kernel with high enough energy is needed to induce ignition of the surrounding gas through thermal transport and mixing. This higher pulse energy has technical implications. In combustion systems, the larger energy required to ensure a self-sustained flame for biogas would necessitate the use of a more powerful laser than needed for methane which may result in additional cost and size of the laser system.

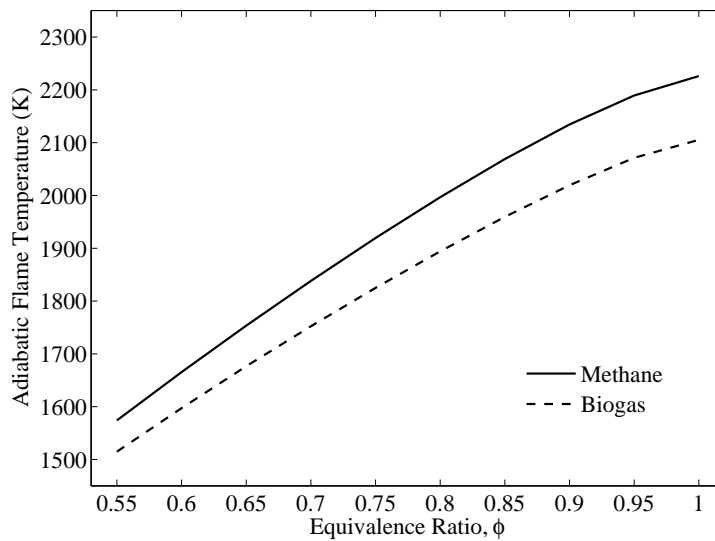


Figure 4.8: Constant pressure adiabatic flame temperature for various equivalence ratios of methane/air and biogas/air with initial conditions of $p = 1$ atm and $T = 300$ K. Values are obtained from chemical equilibrium calculations using the program GASEQ.

In contrast to the iso-octane and E85 mixtures previously studied, the difference in ignition energies between methane and biogas cannot be explained by Lewis number. There is only a 2% difference in the Lewis number between the methane/air and the biogas/air mixtures studied here. Instead, the difference comes from chemical kinetic and dilution effects associated with the addition of CO_2 to the mixture. This has also been observed by other authors in

numerical investigations [126] and experimental laminar burning velocity studies [127]. The chemical effect comes from CO_2 participating in key reactions such as $\text{CO}_2 + \text{H} = \text{CO} + \text{OH}$, competing for H radicals with other chain branching reactions involving H radicals [127]. The thermal dilution effect comes from the higher heat capacity for CO_2 which causes it to act as a heat sink, thereby decreasing the flame temperature. To see this, AFT for methane and biogas mixtures over a range of equivalence ratios is provided in Figure 4.8. The AFTs are obtained from chemical equilibrium calculations using the program GASEQ. As seen in the figure, biogas has a significantly lower flame temperature than methane across the entire range of equivalence ratios. Under stoichiometric conditions the difference in AFT for the two mixtures is 121 K, greater than 5%.

In addition to kinetic effects and lower temperatures, other factors such as flame dynamics may inhibit flame kernel development and lead to a higher propensity for quenching in biogas. Flame kernel dynamics for methane and biogas will be discussed in the following section.

4.2 Flame kernel development

It has been discussed that without sufficient energy input, a flame which has been successfully ignited in the early phase may eventually quench. This section will address some of the properties of flame kernel development that may contribute to quenching in laser-ignited methane and biogas flames. Of particular interest is extending the previous discussion on the role of CO_2 in flame quenching by observing its affect on flame kernel dynamics.

One-color interferometry is utilized to probe the laser-ignited flame kernels at 0.1 ms. At this stage of the ignition process, ionization of the gas is negligible and changes in the refractive index of the gas are solely due to changes in density. Therefore, one-color interferometry can be used since changes in refractive index come from a single source. Additionally, since pressure is approximately constant across the flame front, the changes in refractive index due

to density can be directly correlated to temperature.

To study how CO_2 affects the flame kernel, methane/air is compared with two biogas/air mixtures with varying degrees of CO_2 inclusion: 75% CH_4 /25% CO_2 , and 50% CH_4 /50% CO_2 . Interferometric images of the flame kernels for methane and the two biogas mixtures are shown at the top of Fig 4.9. The bottom of the figure shows the corresponding contour maps for fringe deflection magnitude. Some difference in the structure of the flame kernels can be observed. The volume of the flame gets smaller as the level of CO_2 in the fuel increases, corresponding to a higher surface area to volume ratio. The highest maximum fringe deflection is observed for methane/air and the lowest for the 50% CH_4 /50% CO_2 mixture. Relating this to temperature, this agrees with the higher AFT calculated for methane compared to biogas in the previous section. Additionally, the region of highest intensity grows noticeably smaller as CO_2 content increases. The higher surface area to volume ratio of the CO_2 diluted flames, together with their lower maximum flame temperatures results in lower effective heat transfer to the unburnt mixture. This effectively amounts to a lower thermal diffusion in the weaker flames. As the amount of CO_2 included in the mixture increases, the flame kernel becomes weaker, and therefore the initial energy input required to sustain a flame increases. This is in accordance with the ignition energy results from the previous section.

In addition to the size and temperature of the laser-ignited flame kernels, differences in the dynamics of flame kernel growth have also been observed for methane and biogas. Shown in Figure 4.10 are schlieren images of flame kernel growth up to 0.5 ms after breakdown for methane and biogas at $\phi = 0.9$. Both ignition events are at approximately the same incident energy; 17.7 mJ for methane and 17.5 mJ for biogas. In the first set of schlieren images immediately after breakdown, there is no difference between the two fuels. At 0.1 ms, both flames begin to show typical development for laser-ignited flames. This constitutes a toroidal section around the ignition location and growth of a front lobe which propagates toward the direction of the incident laser beam. It is evident from the first few images that

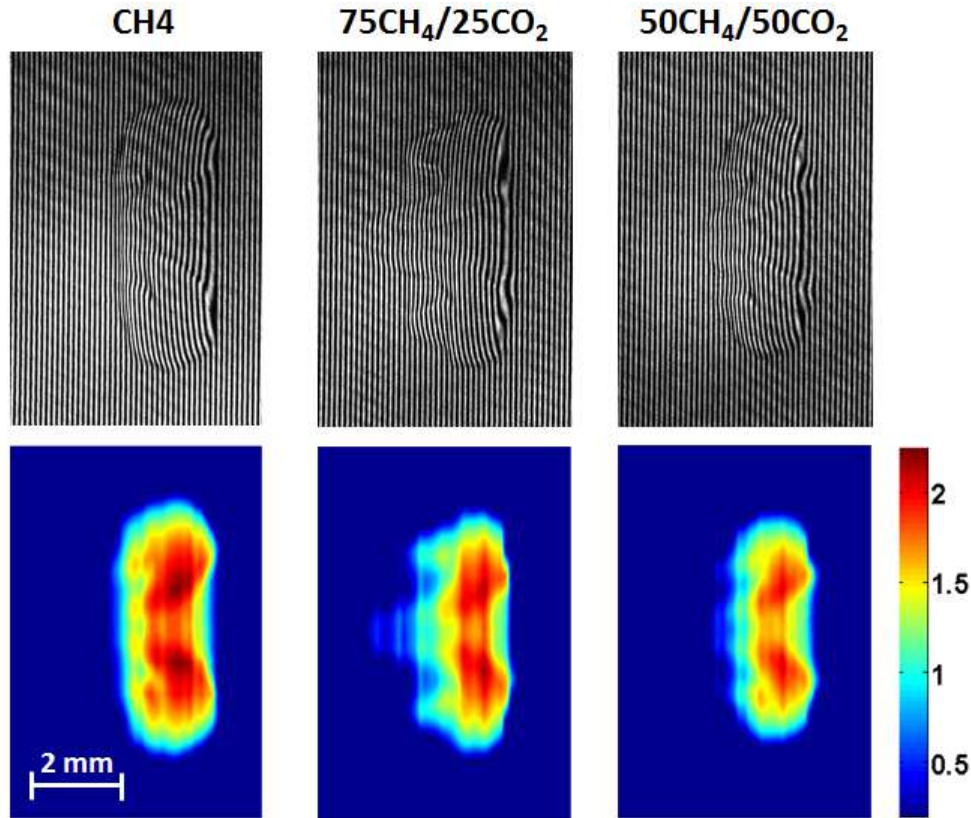


Figure 4.9: (Top) Comparison of flame kernel visualized by interferometry at 0.1 ms for stoichiometric methane, 75% CH_4 /25% CO_2 , and 50% CH_4 /50% CO_2 . (Bottom) Contour maps showing the magnitude of the fringe deflection, where magnitude of 2 corresponds to a displacement of 2 fringe widths.

the front lobe propagates faster for the biogas than for methane. This same phenomenon was recently noted by Almansour et al. [128], although no explanation was offered regarding the effect this may have on the overall ignition behavior. By 0.5 ms, the front lobe of the biogas flame has begun to quench and is more distorted compared with the methane flame kernel. For methane, this type of flame kernel development is typical near stoichiometric conditions. Under lean conditions, the front lobe of methane flame kernels intermittently quench. The front lobe is quenched for biogas at all equivalence ratios, however, leaving only the main toroidal section of the flame.

To investigate the quenching of the front lobe, the propagation of the front lobe of the flame is compared with the main toroidal section for methane and biogas. This is performed by

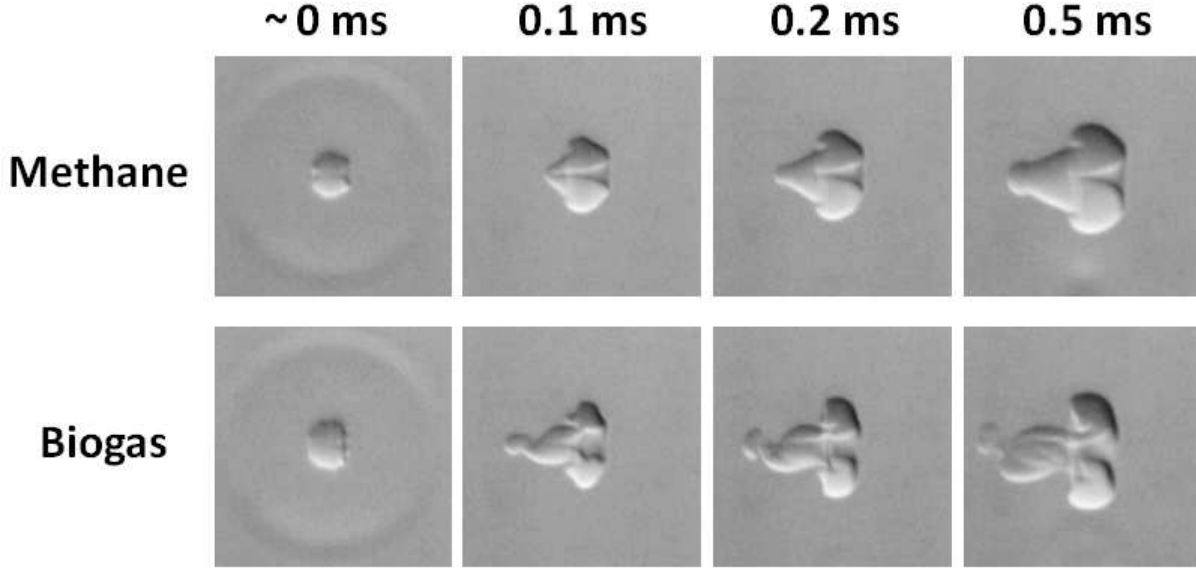


Figure 4.10: Laser ignited flame kernel development for methane and biogas at $\phi = 0.9$, $p = 1$ atm, and $T = 300$ K. The incident laser energies for these ignition events were 17.7 mJ for methane and 17.5 mJ for biogas.

determining the difference between the radius of the front lobe and toroidal section and normalizing this difference by the radius of the toroidal section, shown in Equation 4.2. In this equation, r_{FL} is the radius of the front lobe and r_{TS} is the radius of the toroidal section. The result is averaged over five ignition events for each fuel and is plotted in Figure 4.11.

$$\frac{r_{FL} - r_{TS}}{r_{TS}} \quad (4.2)$$

The front lobe of both fuel/air mixtures accelerates rapidly compared to the toroidal section for the first 0.2 ms. After that, both front lobe and toroidal sections begin to propagate at approximately the same speed. Within the first 0.2 ms, it is clear that the biogas front lobe propagates much faster with respect to the main body of the flame than methane. The very rapid acceleration of the highly curved front lobe of the biogas flame creates a high rate of stretch. This weakens the biogas flame, causing localized quenching to occur. As the front lobe distorts and begins to quench, the cool gas surrounding the flame is entrained, promoting heat loss in the main toroidal section. This mechanism hinders flame kernel development for

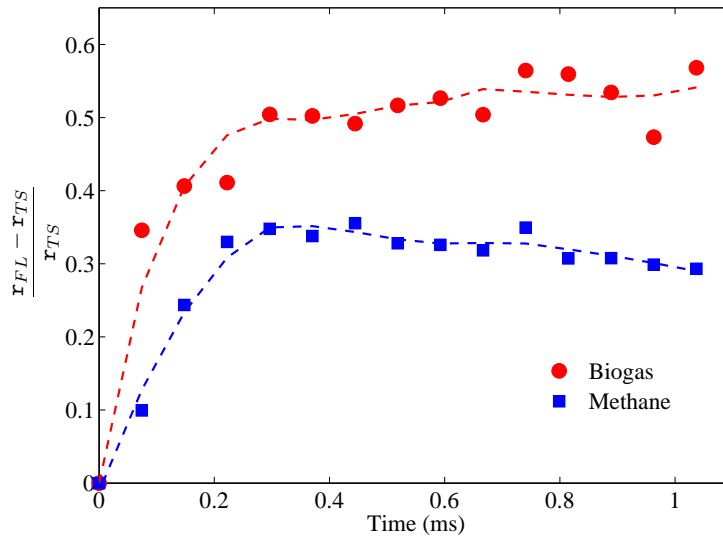


Figure 4.11: Front lobe radius, r_{FL} , compared to radius of toroidal section, r_{TS} . Symbols represent the average of five ignition events and are fitted with a trendline.

biogas compared with methane, particularly near stoichiometric conditions.

This section has furthered the discussion on some of the parameters that may contribute to flame quenching and it has highlighted key differences between methane and biogas flame kernels. The next step in the ignition process is the transition to a self-sustained flame. If a sufficient amount of energy is introduced into a fuel/air mixture to ensure that the ignition process is successful, it is important to know the behavior of the resulting combustion wave.

4.3 Propagation of self-sustained flame

Combustion system performance depends strongly on the behavior of the flame after successful ignition. If the flame propagation from the ignition point is too slow, then this may result in incomplete combustion. It is therefore important to understand the role that fuel composition plays in flame behavior in order to avoid incomplete combustion. In this section, comparison of successful ignition events is achieved through schlieren visualization and measurements of

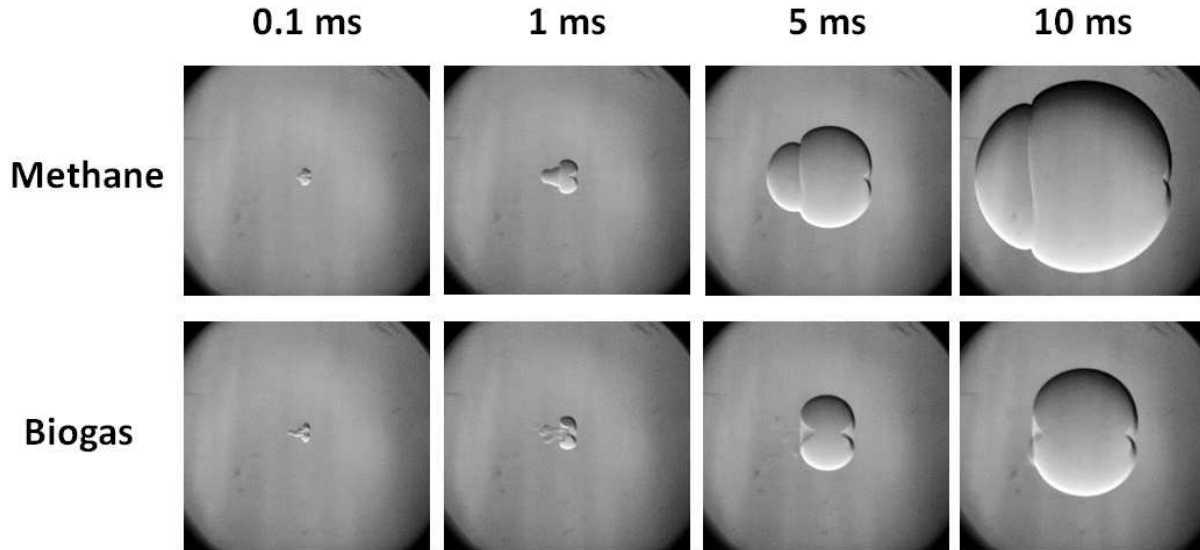


Figure 4.12: Evolution of laser ignited flames of methane and biogas at $\phi = 0.9$, $p = 1 \text{ atm}$, and $T = 300 \text{ K}$. The incident laser energies for these ignition events are 17.72 mJ for methane and 17.51 mJ for biogas.

dynamic pressure inside the combustion chamber.

The evolution of successfully ignited methane and biogas flames at an equivalence ratio of 0.9 is shown in Figure 4.12. As previously noted, the flame kernel development in the first two frames of the figure are quite different. The front lobe of the biogas flame quenches, leaving only the toroidal section. By 5 ms, the flame kernels have transitioned to well established flames. At this point, the biogas flame is substantially smaller than the methane one. After this point, further propagation is controlled by chemical reactions in the flame. Between 5 and 10 ms, the lower laminar burning velocity of the biogas flame is evident as the methane flame expands much more rapidly.

The dynamic pressure inside the chamber during combustion for methane and biogas ignition is given in Figure 4.13. For both fuels, the peak pressures are lower for lean mixtures, partly related to the lower adiabatic flame temperatures and the longer flame time scales which promote heat loss to the walls. Also, the time to reach the peak pressure is extended for lean mixtures as the burning velocity decreases. At each equivalence ratio, biogas has both lower

peak pressures and takes a longer time to reach the peak pressure than methane. Combined with flame temperatures, thermochemical effects can be used to understand these propagation and pressure levels.

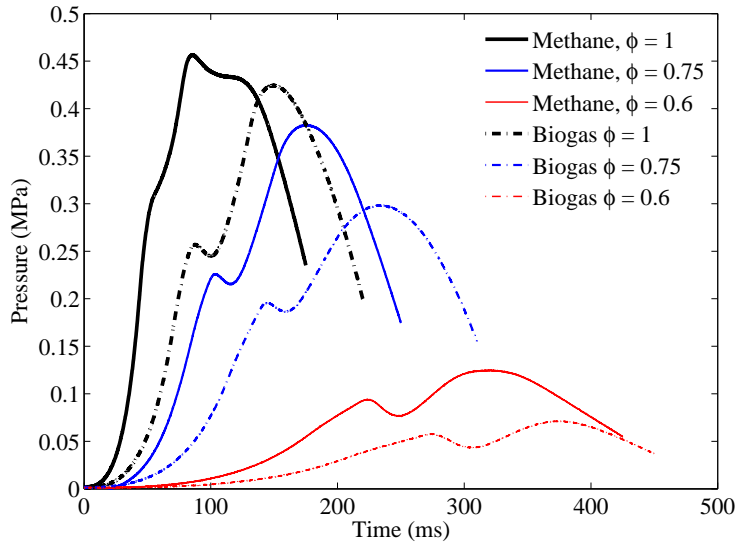


Figure 4.13: Chamber dynamic pressure histories for single ignition events of methane and biogas mixtures at various equivalence ratios, $p = 1 \text{ atm}$, and $T = 300 \text{ K}$.

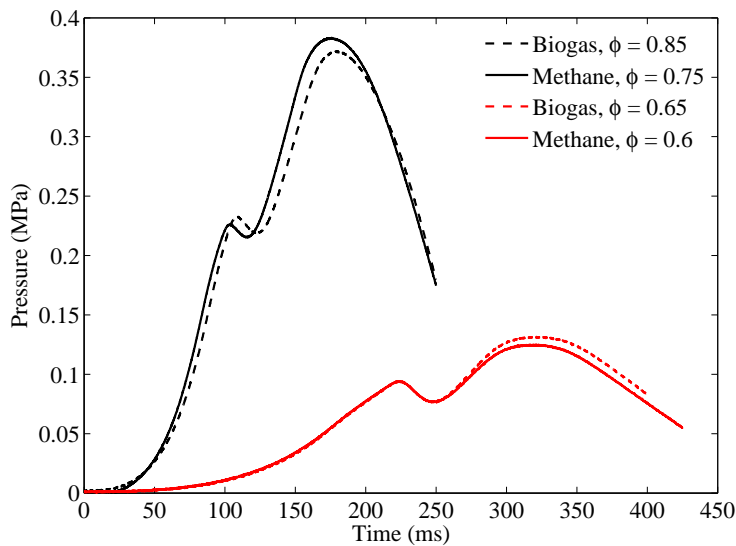


Figure 4.14: Chamber dynamic pressure histories for methane and biogas mixtures with the same mass fraction of methane, $p = 1 \text{ atm}$, and $T = 300 \text{ K}$. Biogas at $\phi = 0.85$ corresponds with methane at $\phi = 0.75$ and biogas at $\phi = 0.65$ corresponds with methane at $\phi = 0.6$

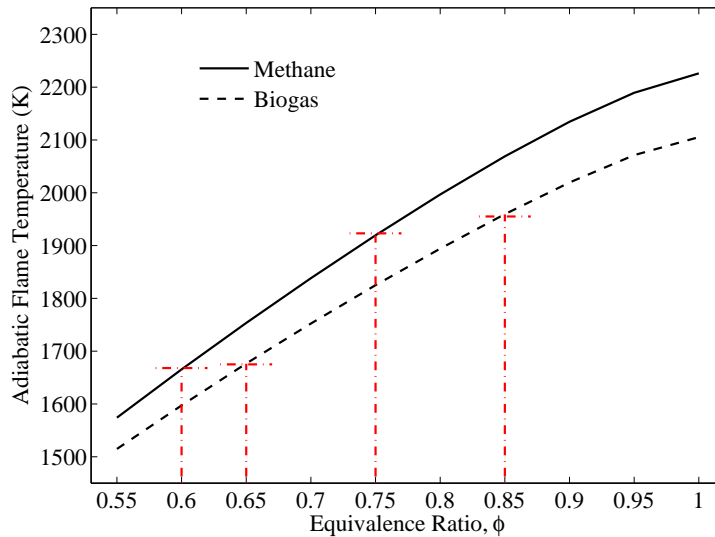


Figure 4.15: Constant pressure adiabatic flame temperature for various equivalence ratios of methane/air and biogas/air with initial conditions of $p = 1$ atm, $T = 300$ K. Red lines identify methane and biogas fuel/air mixtures with the same mass fraction of methane.

Figure 4.14 shows the pressure trace for methane and biogas at different equivalence ratios for which the mass fraction of methane is the same in both pure methane fuel and biogas. The pressure traces from biogas at $\phi = 0.85$ and methane at $\phi = 0.75$ are nearly identical. The same overlap is seen for biogas at $\phi = 0.65$ and methane at $\phi = 0.6$. As shown in Figure 4.15, these mixtures have very similar adiabatic flame temperatures. Hence, when the methane mass fraction is the same, there is comparable heat release due to combustion and similar flame dynamics will result for the two different mixtures. As stated earlier, differences observed in ignition and flame dynamics between methane and biogas at the same equivalence ratio may therefore be explained by the thermal dilution and chemical effects of CO_2 and not transport properties. For the same mass fraction of methane, it appears this does not play a large role and the similarity in diffusivity between CO_2 and the fuel/air species leads to similar flame dynamics.

Chapter summary

This chapter has investigated several phases of the combustion process, from flame kernel

development to the behavior of successfully ignited flames, studying the impact that thermochemical properties of fuels have on combustion dynamics. Minimum ignition energies were compared for iso-octane and E85, as well as methane and biogas. A detailed analysis of the combustion process for methane and biogas was then performed.

E85 was found to have significantly lower MIE and MPE than iso-octane, allowing for leaner mixtures to be successfully ignited using the same energy level. This result can be explained by the lower Lewis number for ethanol, resulting in a higher initial burning velocity and quickly growing flame kernel. The MIE and MPE for biogas was found to be higher than that of methane. For methane and biogas, the Lewis numbers are very similar. The difference in ignition energies is instead due to the chemical kinetic and thermal dilution effect that CO_2 has on the ignition process.

Flame kernel development has also been compared based on schlieren visualizations. Biogas mixtures showed significantly faster flame propagation of the front lobe. The high rate of stretch leads to distortion and quenching of the front lobe for biogas, promoting heat loss from the toroidal section of the flame. These factors, in addition to lower flame temperatures as indicated in interferometric images, result in a much smaller volume and weaker flame kernel for biogas compared with methane at the same equivalence ratio.

Once self-sustained flames are successfully established, the flame behavior is controlled by the chemical composition of the fuel/air mixtures. Methane resulted in faster propagating flames and higher peak pressures within the chamber than biogas at the same equivalence ratio. Methane and biogas mixtures at different equivalence ratios, but the same mass fraction of methane, have similar flame propagation behavior. For these mixtures, the thermal and chemical effects of CO_2 are negligible, resulting in nearly identical adiabatic flame temperatures. The similarity in transport properties between the fuel/air mixture and CO_2 lead to comparable flame dynamics.

Chapter 5

Laser and spark ignition comparison

This chapter contrasts laser ignition with spark ignition, which is the dominant approach used to initiate combustion in combustion systems. The early plasma kernel is examined, followed by the later phase of self-sustained flame propagation. Fuel effects are included in this second part, the idea is to see whether the flames realized have any memory of the ignition process.

The motivation for this part of the work is that laser ignition is being considered as a possible replacement for spark plug ignition. In engine testing, it has been observed that laser ignition results in a shorter combustion duration, allowing for extension of the lean operability limit in SI engines. Comparison of spark and laser ignition has mainly focused on engine testing and relatively few fundamental comparative studies exist. Further insight into the performance benefits of laser ignition seen in engine testing may come through using optical diagnostics to contrast the two ignition technologies.

The fuel and equivalence ratio effects that have been examined in the previous chapters for laser ignition will be contrasted here with spark ignition for iso-octane and E85, as well as methane and biogas.

5.1 Plasma kernel

In order to provide context for the combustion studies using spark and laser ignition systems, sparks in atmospheric air are first compared. Interferometry is used to measure the geometry of the sparks as well as to compare their relative strengths.

Interferometric images of the spark produced by the laser and spark plug are shown along the top of Figure 5.1. The first image is taken within $1 \mu\text{s}$ after laser-induced breakdown. The second image is taken within $1 \mu\text{s}$ after the solid state relay opens, inducing a high voltage in the secondary circuit of the ignition coil and causing breakdown. The exposure time for the camera in these images is set for $5 \mu\text{s}$, smoothing out the shock wave from laser-induced breakdown. Fringe shifts are observed over areas larger than the localized plasma production due to heating of the gas surrounding the spark. This total area of influence is measured for each system. Laser breakdown produces a sphere of heated gas with a diameter of approximately 2.5 mm. The initial geometry produced by the spark plug is a rectangle that is approximately 0.6 mm by 1 mm. However, the width of the spark increases from 0.6 mm to 2 mm over the next $100 \mu\text{s}$ as the gas is continually heated.

The intensity of these sparks are compared by measuring the magnitude of the fringe deflection. Contour maps with the color corresponding to the magnitude of the fringe deflection are shown at the bottom of Figure 5.1. The laser spark shows a much higher intensity than the initial electric breakdown produced by the spark plug. A deflection of 1 fringe width is measured at the center of the laser spark while the spark plug produced a deflection of only 0.3 fringe widths. After $100 \mu\text{s}$, towards the end of the electric discharge from the spark plug, the deflection increases to 1 fringe width. This matches the intensity of the laser spark, although on a much longer timescale than the nanosecond energy deposition from the laser. Additionally, the region of hot gas produced by the laser spark is much larger than that produced by the spark plug.

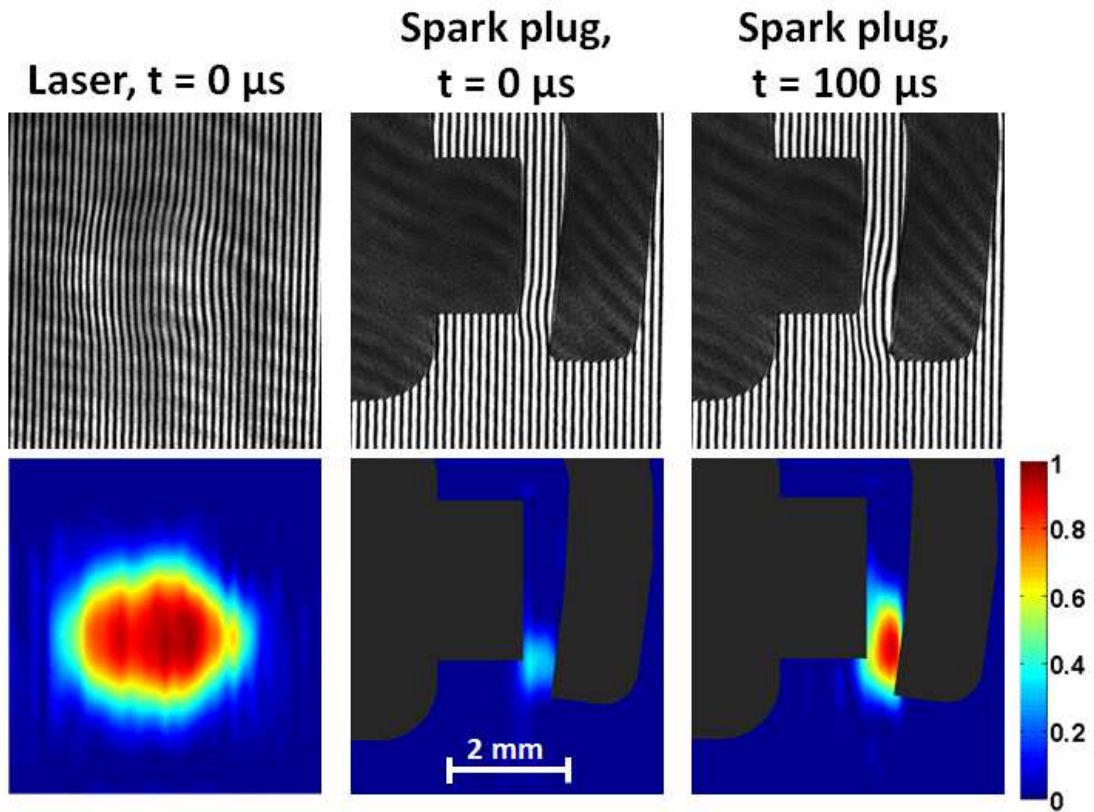


Figure 5.1: (Top) Interferometer fringe patterns for laser-induced breakdown and the initial and final stages of spark-discharge in air. (Bottom) Contour maps showing the magnitude of the fringe deflection, where magnitude of 1 corresponds to a displacement of 1 fringe width.

Many factors can influence the geometry of these sparks. For laser ignition, the spark volume is highly dependent on the focal length of the lens used to focus the laser beam. For spark plugs, the spark gap, electrode geometry, and number of ground electrodes can all have a significant influence on the spark size and development of a flame kernel. One parameter that remains consistent is the difference in energy deposition time scales between the two technologies. Lasers used for ignition typically have pulse widths on the order of nanoseconds while spark plugs, whether capacitive or inductive discharge, have an arc phase that lasts for micro- to millisecond time scales [129]. The difference in energy deposition timescales likely plays an important role in their relative ignition capabilities.

5.2 Ignition of iso-octane and ethanol blends

In this section, laser and spark ignition are compared for iso-octane and E85 under the same conditions. Schlieren images of laser and spark ignited stoichiometric and lean E85/air mixtures are shown in Figure 5.2. These images show the transition from a flame kernel at 0.1 ms to a self-sustained flame at 40 ms. As would be expected, the lean mixtures ($\phi = 0.8$) propagate slower than the laser and spark ignited stoichiometric mixtures. Under stoichiometric conditions, the laser and spark plug produce similar flames. However, under lean conditions, a large difference can be seen between the evolution of the laser and spark ignited flames. In order to quantify the differences between the evolution of these flame kernels, the distance between the lower edge of the flame front and a reference point of ignition, as shown in Figure 5.3, is determined using an in-house code for edge detection and distance measurement. This process, which allows for quantification of the temporal evolution of the laser and spark ignited flame sizes, has been outlined in Section 2.3.

Figure 5.4 shows the flame radius for laser and spark ignition of stoichiometric and lean mixtures of iso-octane. The profiles show a sharp increase in flame distance immediately after

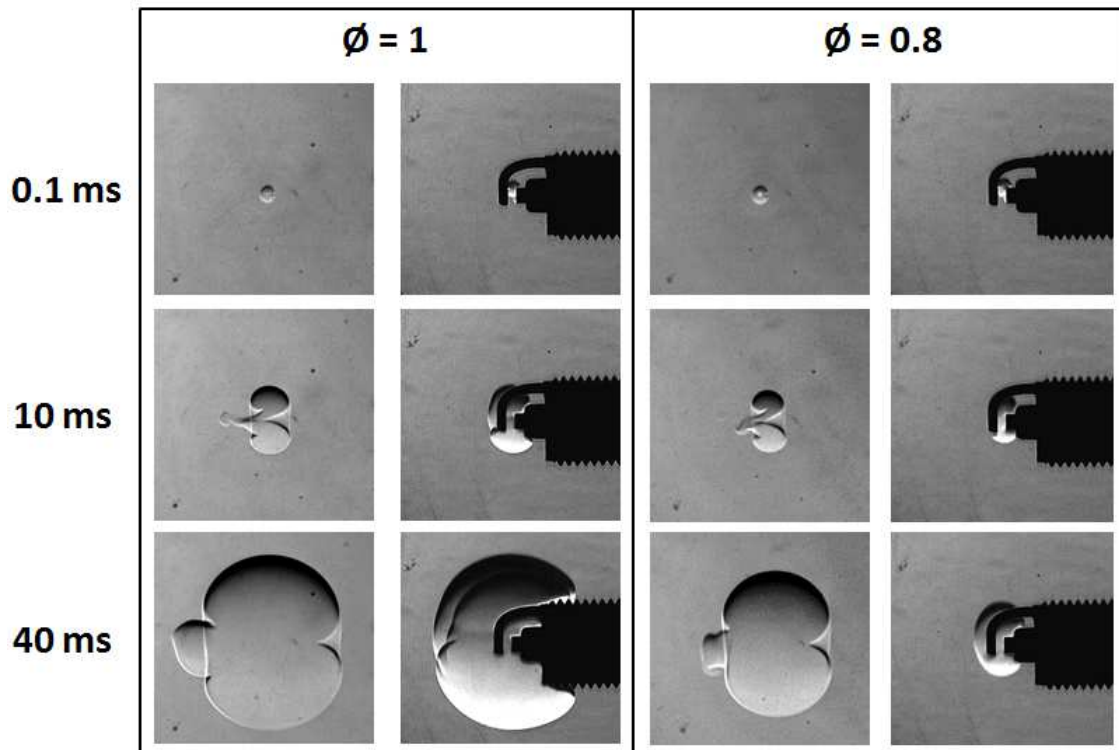


Figure 5.2: Schlieren images of laser and spark ignited flames of E85/air mixtures, $T = 300$ K, $p = 1$ atm..

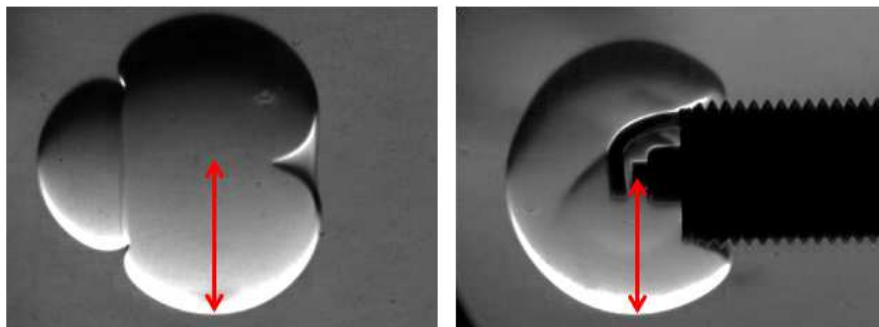


Figure 5.3: Quantifying the temporal evolution of the early flame kernels using the lower edge and the spark center.

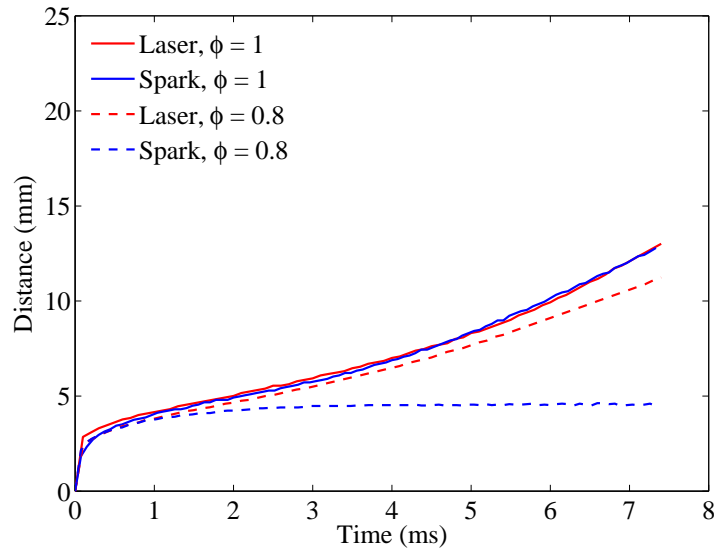


Figure 5.4: Comparison of iso-octane flame propagation for spark (blue) and laser (red) ignited flames at stoichiometric (solid lines) and lean (dashed lines) equivalence ratios, $T = 300\text{ K}$, $p = 1\text{ atm}$.

energy deposition as a flame kernel is formed until around 0.25 ms when the transition to a self-sustained flame begins. For stoichiometric mixtures, the laser and spark ignited flames develop nearly identically. After 0.25 ms, each flame begins to propagate at a characteristic rate that is controlled by the laminar burning velocity of the fuel/air mixture. For lean conditions, the laser ignited flame shows similar behavior by quickly transitioning to a self-sustained flame. The lean flame propagates at a slightly slower speed than the stoichiometric mixture, as would be expected. The spark ignited lean mixture, after development of the flame kernel, shows a long induction period. For the slower propagating iso-octane flame, this leads to quenching since heat loss from the flame overcomes heat generation through chemical reactions, stalling the flame front. This induction period occurs when the size of the flame kernel is approximately the same order of magnitude as the spark plug ground electrode surrounding the ignition area. For lean fuel/air mixtures, lower flame speeds allow more time for heat transfer to occur between the developing flame and the surrounding spark plug electrodes.

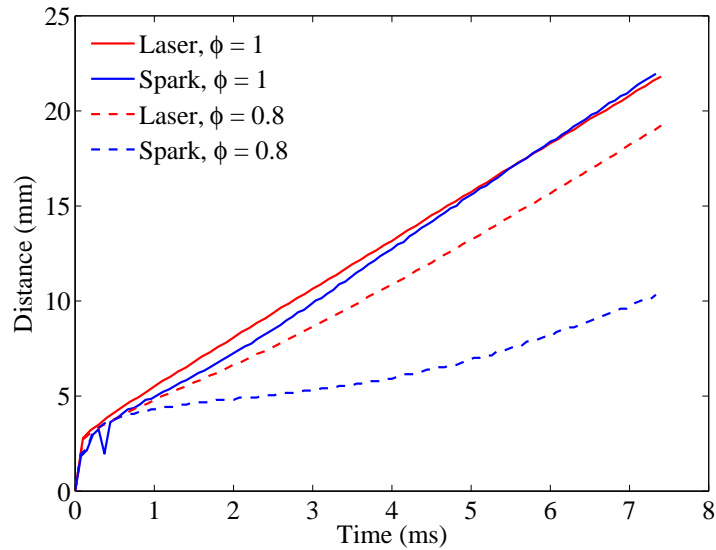


Figure 5.5: Comparison of E85 flame propagation for spark (blue) and laser (red) ignited flames at stoichiometric (solid lines) and lean (dashed lines) equivalence ratios, $T = 300\text{ K}$, $p = 1\text{ atm}$.

The same plot of flame front against time is shown in Figure 5.5 for E85. The features described for the laser and spark ignited flames are similar except for the lean flame initiated with a spark. Its induction period is long but it eventually transitions to a self-sustained flame in contrast to the quenched iso-octane flame.

These results provide further insight into why laser ignition has been observed to have superior performance in gasoline engines, particularly under lean conditions. Laser ignition exhibits a quick transition from flame kernel to self-sustained flame while for spark ignition, a long induction period for the flame kernel is observed as the surrounding electrodes hinder this transition.

5.3 Ignition of methane and biogas

The same approach used in the previous section is now applied to the study of methane and biogas. Stoichiometric and lean ($\phi = 0.8$) mixtures of methane are ignited using a laser and a

spark plug. Figure 5.6 shows Schlieren images of the ignition process at various time instances. It is observed that for each ignition method at early times up to 0.1 ms, the flame kernel growth is fairly consistent for the lean and stoichiometric mixture. At 1 ms, the laser ignited flames of the lean and stoichiometric mixtures are still nearly identical. In contrast to the iso-octane and E85 mixtures previously studied, the laser ignited flame kernels are also much larger than the spark ignited ones, even under stoichiometric conditions. Additionally, the lean spark ignited flame appears to be developing at a slower rate than the stoichiometric one. This disparity can lead to greater heat loss to the electrode by the lean flame. This difference between the lean and stoichiometric spark-ignited flame is more pronounced at 4 ms. The slower development rate of the lean mixture is also evident in the laser ignited flames.

In combustion systems, pressure histories are the most practical diagnostics of the combustion process. The chamber pressure history is shown in Figure 5.7. Noticeable pressure rise for the stoichiometric flames emerges at about 10 ms, after a reasonable volume of the test mixture has been burnt. In the case of the lean mixture, noticeable pressure rise is observed at a later time (about 25 ms). Matters of ignition failure are to be decided based on the dissipation patterns as revealed in Figure 5.6. Once successful ignition has been realized, the pressure histories in Figure 5.7 show that both the laser-induced and spark ignited flames exhibit nearly identical pressure rise behavior. Differences between the pressure histories of the two ignition methods at the same equivalence ratio are less than 2%. Such small deviations are likely a result of test-to-test variations in composition and initial conditions, not a product of the ignition method. Over long time scales, as shown in the pressure history, thermochemical properties of the mixtures dominate over the early ignition differences and the shape of the pressure curve is due to intrinsic properties of the mixture, such as its burning velocity.

Returning to the crucial early phase of the ignition process, the temporal evolution of the laser and spark ignited flame sizes measured from the schlieren images are shown in Figure 5.8. In contrast to the pressure traces which capture much later flame times, a clear distinction

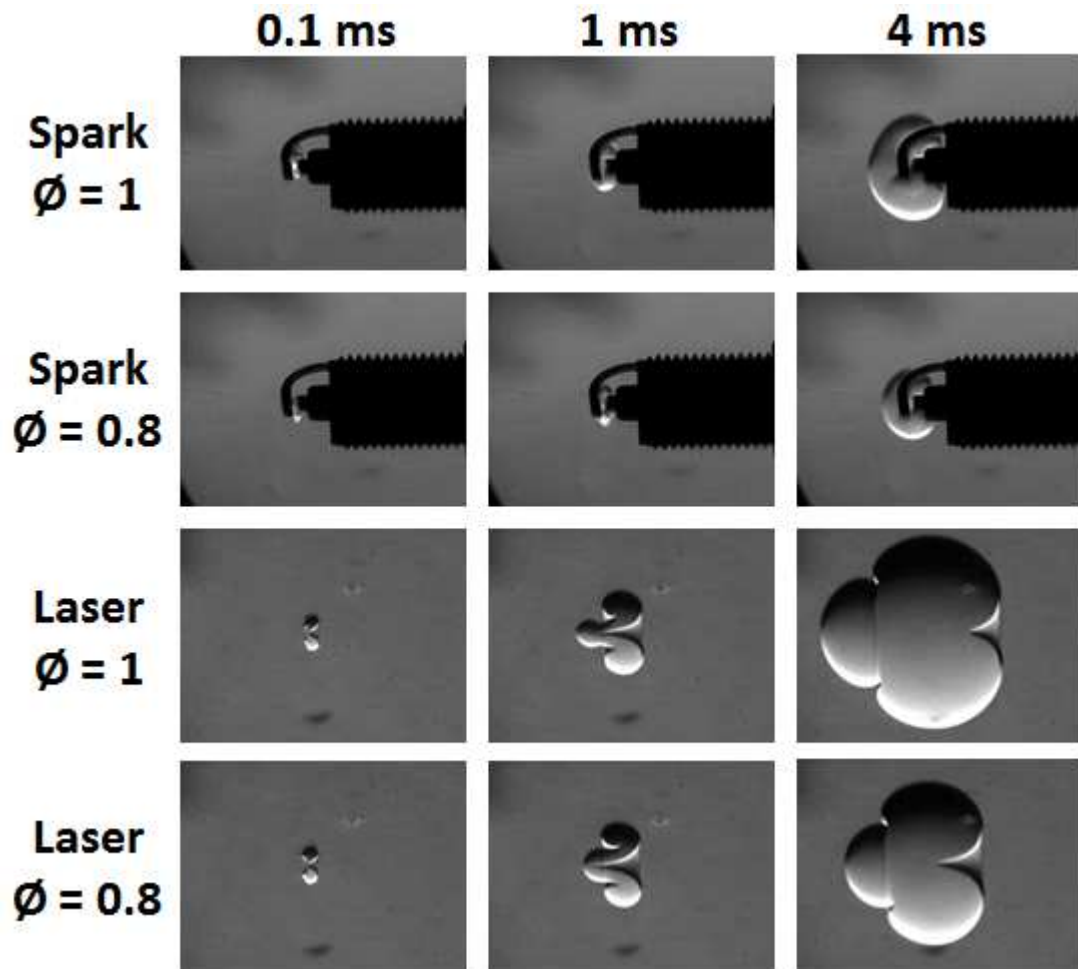


Figure 5.6: Evolution of the early flame kernels in laser-induced and spark-ignited methane flames under stoichiometric and lean conditions. At 4 ms, the lean flames clearly propagate slower than the stoichiometric flames for each method, with the spark-ignited flames clearly lagging the laser-induced flames.

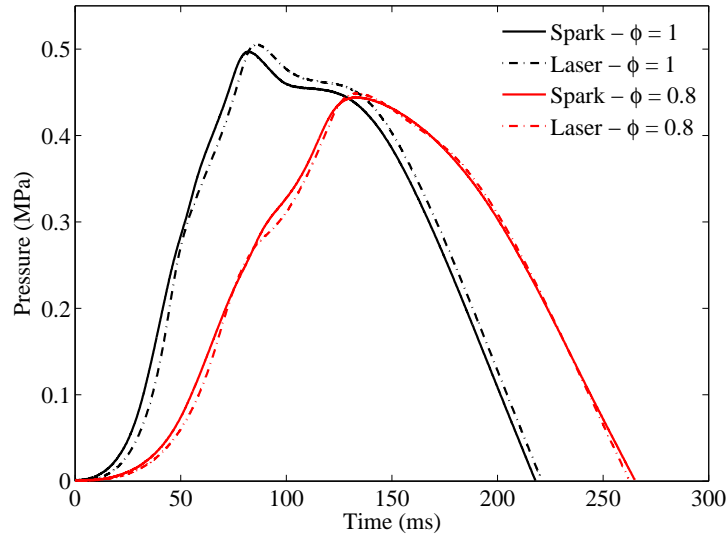


Figure 5.7: Pressure profiles during ignition of stoichiometric and lean mixtures of methane by laser and spark-discharge. At the same equivalence ratio, similar pressure evolution is observed.

can be made between the laser and spark ignited flames during the early phase. Both laser ignited flames of the stoichiometric and lean mixtures are nearly identical up to about 1.5 ms. Beyond this time, the flames begin to propagate at a fairly constant rate, governed by the thermochemical properties of the mixture. The stoichiometric spark ignited flame is very similar to the laser-ignited flame up to about 0.5 ms, while the lean spark-ignited flame diverges almost immediately. However, both spark ignited flames feature an induction period during which the flame size stays fairly constant over a given time, before starting to grow again. This quasi-induction period is much pronounced for the lean mixture and occurs when the kernel is about half the size of the kernel for the stoichiometric mixture. For the lean mixture, the quasi-induction time extends up to 2 ms, during which heat loss might be severe enough to cause extinction.

As shown throughout this work, the addition of CO_2 in fuels can have a large impact on ignition behavior. Here laser and spark ignition of stoichiometric and lean ($\phi = 0.8$) mixtures of 100% CH_4 , 75% $\text{CH}_4/25\%$ CO_2 , and 50% $\text{CH}_4/50\%$ CO_2 are compared to determine the

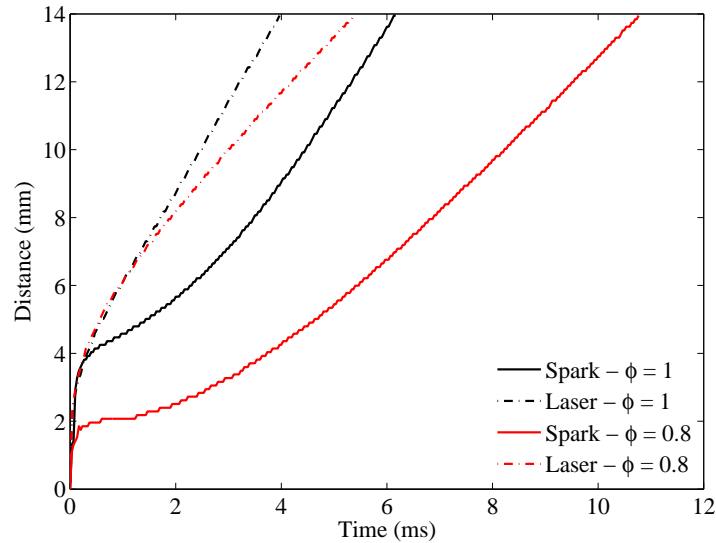


Figure 5.8: Quantitative differences in the evolution of the laser-induced and spark-ignited methane flame kernels. Differences are more pronounced for the lean mixtures.

effect CO₂ inclusion has on their relative ignition capabilities.

Schlieren images of the ignition events of lean methane and 50% CH₄/50% CO₂ mixtures are shown in Figure 5.9. Again, at 0.1 ms the flame kernels for all cases are similar. By 2.5 ms, vast differences can be observed in all four cases. For laser ignition, the 50% CH₄/50% CO₂ mixture shows a quenched front lobe and much smaller volume than the methane mixture. However, the flame in the toroidal section is strong enough to survive and by 7.5 ms both events have successfully transitioned to a self-sustained flame. The quenched front lobe of the laser-ignited flame is the same behavior observed in the previous chapter, characteristic of fuels/air mixtures with high amounts of CO₂ inclusion. The spark ignited flames are similar in volume at 2.5 ms. The methane flame continues to grow while propagation of the flame in the 50% CH₄/50% CO₂ mixture is suspended. Additionally, the contrast at the flame front also starts to fade, indicating a weakening of the flame. Although this particular case eventually leads to successful ignition, it is at this point where spark-ignited flame kernels for both the stoichiometric and lean 50% CH₄/50% CO₂ mixtures typically quench.

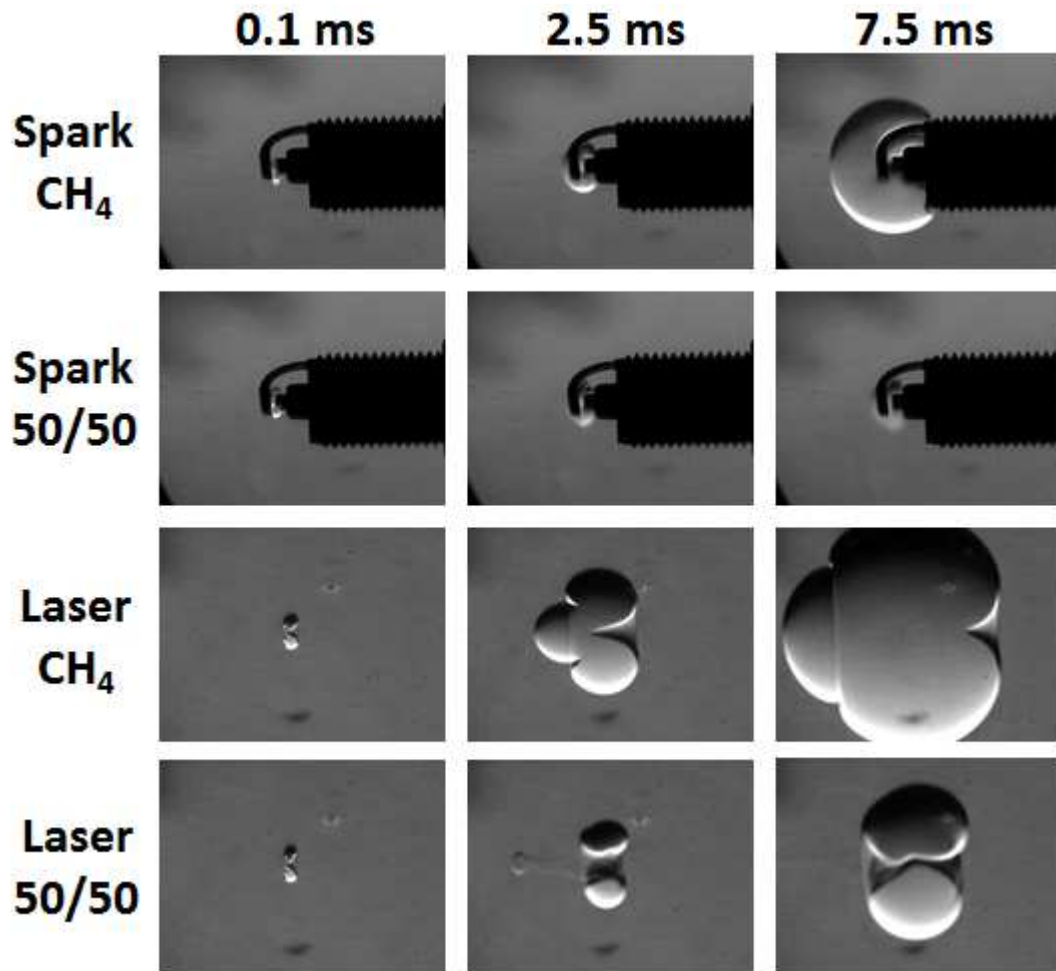


Figure 5.9: Evolution of laser- and spark-ignited flames of 100% CH_4 and 50% CH_4 /50% CO_2 , both at $\phi = 0.8$.

The above results focus on events in the early phase of flame propagation. Figure 5.10 shows the chamber pressure rise histories for lean mixtures of methane and biogas with various amounts of CO_2 . As before, observable pressure rise above the initial chamber pressure occurs at increasingly later times since the strength of the flame is weakened by the addition of CO_2 . Peak pressures of the laser- and spark ignited flames for all conditions are within 3%. The pressure trace for the methane ignition cases are very similar, as previously noted. With higher CO_2 content in the fuel, an increasing lag in the spark ignition pressure traces is observed, compared to the laser ignited flames.

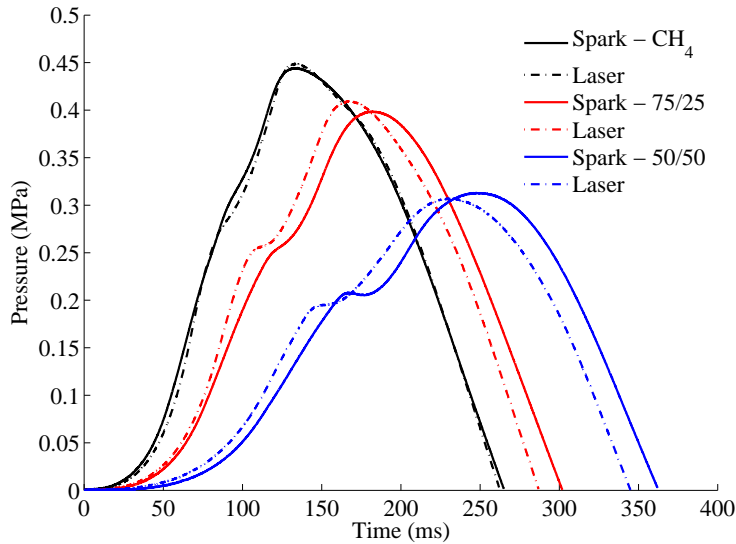


Figure 5.10: Pressure profiles for ignition of 100% CH_4 , 75% $\text{CH}_4/25\% \text{CO}_2$, and 50% $\text{CH}_4/50\% \text{CO}_2$ by laser and spark-discharge at $\phi = 0.8$. Spark ignition shows a small lag in pressure rise as more CO_2 is added to the fuel.

Although the pressure histories enable comparison of ignition events at times beyond 50 ms, they do not resolve differences in the transition from a flame kernel to self-sustained flame. Again, flame radius as determined by schlieren imaging is used to facilitate comparison between the ignition events at times up to 20 ms, as shown in Figure 5.11. The ignition events in this figure are the same events for which the pressure histories are displayed in Figure 5.10. The laser ignited flames all display similar growth until reaching a constant propagation speed. The spark ignited flames all display very different behavior. One consistent

trend among the spark ignited flames is that they all experience a near constant flame size over a considerable amount of time once the initial flame kernel is established. This effect becomes more pronounced with higher CO_2 content. Variations in the flame position for the spark ignited cases are due to uncertainty in the location of the flame front as determined by the Matlab code. The spark-ignited 50% CH_4 /50% CO_2 flame has a 10+ ms delay before a self-sustained flame is established. With this type of behavior, a flame might easily quench during this time in a turbulent environment as opposed to the quiescent condition studied here. With the addition of CO_2 in the fuel, the increased delay in the transition from a flame kernel to a propagating flame front was long enough to be reflected in the delayed overall pressure rise recorded in the combustion chamber for spark ignition.

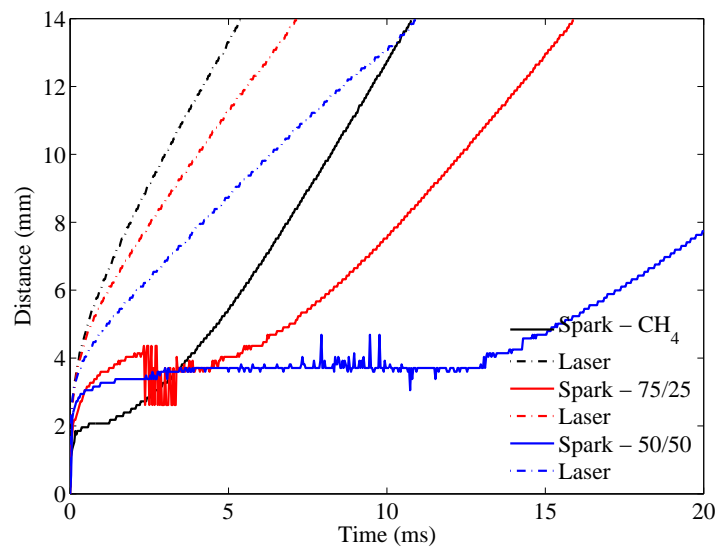


Figure 5.11: Quantitative differences in the evolution of the laser-induced and spark-ignited flame kernels for mixtures of 100% CH_4 , 75% CH_4 /25% CO_2 , and 50% CH_4 /50% CO_2 at $\phi = 0.8$. Long induction period is observed for spark ignited biogas mixtures.

The relative behavior of laser and spark ignited flames in the very early phase (up to 0.1 ms) point to some similarity in the energy transfer and plasma generation in the two methods. Subsequent evolution of the flame kernels show that the confinement imposed by the spark electrodes become a heat sink and also alter the flame kernel development. In weaker mixtures as found in lean fuel-air mixtures, this heat loss and the lower maximum flame temperatures

characteristic of such flames may lead to quenching of otherwise successfully initiated flame kernels. The stationary phase in the flame kernel evolution of the lean spark ignited flame, may attest to the loss of heat and therefore limited gas expansion which could favor the development of a strong flame kernel.

Regarding the impact of CO_2 in biogas ignition, the results of this work clearly show that ignition is affected by the level of CO_2 in the fuel mixture. The degree to which these processes are affected appears to depend on the ignition method, with the result that more misfires in the combustion of low calorific biogas might be observed in a spark ignited engine than in an engine equipped with laser ignition. The reason for this is to be found in the thermochemical properties of the fuels. Higher CO_2 inclusion is accompanied by a higher heat capacity in the fuel and lower cumulative heat release. The inclusion of carbon dioxide in a fuel therefore results in reduced flame temperatures. This in turn leads to slower flame propagation. With the spark plug, this is enough to stall the flame and lead to quenching when CO_2 inclusion is increased. These effects translate to a larger minimum flame kernel size required to guarantee the emergence of a self-sustained flame [130]. The results of this study show the flame kernel stalls when its size is the same order of magnitude as the surrounding electrodes. This induction period is likely to occur for all spark plugs, the degree to which would be dependent on the electrode geometry.

On the other hand, the very short, nanosecond-scale energy deposition of laser ignition, together with the absence of heat sinks such as electrodes, result in a larger high-temperature region immediately after the spark as was shown in Fig. 5.1. In reactive mixtures, this results in high initial flame kernel propagation speeds. This allows the flame to quickly develop to a sufficient size to allow for a smooth transition to a self-sustained flame.

Under engine-relevant conditions, a few differences from the results of this study are likely to be observed. For higher temperatures, both laser and spark ignition would see an extension of their respective lean flammability limits and lower equivalence ratios could be reached.

However, the differences in ignition performance identified in this study would likely remain the same. At higher pressures, a large difference in the ignition performance between the two technologies would be observed. High pressures hinder conventional spark generation while laser spark generation becomes easier, as shown in the results from Chapter 3. For the same energy level, the laser spark would become more robust while the conventional spark would weaken, leading to a greater probability of unsuccessful ignition. For this reason, laser ignition is an attractive option for high-pressure combustion systems. It should be noted that in such systems, combustion takes place in a turbulent flow field. This turbulence might affect the quantitative results obtained here in non-flow conditions. It has been observed by others [131] that turbulence increases minimum ignition energies and also increases the flame speed. This may have an effect on flame quenching. However, the trends observed here and the differences identified between laser and spark ignition are not expected to differ.

Chapter summary

To summarize, this chapter has investigated laser and spark ignition, aimed at gaining a fundamental understanding of the mechanisms contributing to the differences in combustion behavior observed in the literature through engine testing. Interferometry was utilized to compare spark geometry and the time scale of energy deposition. Schlieren imaging was then used to compare ignition dynamics associated with the two ignition technologies.

For iso-octane and E85 mixtures, development of the laser and spark ignited flames were found to be the same under stoichiometric conditions. Under lean conditions, where unsuccessful ignition using the spark plug was more likely, large differences between the development of the laser and spark ignited flames were observed. For laser ignition, a quick transition from flame kernel to self-sustained flame was observed. With spark ignition, after the flame kernel was established, a long induction period was observed as the surrounding electrodes slowed the transition to a self-sustained flame.

The impact of CO₂ inclusion in biogas was also examined using schlieren imaging and chamber pressure rise histories. Similar behavior to the previous fuels was observed with methane and biogas, including the presence of an induction period for the spark ignited flames. Heat loss effects in spark ignited flames showed a more pronounced effect in the change of propagation speed between stoichiometric and lean flames. The difficulty in propagation of spark ignited flames was amplified for biogas mixtures with high CO₂ content, increasing the probability of quenching. Once successfully propagating flames were realized, the resulting combustion chamber pressure rise histories showed little difference between laser-induced and spark ignited flames for methane mixtures. The lower burning rate of lean mixtures as well as mixtures with higher CO₂ inclusion was manifested in the pressure time histories by much longer delay times before observable pressure rise. It was under these conditions that differences in the pressure histories between laser and spark ignition became more pronounced.

Chapter 6

Conclusion and outlook

This thesis explores a number of phases of the laser ignition process, as well as experimental conditions that have not previously been investigated in detail, in order to further our understanding of the complex multi-physics of laser ignition. A constant volume combustion chamber has been used for laser and spark ignition experiments, investigating the combustion of methane, biogas, iso-octane, and E85. Observation of the ignition process was by means of schlieren imaging and interferometry.

Laser-induced breakdown was studied for a range of initial conditions and gas types. Following breakdown, the flow field dynamics and thermodynamic conditions were elucidated by means of two-color interferometry coupled with CFD simulations. The early phase of the flame kernel was then studied to highlight the effect fuel composition has on the ignition process and flame quenching. Investigation of the flame propagation for successful combustion events revealed how thermochemical properties of the fuel affect combustion behavior. Finally, the advantages of laser ignition were highlighted through a comparison of the similarities and differences with spark ignited flames.

Laser-induced breakdown

With respect to laser-induced breakdown, the effects of focusing optics, pressure, and fuel type have been established.

- The effect of focusing optics is such that the minimum energy required for optical breakdown increases with focal length due to the larger focal volume. In terms of the breakdown power density threshold for a given gas and initial condition, the power density is approximately constant except at very low focal lengths where plasma diffusion effects arise and lead to higher power density requirements.
- The minimum energy required for breakdown is such that it decreases with increasing pressure, making laser ignition attractive for high-pressure combustion.
- A generalized representation of focal length and pressure effects has been constructed. This is the first of such representations for optical breakdown at 532 nm. It highlights collisional cascade as the controlling mechanism for breakdown at this wavelength.
- Fuel effects on breakdown have been explored using methane and biogas. This is the first demonstration of breakdown in light combustible fuel/air mixtures. Minimal effects on the breakdown threshold are observed.

Early phase of flame

The early phase of the laser ignition process has been examined focusing on the dynamics of the laser-induced shock wave and the thermodynamic conditions of the resulting plasma kernel.

- The laser-induced shock wave propagation can be properly captured using Jones blast wave theory, from which the energy used to generate the shock wave can be deduced. This also enables complementary CFD simulations of the process.
- It is shown for the first time that the laser-induced shock wave in a combustible mixture is characterized by additional energy release from chemical reactions.
- By means of two-color interferometry, electron and gas density were measured. The structure and thermodynamic conditions of the early plasma kernel have been determined

giving further insight into the laser-induced flow fields.

- Comparing the early phase of laser ignition with that of spark ignition, it is found that the early plasma kernel of laser ignition is larger than that of spark ignition. This is specific to the focal length and spark type used. The longer energy transfer time for the spark plug has also been observed.

Flame dynamics

Propagation speeds and quenching behavior of both laser and spark ignited flames have been characterized.

- With respect to fuel effects, biogas flames propagate slower than methane, making biogas more susceptible to quenching under lean conditions. The same is true for iso-octane which was found to be more susceptible to quenching than E85. The reasons for these behaviors are traceable to thermochemical differences.
- Leaner mixtures require higher MIE and MPE; the higher pulse energy is different for different fuels.
- Contrasting the dynamics of laser ignited flames with spark ignited flames, it is observed that heat transfer to the electrode and the early kernel properties adversely affect spark ignited flames, resulting in longer induction and greater risk of quenching.

By examining these different physical aspects of laser ignition, this thesis advances understanding of forced ignition, consolidating this by contrasting with spark ignition behavior. The conclusions are useful for the design of fuel-flexible and lean combustion technologies. The data set is also useful for CFD simulations and simplified modeling of the ignition process.

Outlook

A few directions for the future of this work are possible:

- In this work, differences in the ignition behavior of methane and iso-octane have been highlighted. Carbon size in fuels may have an effect on the forced ignition behavior, making it of interest to expand this work to explore laser ignition of other larger fuel molecules. Additionally, it would be useful to expand the range of conditions to higher initial pressures. Due to the vapor pressure of heavy liquid fuels, expanding the range of conditions and fuels studied requires implementation of a heating element to increase the initial temperature of the chamber. This contribution would help develop a more general picture of laser ignition behavior and move the work toward more engine-relevant conditions.
- Differences in the ignition behavior between spark and laser ignition were observed in this work. Characterizing the spark plug energy would allow for better comparisons of the ignition energy for the two technologies and provide further insight into the mechanisms controlling spark ignition. Quantification of the spark plug energy requires further instrumentation to be implemented into the spark ignition circuit.
- With quantified energies and focal geometries, the data set provided here and future work can be used toward developing reactive CFD simulations. It has been shown through experiments in this work that the flow dynamics and thermodynamic conditions following breakdown differ between air and combustible fuel/air mixtures. It would therefore be useful to use CFD simulations to provide further insight into the flow field in combustible mixtures following laser-induced breakdown. This information could be used toward developing reduced-order laser ignition models which capture the general ignition behavior without resolving the detailed physics of the problem.

Bibliography

- [1] B. Lewis and G. von Elbe, *Combustion, flames and explosions of gases*. Academic Press, 1961.
- [2] T. Phuoc, “Laser spark ignition: experimental determination of laser-induced breakdown thresholds of combustion gases,” *Optics Communications*, vol. 175, no. 15, pp. 419–423, 2000.
- [3] M. Tsunekane and T. Taira, “High peak power, passively q-switched yb:yag/cr:yag micro-lasers,” *IEEE Journal of Quantum Electronics*, vol. 49, no. 5, pp. 454–461, 2013.
- [4] H. Kofler, E. Schwarz, and E. Wintner, “Experimental development of a monolithic passively q-switched diode-pumped nd:yag laser,” *The European Physical Journal D*, vol. 58, no. 2, pp. 209–218, 2010.
- [5] T. Patterson, “Laser-armed fighter jets by 2020, u.s. air force says,” December 2015. [CNN Online; posted 17-December-2015].
- [6] M. Lim, R. Anderson, and V. Arpaci, “Prediction of spark kernel development in constant volume combustion,” *Combustion and Flame*, vol. 69, pp. 303–316, 1987.
- [7] V. Arpacia, Y. Ko, M. Lim, and H. Lee, “Spark kernel development in constant volume combustion,” *Combustion and Flame*, vol. 135, pp. 315–322, 2003.
- [8] A. Kelley, G. Jomaas, and C. Law, “Critical radius for sustained propagation of

- spark-ignited spherical flames,” *Combustion and Flame*, vol. 156, pp. 1006–1013, 2009.
- [9] Z.Chen, M. Burke, and Y. Ju, “On the critical flame radius and minimum ignition energy for spherical flame initiation,” *Proceedings of the Combustion Institute*, vol. 33, pp. 1219–1226, 2011.
- [10] B. Sforzo, A. Lambert, J. Kim, J. Jagoda, S. Menon, and J. Seitzman, “Post discharge evolution of a spark igniter kernel,” *Combustion and Flame*, vol. 162, pp. 181–190, 2015.
- [11] D. Assanis, S. Wagnon, and M. Wooldridge, “An experimental study of flame and autoignition interactions of iso-octane and air mixtures,” *Combustion and Flame*, vol. 162, pp. 1214–1224, 2015.
- [12] B. Peterson, E. Baum, B. Bohm, and A. Dreizler, “Early flame propagation in a spark-ignition engine measured with quasi 4d-diagnostics,” *Proceedings of the Combustion Institute*, vol. 35, pp. 3829–3837, 2015.
- [13] R. Maly and M. Vogel, “Initiation and propagation of flame fronts in lean ch4-air mixtures by the three modes of the ignition spark,” *Symposium (International) on Combustion*, vol. 17, no. 1, pp. 821–831, 1979.
- [14] T. X. Phuoc, “Laser-induced spark ignition fundamental and applications,” *Optics and Lasers in Engineering*, vol. 44, pp. 351–397, 2006.
- [15] P. Ronney, “Laser versus conventional ignition of flames,” *Optical Engineering*, vol. 33, no. 2, pp. 510–521, 1994.
- [16] L. Radziemski and D. Cremers, eds., *Laser-Induced Plasmas and Applications*. Marcel Dekker Inc., 1989.
- [17] V. E. Mitsuk, V. I. Savoskin, and V. A. Chernikov, “Breakdown at optical frequencies

- in the presence of diffusion losses,” *JETP Letters*, vol. 4, pp. 88–90, 1966.
- [18] C. H. Chan, C. D. Moody, and W. B. McKnight, “Significant loss mechanisms in gas breakdown at $10.6\ \mu$,” *Journal of Applied Physics*, vol. 44, pp. 1179–1188, 1973.
- [19] J. Stricker and J. G. Parker, “Experimental investigation of electrical breakdown in nitrogen and oxygen induced by focused laser radiation at $1.064\ \mu$,” *Journal of Applied Physics*, vol. 53, pp. 851–855, 1982.
- [20] M. Foster, “Microwave breakdown calculations that include the effects of preionization in neon and neon-argon mixtures,” *National Technical Information Service*, vol. AFCRL-TR-73-0562, 1973.
- [21] R. Tambay and R. K. Thareja, “Laser-induced breakdown studies of laboratory air at 0.266 , 0.355 , 0.532 , and $1.06\ \mu\text{m}$,” *Journal of Applied Physics*, vol. 70, pp. 2890–2892, 1991.
- [22] M. Thiyagarajan and J. E. Scharer, “Experimental investigation of 193-nm laser breakdown in air,” *IEEE Transactions on Plasma Science*, vol. 36, pp. 2512–2521, 2008.
- [23] R. Hickling and W. Smith, “Combustion bomb tests of laser ignition,” in *SAE Technical Paper*, SAE International, 1974.
- [24] A. Alcock, K. Kato, and M. Richardson, “New features of laser-induced gas breakdown in the ultraviolet,” *Optics Communications*, vol. 6, no. 4, pp. 342–344, 1972.
- [25] M. Gower, “Krf laser-induced breakdown of gases,” *Optics Communications*, vol. 36, no. 1, pp. 43–45, 1981.
- [26] A. Alcock and S. Ramsden, “Two wavelength interferometry of a laser-induced spark in air,” *Applied Physics Letters*, vol. 8, no. 8, pp. 187–188, 1966.
- [27] W. Kimura, M. Kushner, E. Crawford, and S. Byron, “Laser interferometric measure-

- ments of a laser-preionization-triggered spark column,” *IEEE Transactions on Plasma Science*, no. 3, pp. 246–255, 1986.
- [28] M. Villagran-Muniz, H. Sobral, and E. Camps, “Shadowgraphy and interferometry using a cw laser and a ccd of a laser-induced plasma in atmospheric air,” *IEEE Transactions on Plasma Science*, vol. 29, no. 4, pp. 613–616, 2001.
- [29] S. Garnov, V. Konov, A. Malyutin, O. Tsarkova, I. Yatskovsky, and F. Dausinger, “High resolution interferometric diagnostics of plasmas produced by ultrashort laser pulses,” *Laser Physics*, vol. 13, no. 3, pp. 386–396, 2003.
- [30] A. Sagisaka, H. Daido, K. Ogura, S. Orimo, Y. Hayashi, M. Nishiuchi, M. Mori, K. Matsukado, A. Fukumi, Z. Li, S. Nakamura, K. Takagaki, H. Hazama, M. Suzuki, T. Utsumi, S. Bulanov, and T. Esirkepov, “Characterization of preformed plasmas with an interferometer for ultra-short high-intensity laser-plasma interactions,” *Appl. Phys. B*, vol. 78, pp. 919–922, 2004.
- [31] S. Soubacq, P. Pignolet, E. Schall, and J. Batina, “Investigation of a gas breakdown process in a laser-plasma experiment,” *J. Phys. D: Appl. Phys.*, vol. 37, pp. 2686–2702, 2004.
- [32] E. Amer, P. Gren, and M. Sjudahl, “Laser-ablation-induced refractive index fields studied using pulsed digital holographic interferometry,” *Optics and Lasers in Engineering*, vol. 47, pp. 793–799, 2009.
- [33] H. Zhang, J. Lu, Z. Shen, and X. Ni, “Investigation of 1.06 μm laser induced plasma in air using optical interferometry,” *Optics Communications*, vol. 282, pp. 1720–1723, 2009.
- [34] Y. Chen, J. Lewis, and C. Parigger, “Spatial and temporal profiles of pulsed laser-induced air plasma emissions,” *Journal of Quantitative Spectroscopy & Radiative*

- Transfer*, vol. 67, pp. 91–103, 2000.
- [35] N. Kawahara, J. Beduneau, T. Nakayama, E. Tomita, and Y. Ikeda, “Spatially, temporally, and spectrally resolved measurement of laser-induced plasma in air,” *Appl. Phys. B*, vol. 86, pp. 605–614, 2007.
- [36] S. Yalcin, D. Crosley, G. Smith, and G. Faris, “Influence of ambient conditions on the laser air spark,” *Appl. Phys. B*, vol. 68, pp. 121–130, 1999.
- [37] H. El-Rabii, S. Victorov, and A. Yalin, “Properties of an air plasma generated by ultraviolet nanosecond laser pulses,” *J. Phys. D: Appl. Phys.*, vol. 42, 2009.
- [38] R. Navarro-Gonzalez and M. Villagran-Muniz, “Effect of beam waist on shock properties of laser-induced plasmas in air by the photoacoustic probe beam deflection method,” *Analytical Sciences*, vol. 17, pp. 118–121, 2001.
- [39] M. Villagran-Muniz, H. Sobral, and R. Navarro-Gonzalez, “Shock and thermal wave study of laser-induced plasmas in air by the probe beam deflection technique,” *Measurement Science and Technology*, vol. 14, pp. 614–618, 2003.
- [40] M. Lackner, S. Charareh, F. Winter, K. F. Iskra, D. Rdisser, T. Neger, H. Kopecek, and E. Wintner, “Investigation of the early stages in laser-induced ignition by schlieren photography and laser-induced fluorescence spectroscopy,” *Optics Express*, vol. 12, pp. 4546–4557, 2004.
- [41] G. C. Gebel, T. Mosbach, W. Meier, and M. Aigner, “Laser-induced blast waves in air and their effect on monodisperse droplet chains of ethanol and kerosene,” *Shock Waves*, vol. 25, pp. 415–429, 2015.
- [42] G. Taylor, “The formation of a blast wave by a very intense explosion,” *I. Theoretical discussion. Proc. R. Soc. Lond. A*, vol. 201, pp. 159–174, 1950.

- [43] J. Lee and R. Knystautas, "Laser spark ignition of chemically reactive gases," *AIAA 6th Aerospace Sciences Meeting*, 1968.
- [44] T. Spiglanin, A. McIlroy, E. Fournier, R. Cohen, and J. Syage, "Time-resolved imaging of flame kernels: Laser spark ignition of $\text{H}_2/\text{O}_2/\text{Ar}$ mixtures," *Combustion and Flame*, vol. 102, no. 3, pp. 310–328, 1995.
- [45] T. Phuoc and F. White, "An optical and spectroscopic study of laser-induced sparks to determine available ignition energy," *Proceedings of the Combustion Institute*, vol. 29, pp. 1621–1628, 2002.
- [46] J. Beduneau, B. Kimb, L. Zimmerer, and Y. Ikeda, "Measurements of minimum ignition energy in premixed laminar methane/air flow by using laser induced spark," *Combustion and Flame*, vol. 132, pp. 653–665, 2003.
- [47] A. Starikovskiy and N. Aleksandrov, "Plasma-assisted ignition and combustion," *Progress in Energy and Combustion Science*, vol. 39, pp. 61–110, 2013.
- [48] M. Cordier, A. Vandell, G. Cabot, B. Renou, and A. Boukhalfa, "Laser-induced spark ignition of premixed confined swirled flames," *Combustion Science and Technology*, vol. 185, pp. 379 – 407, 2013.
- [49] E. Lim, A. McIlroy, P. Ronney, and J. Syage, "Detailed characterization of minimum ignition energies of combustible gases using laser ignition sources," *Transport phenomena in combustion*, vol. 1, pp. 176–184, 1996.
- [50] D. Bradley, C. Sheppard, I. Suardjaja, and R. Woolley, "Fundamentals of high-energy spark ignition with lasers," *Combustion and Flame*, vol. 138, no. 1-2, pp. 55 – 77, 2004.
- [51] M. Weinrotter, D. Srivastava, K. Iskra, J. Graf, H. Kopecek, J. Klausner, G. Herdin, and E. Wintner, eds., *Laser ignition of engines - a realistic option!*, vol. 6053 of *Proc. of SPIE*, Intl. Conf. on Lasers, Applications, and Technologies 2005: High-Power Lasers

- and Applications, 2005.
- [52] M. Tsunekane, T. Inohara, K. Kanehara, and T. Taira, "Micro-solid-state laser for ignition of automobile engines," *Advances in Solid-State Lasers: Development and Applications*, pp. 195–212, 2010.
- [53] N. Pavel, M. Tsunekane, and T. Taira, "Composite, all-ceramics, high-peak power Nd:YAG/Cr₄₊:YAG monolithic micro-laser with multiple-beam output for engine ignition," *Optics express*, vol. 19, no. 10, pp. 9378–9384, 2011.
- [54] J. Tauer, H. Kofler, and E. Wintner, "Laser-initiated ignition," *Laser & Photonics Reviews*, vol. 4, no. 1, pp. 99–122, 2010.
- [55] M. H. Morsy, "Review and recent developments of laser ignition for internal combustion engines applications," *Renewable and Sustainable Energy Reviews*, vol. 16, pp. 4849–4875, 2012.
- [56] J. Ma, D. Alexander, and D. Poulain, "Laser spark ignition and combustion characteristics of methane-air mixtures," *Combustion and Flame*, vol. 112, no. 4, pp. 492–506, 1998.
- [57] T. X. Phuoc and F. P. White, "Laser-induced spark ignition of ch₄/air mixtures," *Combustion and Flame*, vol. 119, pp. 203–216, 1999.
- [58] H. Kopecek, H. Maier, G. Reider, F. Winter, and E. Wintner, "Laser ignition of methane-air mixtures at high pressures," *Experimental Thermal and Fluid Science*, vol. 27, pp. 499–503, 2003.
- [59] D. Srivastava, K. Dharamshi, and A. Agarwal, "Flame kernel characterization of laser ignition of natural gas-air mixture in a constant volume combustion chamber," *Optics and Lasers in Engineering*, vol. 49, pp. 1201–1209, 2011.

- [60] D. Srivastava and A. Agarwal, "Laser ignition of single cylinder engine and effects of ignition location," *SAE Technical Papers*, 2013.
- [61] D. Srivastava, E. Wintner, and A. Agarwal, "Effect of focal size on the laser ignition of compressed natural gas-air mixture," *Optics and Lasers in Engineering*, vol. 58, pp. 67–79, 2014.
- [62] D. Srivastava, E. Wintner, and A. Agarwal, "Effect of laser pulse energy on the laser ignition of compressed natural gas fueled engine," *Optical Engineering*, vol. 53, no. 5, 2014.
- [63] J. Mullett, R. Dodd, C. Williams, G. Triantos, G. Dearden, A. Shenton, K. Watkins, S. Carroll, A. Scarisbrick, and S. Keen, "The influence of beam energy, mode and focal length on the control of laser ignition in an internal combustion engine," *J. Phys. D: Appl. Phys.*, vol. 40, pp. 4730–4739, 2007.
- [64] R. Dodd, J. Mullett, S. Carroll, G. Dearden, A. Shenton, K. G. Watkins, G. Triantos, and S. Keen, "Laser ignition of an ic test engine using an nd: Yag laser and the effect of key laser parameters on engine combustion performance," *Lasers in Eng.*, vol. 10, pp. 1–19, 2007.
- [65] G. Dearden and T. Shenton, "Laser ignited engines: progress, challenges and prospects," *Optics Express*, vol. 21, pp. A1113–A1125, 2013.
- [66] C. Ternel, B. Lecordier, M. Trinit, and A. Cessou, eds., *Laser-induced spark ignition of propane-air and isooctane-air*, Proc. of the European Combustion Meeting 2005, 2005.
- [67] T. Lieuwen, V. McDonnell, E. Petersen, and D. Santavicca, "Fuel flexibility influences on premixed combustor blowout, flashback, autoignition, and stability," *ASME Journal of Engineering for Gas Turbines and Power*, vol. 130, no. 1, 2008.
- [68] A. Bruijstens, W. Beuman, M. Molen, J. Rijke, R. Cloudt, G. Kadijk, O. Camp, and

- S. Bleuanus, "Biogas composition and engine performance, including database and biogas property model," *European Commission Report: Biogasmax*, 2008.
- [69] Q. Zhang, D. Noble, and T. Lieuwen, "Characterization of fuel composition effects in $\text{H}_2/\text{CO}/\text{CH}_4$ mixtures upon lean blowout," *ASME Journal of Engineering for Gas Turbines and Power*, vol. 129, no. 3, pp. 688–694, 2007.
- [70] D. Kang, T. Kim, K. Hur, and J. Park, "The effect of firing biogas on the performance and operating characteristics of simple and recuperative cycle gas turbine combined heat and power systems," *Applied Energy*, vol. 93, pp. 215–228, 2012.
- [71] C. Mordaunt and W. Pierce, "Design and preliminary results of an atmospheric-pressure model gas turbine combustor utilizing varying CO_2 doping concentration in CH_4 to emulate biogas combustion," *Fuel*, vol. 124, 2014.
- [72] C. Forsich, M. Lackner, F. Winter, H. Kopecek, and E. Wintner, "Characterization of laser-induced ignition of biogas-air mixtures," *Biomass and Bioenergy*, vol. 27, no. 3, pp. 299 – 312, 2004.
- [73] J. Biet, M. Ndem, M. Idir, and N. Chaumeix, "Ignition by electric spark and by laser-induced spark of ultra-lean CH_4/air and $\text{CH}_4/\text{CO}_2/\text{air}$ mixtures at high pressure," *Combust. Sci. Technol.*, vol. 186, pp. 1–23, 2014.
- [74] P. Dagaut and C. Togb, "Oxidation kinetics of mixtures of iso-octane with ethanol or butanol in a jet-stirred reactor: experimental and modeling study," *J. of Comb. Sci. and Tech.*, vol. 184, no. 7-8, pp. 1025–1038, 2012.
- [75] G. Broustail, F. Halter, P. Seers, G. Morac, and C. Mounam-Rousselle, "Experimental determination of laminar burning velocity for butanol/iso-octane and ethanol/iso-octane blends for different initial pressures," *Fuel*, vol. 106, pp. 310–317, 2013.
- [76] G. B. Jr., J. Luecke, M. Ratcliff, E. Osecky, and B. Zigler, "Effects of iso-octane/ethanol

- blend ratios on the observance of negative temperature coefficient behavior within the ignition quality tester,” *Fuel*, vol. 186, pp. 82–90, 2016.
- [77] P. Aleiferis, J. Serras-Pereira, and D. Richardson, “Characterisation of flame development with ethanol, butanol, iso-octane, gasoline and methane in a direct-injection spark-ignition engine,” *Fuel*, vol. 109, pp. 256–278, 2013.
- [78] B. Moxey, A. Cairns, and H. Zhao, “A comparison of burning characteristics of iso-octane and ethanol fuels in an optical si engine,” *Journal of KONES Powertrain and Transport*, vol. 20, no. 2, pp. 299–305, 2016.
- [79] N. Kawahara, E. Tomita, and S. Nakamura, eds., *Laser-Induced Plasma Generation and Evolution in a Transient Spray*, 16th Int Symp on Applications of Laser Techniques to Fluid Mechanics, 2012.
- [80] K. Rahman, N. Kawahara, K. Tsuboi, and E. Tomita, eds., *Experimental Study on Combustion Characteristics of Wet Ethanol Ignited by Laser-Induced Breakdown*, 3rd Laser Ignition Conference, 2015.
- [81] T. Seo, Y. Ishimura, and M. Mikami, eds., *A Study on Ignition Characteristics of Rich-Premixed Ethanol Spray by Laser-Induced Plasma*, OSA, 3rd Laser Ignition Conf., 2015.
- [82] H. Adelman, “A time dependent theory of spark ignition,” *Eighteenth Symposium (International) on Combustion - The Combustion Institute*, pp. 1333–1342, 1981.
- [83] R. Maly, “Ignition model for spark discharges and the early phase of flame front growth,” *Eighteenth Symposium (International) on Combustion - The Combustion Institute*, pp. 1747–1754, 1981.
- [84] M. Kono, K. Niu, T. Tsukamoto, and Y. Ujiie, “Mechanism of flame kernel formation produced by short duration sparks,” *Twenty-Second Symposium (International) on*

- Combustion - The Combustion Institute*, pp. 1643–1649, 1988.
- [85] K. Ishii, T. Tsukamoto, Y. Ujiie, and M. Kono, “Analysis of ignition mechanism of combustible mixtures by composite sparks,” *Combustion and Flame*, vol. 91, pp. 153–164, 1992.
- [86] T. Kravchik and E. Sher, “Numerical modeling of spark ignition and flame initiation in a quiescent methane-air mixture,” *Combustion and Flame*, vol. 99, pp. 635–643, 1994.
- [87] C. Kaminski, J. Hult, M. Alde, S. Lindenmaier, A. Dreizler, U. Maas, and M. Baum, “Spark ignition of turbulent methane/air mixtures revealed by time-resolved planar laser-induced fluorescence and direct numerical simulations,” *Proceedings of the Combustion Institute*, vol. 28, pp. 399–405, 2000.
- [88] M. Thiele, S. Selle, U. Riedel, J. Warnatz, and U. Maas, “Numerical simulation of spark ignition including ionization,” *Proc. of Comb. Inst.*, vol. 28, pp. 1177–1185, 2000.
- [89] M. Thiele, J. Warnatz, A. Dreizler, S. Lindenmaier, R. Schießl, U. Maas, A. Grant, and P. Ewart, “Spark ignited hydrogen/air mixtures: Two dimensional detailed modeling and laser based diagnostics,” *Combustion and Flame*, vol. 128, pp. 74–87, 2002.
- [90] J. Han, H. Yamashita, and N. Hayashi, “Numerical study on the spark ignition characteristics of a methane-air mixture using detailed chemical kinetics effect of equivalence ratio, electrode gap distance, and electrode radius on mie, quenching distance, and ignition delay,” *Combustion and Flame*, vol. 157, pp. 1414–1421, 2010.
- [91] S. Bane, J. Ziegler, and J. Shepherd, “Investigation of the effect of electrode geometry on spark ignition,” *Combustion and Flame*, vol. 162, pp. 462–469, 2015.
- [92] H. Hedfi, A. Jbara, H. Jedli, K. Slimi, and A. Stoppato, “Performance enhancement of a spark ignition engine fed by different fuel types,” *Energy Conversion and Management*, vol. 112, pp. 166–175, 2016.

- [93] A. Wandel, "Influence of scalar dissipation on flame success in turbulent sprays with spark ignition," *Combustion and Flame*, vol. 161, pp. 2579–2600, 2014.
- [94] H. Yan, R. Adelgren, M. Boguszko, G. Elliott, and D. Knight, "Laser energy deposition in quiescent air," *AIAA Journal*, vol. 41, no. 10, 2003.
- [95] M. H. Morsy, Y. Ko, and S. H. Chung, "Laser-induced ignition using a conical cavity in ch4-air mixtures," *Combustion and Flame*, vol. 119, no. 4, pp. 473–482, 1999.
- [96] M. H. Morsy and S. H. Chung, "Numerical simulation of front lobe formation in laser-induced spark ignition of ch4/air mixtures," *Proc. of Comb. Inst.*, vol. 29, pp. 1613–1619, 2002.
- [97] S. Ghosh and K. Mahesh, "Numerical simulation of the fluid dynamic effects of laser energy deposition in air," *J. Fluid Mech.*, vol. 603, pp. 329–354, 2008.
- [98] J. Koga, K. Moribayashi, Y. Fukuda, S. Bulanov, A. Sagisaka, K. Ogura, H. Daido, M. Yamagiwa, T. Kimura, T. Fujikawa, M. Ebina, and K. Akihama, "Simulation and experiments of the laser induced breakdown of air for femtosecond to nanosecond order pulses," *J. Phys. D: Appl. Phys.*, vol. 43, 2010.
- [99] R. Joarder, G. C. Gebel, and T. Mosbach, "Two-dimensional numerical simulation of a decaying laser spark in air with radiation loss," *Int. J. Heat and Mass Transfer*, vol. 63, pp. 284–300, 2013.
- [100] G. Tartar, H. Ranner, F. Winter, and E. Wintner, "Simulation of optical breakdown in nitrogen by focused short laser pulses of 1064 nm wavelength," *Laser and Particle Beams*, vol. 26, pp. 567–573, 2008.
- [101] D. Skoog, F. Holler, and S. Crouch, *Principles of Instrumental Analysis*. International student edition, Thomson Brooks/Cole, 2007.

- [102] T. Alger, B. Mangold, D. Mehta, and C. Roberts, eds., *The effect of sparkplug design on initial flame kernel development and sparkplug performance*, SAE 2006 World Congress & Exhibition, 2006.
- [103] B. Wolk, A. DeFilippo, J. Chen, R. Dibble, A. Nishiyama, and Y. Ikeda, “Enhancement of flame development by microwave-assisted spark ignition in constant volume combustion chamber,” *Combustion and Flame*, vol. 160, pp. 1225–1234, 2013.
- [104] G. S. Settles, *Schlieren and Shadowgraph Techniques: Visualizing Phenomena in Transparent Media*. Springer, 2001.
- [105] G. Toker, *Holographic Interferometry: A Mach-Zehnder Approach*. CRC Press, 2012.
- [106] J. Qi, C. Leung, W. Wong, and S. Probert, “Temperature-field measurements of a premixed butane/air circular impinging-flame using reference-beam interferometry,” *Applied Energy*, vol. 83, pp. 1307–1316, 2006.
- [107] D.-Y. Zhang and H.-C. Zhou, “Temperature measurement by holographic interferometry for non-premixed ethylene-air flame with a series of state relationships,” *Fuel*, vol. 86, pp. 1552–1559, 2007.
- [108] E. McLean and S. Ramsden, “Optical interferometric and spectroscopic measurements of electron density in a plasma,” vol. 140, no. 4, 1965.
- [109] B. Weber and S. Fulghum, “A high sensitivity two-color interferometer for pulsed power plasmas,” *Review of Scientific Instruments*, vol. 68, no. 2, pp. 1227–1232, 1997.
- [110] S. Fulghum, “Multi-beam laser interferometer for plasma density measurements in a plasma erosion opening switch (peos),” 1994.
- [111] R. Feynman, R. Leighton, and M. Sands, *The Feynman lectures on physics*. Addison-Wesley world student series, Addison-Wesley Pub. Co., 1963.

- [112] R. Huddlestone and S. Leonard, *Plasma Diagnostic Techniques*. Pure and Applied Physics, Academic Press, 1965.
- [113] M. Bak, S. Im, and M. Cappelli, “Successive laser-induced breakdowns in atmospheric pressure air and premixed ethane-air mixtures,” *Combustion and Flame*, vol. 161, pp. 1744–1751, 2014.
- [114] F. Jenkins and H. White, *Fundamentals of optics*. McGraw-Hill, 2nd ed., 1983.
- [115] F. Paschen, “Ueber die zum funkenubergang in luft, wasserstoff und kohlensaure bei verschiedenen drucken erforderliche potentialdifferenz (on the potential difference required for spark initiation in air, hydrogen, and carbon dioxide at different pressures),” *Annalen der Physik*, vol. 273, no. 5, pp. 69–75, 1889.
- [116] P. Chylek, M. Jarzembki, V. Srivastava, and R. Pinnick, “Pressure dependence of the laser-induced breakdown thresholds of gases and droplets,” *Applied Optics*, vol. 29, no. 15, pp. 2303–2306, 1990.
- [117] A. D. MacDonald, ed., *Microwave Breakdown in Gases*. Wiley, 1966.
- [118] D. Lencioni and L. Pettingill, “The dynamics of air breakdown initiated by a particle in a laser beam,” *J. Appl. Phys.*, vol. 48, no. 5, pp. 1848–1851, 1977.
- [119] J. V. Neumann, ed., *Theory of detonation waves*, Institute for Advanced Study Princeton NJ, 1942.
- [120] H. Brode, “Point source explosion in air,” 1956.
- [121] D. L. Jones, “Intermediate strength blast wave,” *Physics of Fluids*, vol. 11, 1968.
- [122] D. L. Jones, “The energy parameter b for strong blast waves,” *National Bureau of Standards Technical Note*, vol. 155, 1962.
- [123] A. Demirbas, *Biofuels: Securing the Planet’s Future Energy Needs*. Springer, 2009.

- [124] P. Aleiferis and M.K.Behringer, “Flame front analysis of ethanol, butanol, iso-octane and gasoline in a spark-ignition engine using laser tomography and integral length scale measurements,” *Combustion and Flame*, vol. 162, no. 12, pp. 1–20, 2015.
- [125] F. Incropera and D. DeWitt, *Fundamentals of Heat and Mass Transfer*. Wiley, 5th ed., 2007.
- [126] A. Mameri, F. Tabet, and A. Hadeif, “Numerical investigation of biogas diffusion flames characteristics under several operation conditions in counter-flow configuration with emphasis on thermal and chemical effects of CO_2 in the fuel mixture,” *Heat and Mass Transfer*, pp. 1–10, 2017.
- [127] L. Qiao, Y. Gan, T. Nishiie, W. Dahm, and E. Oran, “Extinction of premixed methane/air flames in microgravity by diluents: Effects of radiation and lewis number,” *Combustion and Flame*, vol. 157, no. 8, pp. 1446–1455, 2010.
- [128] B. Almansour, L. Thompson, J. Lopez, G. Barari, and S. Vasu, “Laser ignition and flame speed measurements in oxy-methane mixtures diluted with CO_2 ,” *Journal of Energy Resources Technology*, vol. 138, no. 3, p. 032201, 2016.
- [129] G. Stiesch, *Modeling Engine Spray and Combustion Processes*. Heat and Mass Transfer, Springer, 1 ed., 2003.
- [130] D. Ballal and A. Lefebvre, “Ignition and flame quenching in flowing gaseous mixtures,” *Proceedings of the Royal Society, London Series A*, vol. 357, no. 1689, pp. 163–181, 1977.
- [131] C. Cardin, B. Renou, G. Cabot, and A. Boukhalfa, “Experimental analysis of laser-induced spark ignition of lean turbulent premixed flames: New insight into ignition transition,” *Combustion and Flame*, vol. 160, pp. 1414–1427, 2013.

Vita

Author's Name: Nathan D. Peters
Place of Birth: Geneva, Illinois, USA
Date of Birth: June 1st, 1990

Degrees Awarded:

Master of Science, Syracuse University, 2013
Bachelor of Science, Iowa State University, 2012

Professional Experience:

Teaching and Research Assistant, Syracuse University Department of MAE, 2012-2017
Graduate Research Aide, Argonne National Laboratory, 2016
Research Assistant, Iowa State University, 2011